Into darkness: From high density quenching to near-infrared scintillators

Wolszczak, Weronika

DOI
10.4233/uuid:6d7dc81b-f374-4600-a902-58026bb19708

Publication date
2019

Document Version
Final published version

Citation (APA)
Wolszczak, W. (2019). *Into darkness: From high density quenching to near-infrared scintillators*. [Dissertation (TU Delft), Delft University of Technology]. https://doi.org/10.4233/uuid:6d7dc81b-f374-4600-a902-58026bb19708

INTO DARKNESS: FROM HIGH DENSITY QUENCHING TO NEAR-INFRARED SCINTILLATORS

INTO DARKNESS: FROM HIGH DENSITY QUENCHING TO NEAR-INFRARED SCINTILLATORS

Dissertation

for the purpose of obtaining the degree of doctor
at Delft University of Technology
by the authority of the Rector Magnificus, prof.dr.ir. T.H.J.J. van der Hagen,
chair of the Board for Doctorates
to be defended publicly on
Monday 9, September 2019 at 12:30 o'clock

by

Weronika Wiktoria WOLSZCZAK

Master of Science in Physics,
University of Warsaw, Poland,
born in Lipsko, Poland.

This dissertation has been approved by the promotor

promotor: prof. dr. P. Dorenbos

Composition of the doctoral committee:

Rector Magnificus,	chairperson
Prof. dr. P. Dorenbos	Delft University of Technology
Independent members:	
Prof. dr. L.D.A. Siebbeles,	Delft University of Technology
Dr. D.R. Schaart,	Delft University of Technology
Prof. dr. C. Ronda,	Zhejiang University, China/Philips, The Netherlands
Prof. dr. H. van der Graaf,	Delft University of Technology/Nikhef Amsterdam, The Netherlands
Dr. V.O. Ouspenski	Saint-Gobain Crystals/France
Prof. dr. K.W. Krämer	Bern University/Switzerland

The research leading to this thesis was supported by the Dutch Technology Foundation (STW), which is part of the Netherlands Organization for Scientific Research (NWO). This work was partly funded by Saint-Gobain Research, France.

The research described in this thesis was performed in the section Luminescence Materials, part of the Radiation Science & Technology department, faculty of Applied Sciences, Delft University of Technology.

Keywords: scintillator, α/β ratio, digital signal processing, pulse shape discrimination, alpha particles, non-radiative energy transfer, near-infrared scintillator

Printed by: GVO drukkers & vormgevers B.V.

Front & Back: The front picture by GloFX, 3624 North Monroe St. Tallahassee, FL USA 32303. Cover design: W. Wolszczak

ISBN 978-94-6332-533-2

An electronic version of this dissertation is available at
`http://repository.tudelft.nl/`.

To my mother

Nothing in life is to be feared, it is only to be understood. Now is the time to understand more, so that we may fear less.

Maria Skłodowska-Curie

CONTENTS

1

INTRODUCTION

Any knowledge that doesn't lead to new questions quickly dies out:
it fails to maintain the temperature required for sustaining life.

Wisława Szymborska

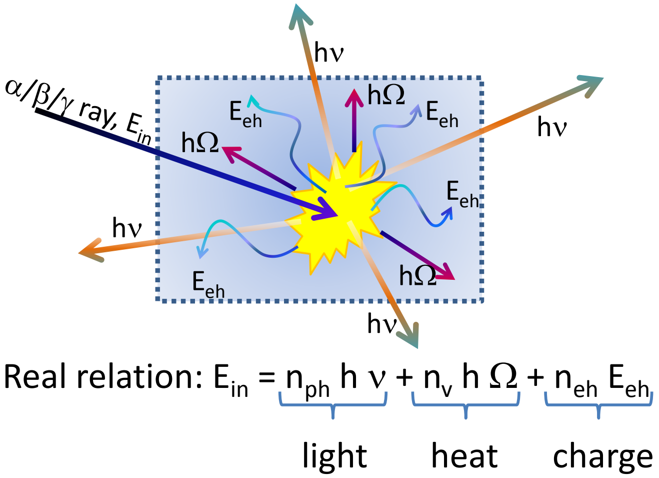

Figure 1.1: Different channels of ionizing radiation energy conversion in matter.

1.1. BIRDS EYE PERSPECTIVE ON RADIATION INTERACTION WITH MATTER

When a high energy particle stops in a material it looses its energy (transforms it) into other forms. When looking from a top-level perspective we can divide the final energy deposit into three categories:

1. photons (light, scintillation),
2. vibrations of a crystal lattice (phonons, heat),
3. and free electron-holes (free charge carriers).

Despite of simplicity of this classification, it helps to organize thinking about different modes of radiation detection and to see them as parts of a broader picture. Fig. 1.1 illustrates this with an equation, where initial energy E_{in} of a particle is transformed and branched between emission of: n_{ph} photons with average energy $h\nu$, n_{ν} phonons (lattice vibration modes) with average energy $h\Omega$, and n_{eh} free electron-hole pairs with average energy E_{eh}.

Each energy conversion channel was addressed and exploited in past research for the purpose of radiation detection, and it resulted in development of many types of detectors and techniques. Fig. 1.2 shows energy conversion channels and detectors which make use of them. Bolometers can be used for ionization radiation detection by measuring a material temperature increase with a temperature-dependent electrical resistance element. They found application in particle physics, particularly in Dark Matter and rare-decays search [1–5]. Scintillators make use of immediate light emission by the excited material, while Thermo-Luminescence (TL) dosimeters can store trapped-charges and release them latter upon thermal activation. High purity germanium (HPGe) and

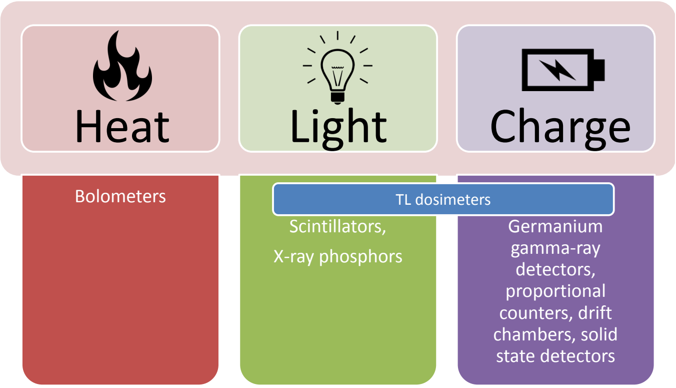

Figure 1.2: Different detector types exploit different energy loss channels.

other solid state detectors are designed to directly collect free charge carriers created by an ionizing particle.

Obviously, each of these detector types try to minimize branching energy to other channels for obtaining high efficiency. For HPGe detectors a long lifetime of free charges, high drift velocity, and low recombination rate are required to collect all charges at the electrodes, avoid trapping and energy loss as heat or light. The opposite requirements are posed on scintillation detectors: as fast as possible capture of ionized charges by a luminescence dopant facilitates rapid and efficient light emission. For TL dosimeters a presence of deep charge traps is essential for capturing free charge carriers and storing them without fading until a later thermo-stimulated optical readout.

1.2. SCINTILLATION

A scintillator (from Latin *scintilla*: a spark) is a material which can absorb ionizing radiation and downconvert its energy into a short pulse of light. The process is symbolically depicted in Fig. 1.3, where an incoming particle is absorbed by a material and leads to a pulse of n_{ph} photons. By measuring the number of emitted photons we can deduce the energy of the incoming high energy particle. This principle is the basis of nuclear spectroscopy, where a scintillator is coupled to a photodetector, and the amount of detected light is assumed to be proportional to the absorbed energy. This picture is obviously oversimplified, and reality is much more complex. If we will consider all processes shown in Fig. 1.1, the process of downconvertion is never 100% efficient. Moreover, the linear relation shown in Fig. 1.3 is also broken in all known scintillators.

Only energy emitted as light is useful for scintillation detection, while the other forms of energy are lost. Phonon and photon emission can be detected in scintillating bolometers [1], however it is not practical for most of spectroscopic applications. Free electrons and holes can be trapped by defects and impurities in the crystal, which eliminate them from instantaneous light emission and contribute to delayed light emission (afterglow). Measurements of bismuth germanate (BGO) with a scintillating bolometer enabled quantification of the branching ratios between these three channels. It was found

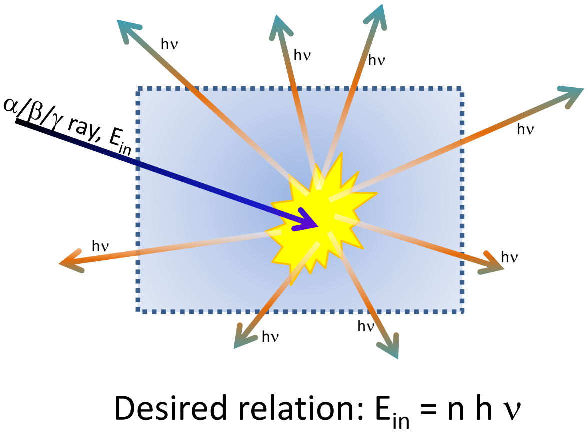

Figure 1.3: The main principle of spectroscopy with scintillators.

that at 6 K only 5.8% of the absorbed γ-photon energy is transformed into light, while the remaining part is converted into heat 46.4% and free charge carriers 47.8% [6]. Free charge carriers become eventually trapped at deep traps and do not participate in scintillation process. This makes BGO a rather inefficient scintillator.

1.3. RADIATION INTERACTION WITH MATTER

A gamma photon can interact with a scintillator by three basic interactions:

1. Compton scattering which is responsible for the Compton edge and Compton continuum;
2. the photoelectric effect which is responsible for the photo-peak;
3. pair production which only becomes important well above 1.022 MeV

Different interactions dominate depending on initial energy and materials properties. Compton scattering and the photoelectric effect are schematically depicted in Fig. 1.4. Compton scattering leads to a partial deposition of incident gamma photon energy in a scintillating crystal, as the scattered photon can escape the detector volume. The most important for γ-spectroscopy is the photoelectric effect which leads to a full absorption of the incident photon energy. In Fig. 1.4 the full absorption peak (also called "a photopeak") is located at 662 keV. However, the photopeak in small crystals can be accompanied by an X-ray escape peak. After absorption of a gamma photon by the photoelectric effect, a hole is left in an inner orbit of the excited atom. Next, the hole is filled up with an electron from a higher orbit what is accompanied with emission of characteristic X-rays. These X-ray photons can escape undetected from a small crystal and decrease the full absorption peak energy by the corresponding X-ray energy. Fig. 1.4 shows a lanthanum K_α X-ray escape peak in $LaBr_3$:Ce,Sr.

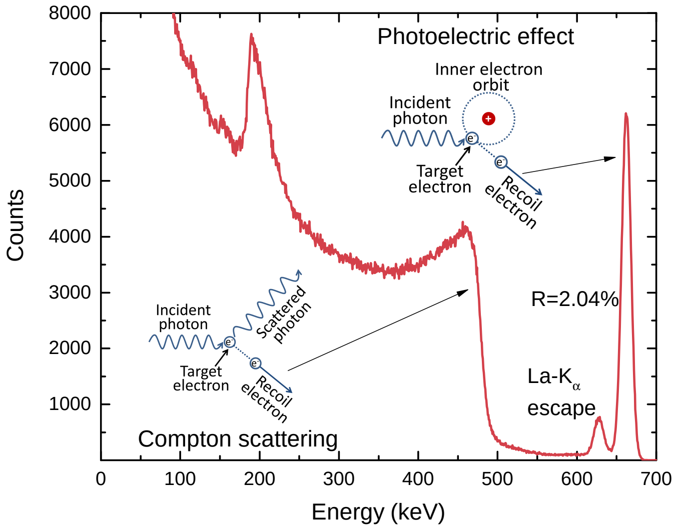

Figure 1.4: Pulse height spectrum of ^{137}Cs isotope measured with LaBr$_3$:Ce,Sr sample and an Avalanche Photodiode readout. Data reproduced from [7].

While high energy electron interaction with matter results in multiple scattering, alpha particles travel along almost straight paths. Fig. 1.5 shows simulated alpha particle paths in sodium iodide NaI using the SRIM particle track simulation package [8]. The density of excitation due to alpha particles can be much higher than with electrons. It is because of their higher mass and higher charge state. Employing α-particles gives an unique opportunity for studying scintillation properties at high ionization density.

1.4. SCINTILLATION MECHANISM

There is probably no single scintillation mechanism which applies equally to all known scintillators. Through the years of research many theoretical models have been proposed with increasing sophistication of the analyzed details. In this section I will limit myself to discussing only the most recent model proposed for CsI:Tl.

Fig. 1.6 shows the state of art understanding of the scintillation mechanism in CsI:Tl. A hot cloud of free charge carriers is created in the first stage after the interaction with a gamma photon. The process of track creation is extremely fast, and it takes less than one picosecond for a high energy electron ($\approx$ 1 MeV) to come to a full stop. Within next 50 femtosecond free holes become self trapped (STH$^+$). Because STH$^+$ have very low mobility, they stay close to the initial track core. The cloud of free hot electrons expands at this time and we observe charge separation: positively charged STH$^+$ stay behind close to the linear track, while electrons expand and fly-away. After around 4 picoseconds free electrons lose their initial kinetic energy through a phonon inelastic scattering mechanism and start to experience a Coulomb attraction to the track of STH$^+$ left behind. Thermalized electrons on the way back towards STH$^+$ can be trapped by Tl$^+$ centers and form Tl^0. At the same time STH$^+$ start to diffuse around the initial track, and some of

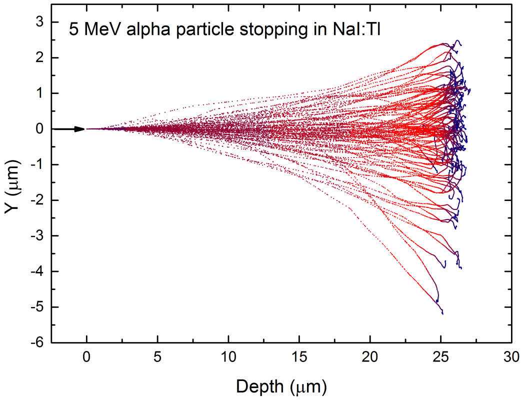

Figure 1.5: Simulation of ionization tracks of 5 MeV alpha particles stopping in NaI:Tl.

them are trapped to form Tl^{2+} centers. At this stage the recombination becomes limited by de-trapping of electrons from Tl^0, and holes from Tl^{2+}. Some of the electrons which were not captured at Tl^0 can directly recombine with Tl^{2+} centers leading to prompt luminescence. The delayed luminescence will come from the electrons detrapped later from Tl^0.

1.5. NON-PROPORTIONAL RESPONSE

As it was already mentioned in paragraph 1.2, the amount of emitted light by a scintillator is not strictly proportional to the energy of the incident particle. It does not seem to be a big concern for spectroscopic application, as it is easily possible to calibrate the energy response and correct for that later. However, there is a much deeper concern arising from the deviation from linearity. Radiation interaction with matter and the following scintillation process are stochastic in nature. Every scintillation event, even if it is caused by a mono-energetic particle, has some variations in a track structure, branching, and the final ionization density. If we consider that the light response of a scintillator is non-linear, than these variations in a track structure lead to variations in the light yield. Finally, the ability to measure energy of the incoming particle is affected by the degree of scintillator's non-proportionality. This has tremendous consequences for nuclear spectroscopy, as non-proportional scintillators have low energy resolution and limited ability to distinguish different incoming energies.

Fig. 1.7 shows non-proportionality of response of NaI:Tl, $LaBr_3$:Ce, $LaBr_3$:Ce,Sr, and Lu_2SiO_5:Ce (LSO) scintillators excited with synchrotron radiation and normalized to the value at 662 keV of gamma excitation. The perfect response is no deviation from linearity, so the light yield per unit energy stays constant despite the energy of the incoming radiation. NaI:Tl and Lu_2SiO_5:Ce deviate the most from 100% value, and these materials have limited energy resolution: 7-8% and 8-9% at 662 keV of gamma excitation, correspondingly [9, 10]. $LaBr_3$:Ce, $LaBr_3$:Ce,Sr are one of the highest energy resolution

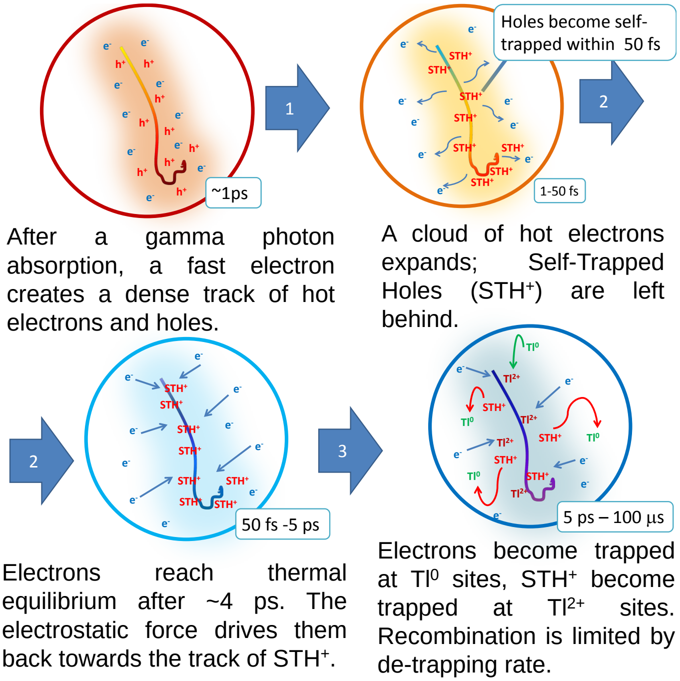

Holes become self-trapped within 50 fs

~1ps

1-50 fs

50 fs -5 ps

5 ps – 100 µs

After a gamma photon absorption, a fast electron creates a dense track of hot electrons and holes.

A cloud of hot electrons expands; Self-Trapped Holes (STH^+) are left behind.

Electrons reach thermal equilibrium after ~4 ps. The electrostatic force drives them back towards the track of STH^+.

Electrons become trapped at Tl^0 sites, STH^+ become trapped at Tl^{2+} sites. Recombination is limited by de-trapping rate.

Figure 1.6: Scintillation mechanism in CsI:Tl

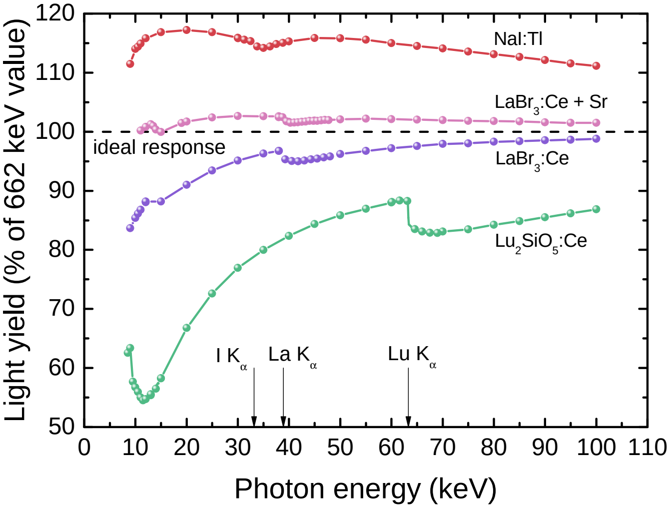

Figure 1.7: Light yield of NaI:Tl, LaBr$_3$:Ce, LaBr$_3$:Ce,Sr, and Lu$_2$SiO$_5$:Ce (LSO) excited with synchrotron radiation and normalized to the value at 662 keV of gamma excitation. Data on LaBr$_3$:Ce, LaBr$_3$:Ce,Sr reproduced from [7, 12], and on NaI:Tl and LSO from [13].

scintillators known currently, 2.7-3.2% and 2% correspondingly [7, 11], see Fig. 1.4.

1.6. THEORETICAL LIMITS OF SCINTILLATION

1.6.1. MAXIMUM LIGHT YIELD WITH A SCINTILLATOR

After photoelectric absorption of a high energy γ-photon an energetic electron is created. It looses energy by collisions with the material electrons leading to ionization of the absorption medium. However, the lowest amount of energy required to create an electron-hole pair is not equal to the material bandgap E_g. Because of momentum conservation, the mean energy necessary for the formation of one pair is $\beta \cdot E_g$, where β in an empirical material-dependent parameter equal around 2.3-2.5 for most of inorganic halide scintillators [14]. Then, the maximum number of electron-hole pairs is given by

$$N_{eh} = \frac{E_\gamma}{\beta E_g} \tag{1.1}$$

where E_γ is the energy of the absorbed γ-photon. If we assume the ideal case when all electron-hole pairs are converted to visible photons, then Eq. 1.1 becomes the theoretical limit for the maximum light yield. Eq. 1.1 shows that a small bandgap is preferred for obtaining higher light yield.

Fig. 1.8 shows light yield of different scintillators versus the bandgap energy E_g. The theoretical limit predicted by Eq. 1.1 with β assumed to be 2.5 is marked with the dashed line. Fluoride scintillators tend to have a large bandgap and consequently their light yield is rather low. Iodides are found on the other end of the bandgap range and have smaller bandgaps and higher light yields. We can conclude that the highest light yields

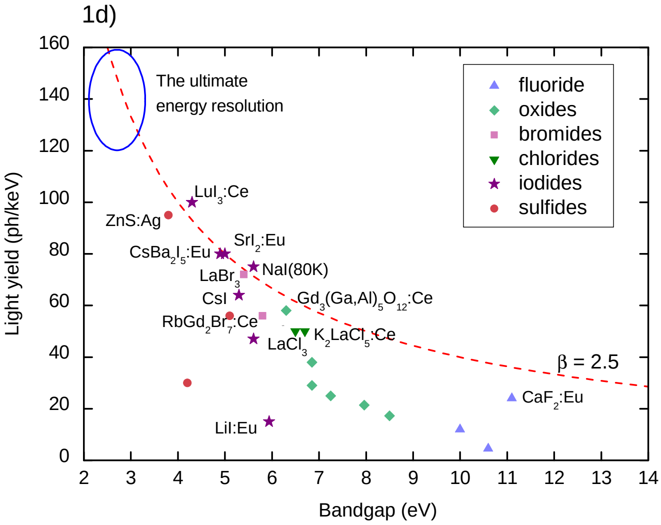

Figure 1.8: Light yield of different scintillators versus the bandgap energy E_g with theoretical limit (dashed line).

can be obtained from low bandgap materials like iodides and sulfides. The bangap range between 2 and 3 eV is the ultimate range for obtaining the highest light yield and consequently the best energy resolution. The connection between energy resolution and light yield will be discussed in the next paragraph.

1.6.2. ENERGY RESOLUTION

The energy resolution R is a parameter which quantifies an ability of a detector to distinguish radiation of different energy. The energy resolution value is usually expressed as a full width maximum ΔE of the mono-energy peak in a pulse-height spectrum divided by the peak position E:

$$R = \frac{\Delta E}{E} \tag{1.2}$$

A naïve thinking may suggest that the energy resolution of a scintillator is limited only by counting statistics of the photodetector used for collection of the scintillation light. Unfortunately, it is not the only one limiting factor, and the energy resolution of scintillators is limited by a few more factors. R can be written as a sum of different contributions:

$$R^2 = R_M^2 + R_{intr}^2 + R_{inh}^2 + R_{tr}^2. \tag{1.3}$$

R_M is the well-known Poisson limit (counting statistics) [15]. In case of a scintillator coupled to a PMT, R_M can be expressed as

$$R_M = 2.35\sqrt{\frac{1+v}{N_{phe}}}, \tag{1.4}$$

were v is the variance of the PMT gain and N_{phe} is the number of photoelectrons released by the scintillation pulse from the photocathode of the PMT. The same formula can be applied to different types of detectors like P-I-N diodes, avalanche photodiodes, but with different values of ν. For PMTs $\nu \approx 0.1$-0.2. R_{intr} is the so called intrinsic energy resolution and is related to a non-proportional response of the scintillator. Creation of an ionization track is a stochastic process, so any non-linearity of the light yield results in additional broadening of the photopeak. R_{inh} is a factor introduced by inhomogeneities in the crystal structures, like dopant concentration variations across the crystal. This results in spacial dependence of the light yield and deteriorates the energy resolution. The last term in Eq. 1.3, R_{tr} refers to additional peak broadening caused by variations in scintillation light transfer to the detector. For example, in long crystals the scintillation photons can have very different optical paths depending if they are absorbed close to the photodetector or far from it. Photons which travel longer paths have higher chance of being lost on the way to the photodetector. This again increases the spread of the number of detected photons.

It was discovered very early that scintillators have non-linear response to the exciting radiation. This fact was quickly connected with deterioration of the energy resolution obtained with scintillators, and sparked systematic studies of this phenomenon. Through the years, more and more sophisticated techniques were developed. Starting from using multiple isotopes for characterization of linearity, using the Compton Coincidence Technique and the Scintillator Light Yield Non-proportionality Characterization Instrument (SLYNCI), and recently K-dip spectroscopy. It became clear that the phenomenon of non-proportionality is related to most fundamental processes of scintillation. Despite that different models have been developed to explain non-proportionality, its origin is not well understood yet.

1.6.3. ENERGY RESOLUTION WITH AN APD

The energy resolution R of a scintillator coupled to an APD can be written as

$$R^2 = R^2_{intr} + R^2_{av} + R^2_{noise} + R^2_{inh}, \tag{1.5}$$

where $R_{av} = 2.35\sqrt{F/N_{eh}}$ is the contribution from the APD avalanche gain fluctuations and from counting statistics, $R_{noise} = 2.35\sigma_{noise}/N_{eh}$ is a contribution from the APD noise [16]. F is the excess noise factor of an APD and N_{eh} is the number of electron-hole pairs generated in the APD by a scintillation pulse. σ_{noise} is the standard deviation in the noise contribution arising from surface and bulk charge recombination of an APD and expressed in RMS electrons.

1.7. THESIS OUTLINE

As we discussed, multiple requirements have to be met at the same time for obtaining a high energy resolution scintillator: high light yield, high proportionality, good matching of the emission wavelength and the photo-detector sensitivity, and high uniformity of a crystal and light collection. All these issues (with exception of crystal quality) will be addressed in this thesis in order to obtain the ultimate energy resolution of a scintillating detector.

Nonproportionality of scintillators is one of the important limiting factors for improving energy resolution. Despite many years of research the origin of this phenomenon is not fully understood. To study nonproportionality multiple measurement methods were developed like Compton-electron coincidence detection and K-dip spectroscopy. Despite being powerful, these methods are complicate, costly, and time-consuming. In Chapter 2 we investigate the interaction of alpha particles with scintillators and conclude that the so called alpha/beta ratio can be used for characterizing nonproportionality. It was found that the materials with high alpha/beta ratio are also characterized with good proportionality of gamma and electron response.

In Chapter 3 we investigate the internal contamination of lanthanum-based scintillators using modern digital spectroscopy methods. This made possible to deconvolve internal alpha peaks and separate them from gamma-photon background. We found that this method can be used for investigating of crystal non-homogeneities at micrometer level as alpha particles have short interaction range of 20-30 μm. This type of measurement allows to avoid surface effects related to short range of alpha particles and enables precise measurement of the alpha/beta ratio. Chapter 4 presents a newly developed fully-digital nuclear spectroscopy used for characterizing scintillation pulse shape change with density of excitation. The measured time profiles were find to agree well with the theoretically predicted curves simulated by Lu et al. [17]. This was an independent confirmation of the most recent model of scintillation mechanism in CsI:Tl. The knowledge about high proportionality of halide scintillators derived in the Chapter 1 was used in Chapter 5 to discover a new highly proportional near-infrared scintillator. As already discussed, materials with infrared emission can be used together with silicon-based photodectors for exploiting almost 100% quantum efficiency of scintillation light detection and minimizing Poison contribution to energy resolution. In Chapter 6 we studied the requirements for obtaining fast spin-allowed 5d-4f emission of samarium which is a promising dopant for developing new near-infrared scintillators. The chapter concludes with a list of candidate materials for scintillators with fast samarium emission. In Chapter 7 we have studied the proposed candidates by means of optical and scintillation spectroscopy and characterized them with optical and nuclear methods.

REFERENCES

[1] N. Coron, E. García, J. Gironnet, J. Leblanc, P. de Marcillac, M. Martínez, Y. Ortigoza, A. O. de Solórzano, C. Pobes, J. Puimedón, T. Redon, M. Sarsa, L. Torres, and J. Villar, *"A BGO scintillating bolometer as dark matter detector prototype",* Optical Materials **31**, 1393 (2009), including Special Issue: Papers from the Fourth Workshop on Cryogenic Scintillation CryoScint08.

[2] C. Arnaboldi, S. Capelli, O. Cremonesi, L. Gironi, M. Pavan, G. Pessina, and S. Pirro, *Characterization of ZnSe scintillating bolometers for double beta decay,* Astroparticle Physics **34**, 344 (2011).

[3] C. Arnaboldi, J. Beeman, O. Cremonesi, L. Gironi, M. Pavan, G. Pessina, S. Pirro, and E. Previtali, *$CdWO_4$ scintillating bolometer for double beta decay: Light and heat anticorrelation, light yield and quenching factors,* Astroparticle Physics **34**, 143 (2010).

[4] A. Alessandrello, V. Bashkirov, C. Brofferio, C. Bucci, D. Camin, O. Cremonesi, E. Fiorini, G. Gervasio, A. Giuliani, A. Nucciotti, M. Pavan, G. Pessina, E. Previ-

tali, and L. Zanotti, *A scintillating bolometer for experiments on double beta decay,* Physics Letters B **420**, 109 (1998).

[5] T. M. Undagoitia and L. Rauch, *Dark matter direct-detection experiments,* Journal of Physics G: Nuclear and Particle Physics **43**, 013001 (2015).

[6] Y. Ortigoza, N. Coron, C. Cuesta, E. García, C. Ginestra, J. Gironnet, P. de Marcillac, M. Martínez, C. Pobes, J. Puimedón, T. Redon, M. Sarsa, L. Torres, and J. Villar, *"Energy partition in sapphire and BGO scintillating bolometers",* Astroparticle Physics **34**, 603 (2011).

[7] M. S. Alekhin, D. A. Biner, K. W. Krämer, and P. Dorenbos, *Improvement of* $LaBr_3$*:5%Ce scintillation properties by* Li^+, Na^+, Mg^{2+}, Ca^{2+}, Sr^{2+}, *and* Ba^{2+} *co-doping,* Journal of Applied Physics **113**, 224904 (2013).

[8] J. F. Ziegler, M. Ziegler, and J. Biersack, *SRIM – the stopping and range of ions in matter (2010),* Nuclear Instruments and Methods in Physics Research Section B: Beam Interactions with Materials and Atoms **268**, 1818 (2010), 19th International Conference on Ion Beam Analysis.

[9] E. Sakai, *Recent measurements on scintillator-photodetector systems,* IEEE Transactions on Nuclear Science **34**, 418 (1987).

[10] C. L. Melcher, J. S. Schweitzer, C. A. Peterson, R. A. Manente, and H. Suzuki, *Crystal growth and scintillation properties of the rare earth orthosilicates.* (Delft University Press (SCINT95)s, 1996) pp. 309–315.

[11] P. R. Menge, G. Gautier, A. Iltis, C. Rozsa, and V. Solovyev, *Performance of large lanthanum bromide scintillators,* Nuclear Instruments and Methods in Physics Research Section A: Accelerators, Spectrometers, Detectors and Associated Equipment **579**, 6 (2007), proceedings of the 11th Symposium on Radiation Measurements and Applications.

[12] M. S. Alekhin, J. T. M. de Haas, I. V. Khodyuk, K. W. Krämer, P. R. Menge, V. Ouspenski, and P. Dorenbos, *Improvement of* γ*-ray energy resolution of* $LaBr_3$*:*Ce^{3+} *scintillation detectors by* Sr^{2+} *and* Ca^{2+} *co-doping,* Applied Physics Letters **102**, 161915 (2013).

[13] I. V. Khodyuk and P. Dorenbos, *Trends and patterns of scintillator nonproportionality,* IEEE Transactions on Nuclear Science **59**, 3320 (2012).

[14] P. A. Rodnyi, *Physical processes in inorganic scintillators,* Vol. 14 (CRC press, 1997).

[15] P. Dorenbos, J. de Haas, and C. van Eijk, *Non-proportionality in the scintillation response and the energy resolution obtainable with scintillation crystals,* IEEE Transactions on Nuclear Science **42**, 2190 (1995).

[16] M. Moszyński, M. Szawłowski, M. Kapusta, and M. Balcerzyk, *Large area avalanche photodiodes in scintillation and x-rays detection,* Nuclear Instruments and Methods in Physics Research Section A: Accelerators, Spectrometers, Detectors and Associated Equipment **485**, 504 (2002).

[17] X. Lu, S. Gridin, R. T. Williams, M. R. Mayhugh, A. Gektin, A. Syntfeld-Każuch, L. Świderski, and M. Moszyński, *Energy-Dependent Scintillation Pulse Shape and Proportionality of Decay Components for CsI:Tl: Modeling with Transport and Rate Equations,* Phys. Rev. Applied **7**, 014007 (2017).

2

NON-PROPORTIONAL RESPONSE OF SCINTILLATORS TO ALPHA PARTICLE EXCITATION

To know that we know what we know,
and to know that we do not know what we do not know,
that is true knowledge.

Nicolaus Copernicus

In this work we investigated the relation between gamma nonproportionality and alpha particle nonproportionality. Firstly, we collected literature data on the α/β ratio of almost all commonly used scintillators. Secondly, we extended the literature review with our own measurements of $LaBr_3$:Ce α/β ratio in function of Ce^{3+} concentration. A strong influence of co-doping on the α/β ratio of $LaBr_3$:Ce has been observed. Finally, we conclude that the gamma nonproportionality, gamma intrinsic energy resolution, and α particle response are closely related to each other, and they are due to quenching in the high density part of ionization tracks. Though it still needs to be tested for a larger group of scintillators, the α/β ratio can be used as a single value characterizing intensity of light quenching processes in scintillators.

This chapter is adapted from: **W. Wolszczak** and P. Dorenbos, "*Nonproportional Response of Scintillators to Alpha Particle Excitation*," in IEEE Transactions on Nuclear Science, vol. 64, no. 6, pp. 1580-1591, June 2017. `https://doi.org/10.1109/TNS.2017.2699327`

2.1. INTRODUCTION

Interest in studying the non-proportionality of the response of scintillators to different types of radiation led to development of new and more sophisticated methods of measuring it. Since reporting for the first time of non-proportional response of sodium iodide (NaI:Tl) to γ rays by Pringle in 1950 [1], most of the research until 90ties was done with using multiple radioactive sources and X-ray fluorescence peaks [2]. In 1994 Valentine and Rooney [3, 4] introduced a new method – the Compton Coincidence Technique (CCT). In order to increase the data rate, in 2008 the CCT was further developed by Choong [5, 6] into a second-generation instrument referred to as SLYNCI (Scintillator Light Yield Nonproportionality Compton Instrument). In 2010 Khodyuk et al. developed the K-dip spectroscopy technique for measuring electron nonproportionality starting from energy as low as 30 eV [7].

In all previously mentioned methods, the particle which interacts with the scintillating material is an electron created by the photoelectric or Compton effect. The electron loses it's energy in multiple interactions with matter, creating a dense track of excited electrons, holes, excitons etc. An alternative way to reach high density of excitation is by using particles with higher mass and/or charge than that of electrons.

Alpha particles were not commonly used in scintillator research during last years. The main concern is a short range of alpha particles, which causes that the scintillation yield is very sensitive to surface properties of the studied material. Experimental difficulties arise when measurements are performed in a gas atmosphere, instead of the vacuum, because alpha particles can loose a considerable amount of their energy before reaching the target material.

In our work we focused on internal alpha particle sources to avoid any of the mentioned problems. Since it is difficult to separate some natural occurring alpha isotopes from the used starting materials, the internal contamination with alpha decaying isotopes is common in many scintillators. For instance, the contamination with ^{227}Ac is difficult to avoid in lanthanide-based scintillators due to similar chemical properties of all actinides and lanthanides. The decay chain of ^{227}Ac, besides beta minus decays, is followed by alpha decays of it's daughters: ^{223}Ra, ^{219}Rn, ^{215}Po, ^{211}Bi [8]. Significant amount of the data on internal alpha activity inside scintillators come from particle physics experiments searching for very rare physical processes like two neutrino double beta decay ($2\nu2\beta$) [9] or the dark mater search experiments [10].

In this work we use alpha particles for studying scintillators non-proportionality of the response. Firstly we have collected the available literature data concerning alpha particle interactions with different scintillating materials to discuss general trends and patterns. Wherever it was possible we have used data on measurements performed with internally created alpha particle sources. Secondly, we performed our own measurements of light yield from internally created alpha particles. We have measured the alpha particle response in lanthanum bromide doped with different cerium concentration, and in gadolinium based scintillators: Gd_2SiO_5:Ce (GSO:Ce) and $(Gd,Y)_3(Al,Ga)_5O_{12}$:Ce (GYGAG:Ce). We will combine the collected data from literature and data measured by our own in order to draw general conclusions about the relation between the electron/gamma nonproportionality and the alpha particle response. We used this as a base for combining alpha particle data with electron data on a common stopping power scale.

2.2. EXPERIMENTAL METHODS

The definitions of the α/β ratio and γ-nonproportionality are presented in Appendix 2.6 together with a literature review of general properties of α/β in scintillators.

In addition to the data collected from literature we conducted our own measurements of the α/β ratio. We used the internal contamination of scintillator crystals with alpha-emitting isotopes in order to avoid surface effects. Previous works [11–16] identified actinium 227 as the main contamination of lanthanide-based scintillators.

We have used the highest alpha energy peak of the internal alpha spectrum for calculating the α/β ratio, see Fig. 2.2. This peak is ascribed to ^{215}Po ($E_{\alpha0,0}$ = 7386 keV) and 99.9% of its decays is directly to the ground state of a daughter isotope [17], so there is no additional gamma de-excitation.

The decay of naturally occurring ^{152}Gd isotope was used in measurements of gadolinium-based scintillators: GYGAG:Ce and GSO:Ce. ^{152}Gd has a half-life of $t_{1/2} = 1.08\cdot10^{15}$ years [18] and 0.2% natural abundance. It decays with 100% efficiency by α emission to the ground state of ^{148}Sm:

$$^{152}\text{Gd} \rightarrow\ ^{148}\text{Sm}\ (E_{recoil} = 56.6\ \text{keV}) + \alpha\ (E_\alpha = 2146.9\ \text{keV}). \tag{2.1}$$

Energy of the recoil E_{recoil} in this reaction is very small compared to the energy carried by the α particle, so practically all of the light emitted by the scintillator is due to α excitations. In our evaluation we will consequently omit the contribution of a nuclear recoil to the measured light yield in all materials, and we will use the alpha energy E_α for calculating the α/β ratio.

The intrinsic activity pulse height spectra of studied samples were measured inside a 15 cm thick lead castle to suppress environmental background. The inner side of the lead castle was covered with copper and cadmium to reduce lead X-ray fluorescence. We used a low potassium PMT (ElectronTubes 9266B) to minimize counts from ^{40}K.

Hygroscopic samples, like LaBr$_3$:Ce, were handled inside a nitrogen filled glove box and mounted in a hermetic casing to carry out measurements outside the glove box. Samples were coupled to the PMT with an optical grease and covered with several layers of PTFE tape over the crystal and PMT, the so-called umbrella covering, to maximize light collection. In all measurements 0.5 μs shaping time was used for the spectroscopy amplifier.

2.3. RESULTS

2.3.1. LITERATURE REVIEW

Table 2.1 lists data on the α/β ratio collected from literature together with our own measurements. General trends observed in the presented data are discussed in detail in Appendix 2.6. Fig. 2.1 shows the literature data on α/β as a function of α energy.

2.3.2. INTRINSIC α ACTIVITY

Fig. 2.2 shows intrinsic activity pulse height spectra of LaCl$_3$:Ce, LaBr$_3$ doped with 5% Ce, LaBr$_3$ doped with 30% Ce, and LaBr$_3$ doped with 5% Ce and 0.1% Sr. All spectra are normalized to the maximum of counts in the lowest energy α peak (mixed ^{223}Ra + ^{227}Th peak), and energy is calibrated with a 662 keV ^{137}Cs γ-source. The activity observed

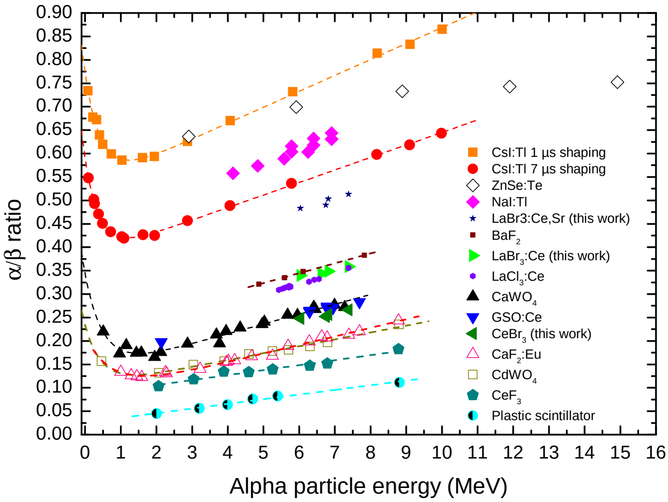

Figure 2.1: α/β ratio in function of alpha particle energy. CsI(Tl) 0.056 mol% Tl [19], ZnSe:Te [20], NaI:Tl [10], BaF$_2$ [21], LaCl$_3$:Ce [13], CaWO$_4$ [22], GSO:Ce [23–25], CaF$_2$:Eu [26], CdWO$_4$ [27], CeF$_3$ [28], polysterene based plastic scintillator [29, 30]. Dashed lines are provided to guide the eye.

above 1.6 MeV gamma equivalent energy is due to alpha particle emission inside the crystal. The same structure of three alpha peaks is observed for all four samples but at different γ-equivalent energy, clearly showing a change of the α/β ratio.

Table 2.1: Overview of scintillators and their properties: density ρ, α/β ratio measured at alpha energy E_α, alpha source used for α/β ratio measurement, light yield at 662 keV gamma energy, intrinsic energy resolution R_{int} for 10 keV and 662 keV γ photons, nonpropotionality of gamma response at 10 keV and reference.

Scintillator	ρ (g/cm^3)	α/β	E_α (MeV)	Source	Light yield (ph/MeV)	R$_{int}$ (% at 662 keV)	R$_{int}$ (% at 10 keV)	NonPR (% at 10 keV)	Ref.
CsI A (100 K)	4.5	1.0	4.7	^{241}Am^{E}	108 000^{2d}	4.64^{2d}	21.72^{2d}	104.44^{2d}	[31, 32]
CsI B (100 K)	4.5	1.0	4.7	^{241}Am^{E}	124 000^{2d}	3.74^{2d}	15.76^{2d}	85.48^{2d}	[31, 32]
NaI:Tl	3.7	0.604^{8}	5.789	^{224}Ra^{I}	45 000	5.7^{d}	13.8^{ac}	113.88	[2, 10, 33, 34]
CsI:Tl	4.5	0.573^{Av}	5.46	^{238}Pu^{E}	56 000	5.5^{ac}	14.64^{ac}	112	[33]
CsI:Na	4.5	0.45	5.46	^{238}Pu^{E}	42 000	6.7^{ac}	16.3^{ac}	123.1	[2, 33, 35, 36]
SrI$_2$:Eu	4.6	0.55	7.687	^{214}Po	82 400			102.2^{c}	[9, 37]
ZnSe:Te (0.2% Te)	5.4	0.69^{4}	5.48	^{241}Am^{E}	28 300	3.3 ^{bd}	25.1^{bd}	87.7^{bd}	[20, 38]
LaBr$_3$:Ce,Sr	5.3	0.513	7.386	^{215}Po^{I}	71 000^{3d}	1.1^{3d}	17.65^{3d}	100.0	[34, 39]
LaBr$_3$:Ce	5.3	0.36	7.386	^{215}Po^{I}	74 000^{3d}	1.8^{3d}	28.1^{3d}	86.6	[34, 39]
LaCl$_3$:Ce	3.9	0.356	7.386	^{215}Po^{I}	35 800^{1d}	2.8^{1d}	23.17^{1d}	83.7	[12]
CeBr$_3$	5.2	0.266	7.386	^{215}Po^{I}	43 000	3.1	25.2	76.4	[15]
BaF$_2$	4.9	0.335	5.59	^{222}Rn^{I}	11 000	4		81.7	[2, 21]
CaF$_2$:Eu	5.7	0.221	5.4	^{232}Th+^{238}U^{Im}	24 000	5.52^{c}	25.0^{c}	79.4	[2, 40, 41]
YAP:Ce	5.4	0.3	5.49	^{241}Am^{E}	17 000	1.3^{1d}		95.2	[42, 43]
YAG:Ce	4.6	0.3	3.94	^{241}Am^{E}	17 000	5.0	26.16	71.4	[44–46]
YAG:Nd	4.6	0.33	5.25	^{241}Am^{E}	3 600				[47]
LuAG:Pr (0.23% Pr)	6.7	0.300^{a}	5.49	^{241}Am^{E}	12 900	3.0	20.7	85.4	[7, 48, 49]
GSO:Ce	6.7	0.265	6.29	^{220}Rn^{I}	8 500	2.7^{d}	35.18^{d3}	68.8	[2, 25, 50]
LuAG:Ce	6.7	0.251^{a}	5.49	^{241}Am^{E}	12 500	4.5	35.8	72.4	[45, 46, 51]
GYGAG:Ce^{7}	5.8	0.242^{8}	2.147	^{152}Gd^{I}	40 000			84.7	[52, 53]
BGO	7.1	0.198	5.3	^{210}Po^{I}	9 000	3.9^{d}	61.48^{4d}	70	[2, 54, 55]
GAGG:Ce^{6}	6.6	0.17^{3}	5.486	^{241}Am^{E}	31 700	5.18^{da}	33.48^{da}	62.9^{da}	[56, 57]
LSO:Ce	7.4	0.14^{5}			23 000	6.6	49.07^{3}	57.00	[2, 34]
BC-400/NE-102	1.0	0.084^{a}	5.3	^{210}Po^{E}					[58]

[8] 0.5 μs shaping [3] 1 μs shaping [a] 2 μs shaping [1] 3 μs shaping [2] 4 μs shaping [b] 10 μs shaping
[4] 12 μs shaping [c] measured with Compton electrons [d] measured with γ photons
[e] measured with K-dip spectroscopy (photoelectrons) [5] unpublished data of M. J. Knitel
[6] Gd$_3$Al$_2$Ga$_3$O$_{12}$:Ce, single crystal [7] (Gd,Y)$_3$(Ga,Al)$_5$O$_{12}$:Ce, ceramic
[E] external α source [I] internal α source [Av] average over available data
[m] linear model fit of ^{232}Th and ^{238}U internal contamination response evaluated at 5.4 MeV [40]

Fig. 2.3 shows the α/β ratio at $E_\alpha = 7386$ keV (^{215}Po) and $E_\gamma = 662$ keV as a function of cerium concentration in LaBr$_3$:Ce scintillator. The α/β ratio has a maximum value of 0.36 around 2.5% of cerium concentration while the lowest is 0.26 for 100% (CeBr$_3$).

The measured α/β ratio values for LaBr$_3$:Ce (5 mol% Ce), LaCl$_3$:Ce (10 mol% Ce), CeBr$_3$, LaBr$_3$:Ce,Sr (5 mol% Ce, 500 ppm Sr), GSO:Ce and GYGAG:Ce are included in

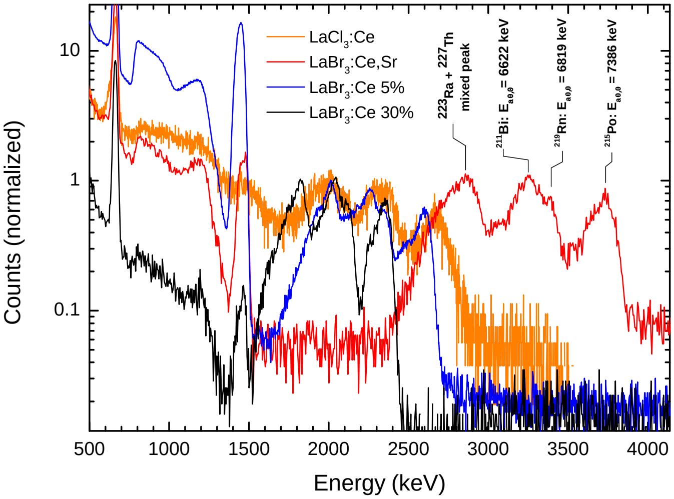

Figure 2.2: Intrinsic activity spectrum of $LaCl_3$:Ce, $LaBr_3$ doped with 5% Ce, $LaBr_3$ doped with 30% Ce, and $LaBr_3$ doped with 5% Ce and 0.1% Sr. Energy was calibrated with 662 keV gammas from ^{137}Cs. Alpha emission energies are according to [17].

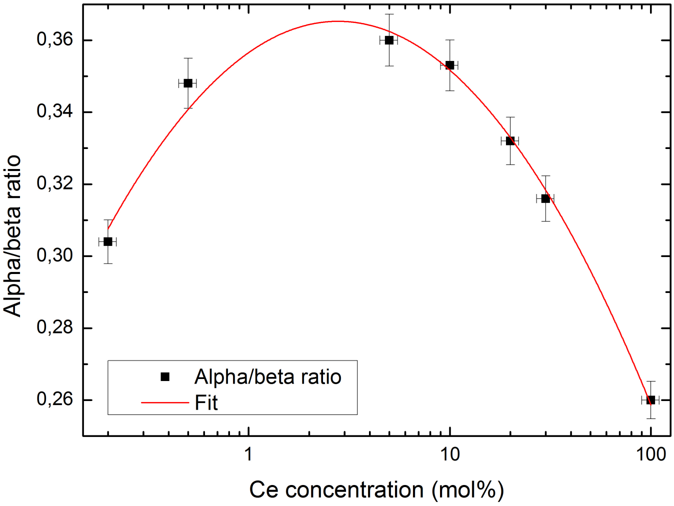

Figure 2.3: α/β ratio of $LaBr_3$:Ce as a function of cerium concentration, measured with internal ^{215}Po contamination, $E_\alpha = 7386$ keV.

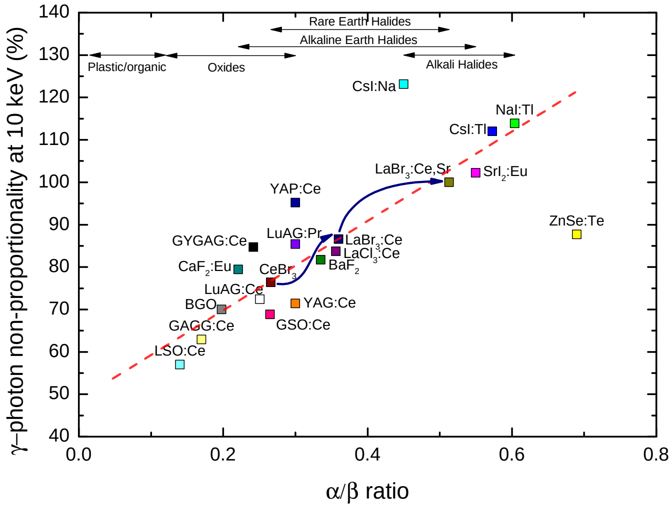

Figure 2.4: Non-proportionality of response at 10 keV of various scintillators in function of their α/β ratio at alpha energies as listed in Table 2.1.

Table 2.1.

2.3.3. NON-PROPORTIONALITY AND α/β RATIO

Fig. 2.4 shows the α/β ratio and gamma photon nonproportionality at 10 keV plotted against each other, based on the data listed in Table 2.1. Gamma energy of 10 keV has been chosen as the lowest gamma energy easily available in the literature for a large group of materials. When data at 10 keV were not available, we used a linear extrapolation from the available nonproportionality curve towards 10 keV. Other reason to chose 10 keV is that the K-edge of most heavy elements in scintillators is at higher energy, which ensures that sudden changes of a photoelectric effect cross section do not influence measurements of the non-proportionality. It is possible to avoid this problem by using electron non-proportionality, but it is not available for a large range of materials.

During collecting the data for Table 2.1 we tried to match experimental conditions of gamma and alpha measurements as closely as possible. For instance, the shaping time has a strong influence on α/β and gamma nonproportionality (see Appendix 2.6.2), so it is important to assure the same shaping time for both measurements.

Despite difficulties with providing the same experimental conditions, a clear trend is observed in Fig. 2.4. A high value of non-proportionality at 10 keV is correlated with a high α/β ratio. We may distinguish three groups of scintillators on this plot. The first group are scintillators with a low value of nonproportionality at 10 keV and low α/β: the oxide scintillators like BGO, GSO:Ce, LSO:Ce, CWO, and the plastic (NE213) scintillator. The second group are mainly rare earth halides ($LaBr_3$:Ce, $LaCl_3$:Ce, $CeBr_3$), and aluminates YAP:Ce and YAG:Ce. The last group are alkali halides CsI:Tl, NaI:Tl, alkaline earth SrI_2:Eu, and co-doped $LaBr_3$:Ce,Sr. They all have a high α/β ratio and high value of non-proportionality at 10 keV. $LaBr_3$:Ce shows that co-doping with Sr not only improves the

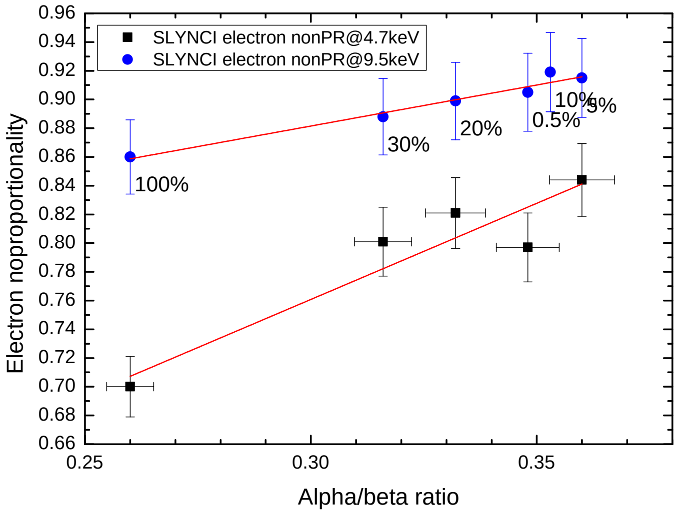

Figure 2.5: Electron nonproportionality of LaBr$_3$:Ce measured with SLYNCI [61] at 4.7 keV and 9.5 keV as a function of the α/β ratio, measured at multiple cerium concentrations. Electron response is normalized to 1 at 450 keV, the α/β at 662 keV gamma equivalent. Values expressed in percent displayed next to data points show the cerium concentration.

non-proportionality and energy resolution but also causes an increase of the α/β ratio.

CsI:Na and ZnSe:Te are far away from the general trend. CsI:Na has a high mobility of sodium near the crystal surface [59], and it is sensitivity to surface finishing and humidity conditions [60] (see Appendix 2.6.2). These factors were probably not carefully considered during measurements and resulted in unreliable α/β. ZnSe:Te is a semiconducting scintillator and quenching processes may follow another trend line characteristic for that type of materials.

The trend marked with dark blue arrows in Fig. 2.4 shows a change of the α/β ratio in series from CeBr$_3$, LaBr$_3$:Ce to LaBr$_3$:Ce,Sr. A small change in chemical composition or defect structure results in significant changes of the α/β ratio and non-proportionality of response.

To further demonstrate the correlation between the α/β ratio, we plotted data measured in this work for LaBr$_3$:Ce with different Ce concentration against non-proportionality measured with SLYNCI [61] at 4.7 and 9.5 keV Compton scattered electron energy. Fig. 2.5 shows clearly that the α/β ratio increases with increase of non-proportionality.

The intrinsic energy resolution R_{int} can be used as a measure of scintillators non-proportionality, although it can be strongly affected by parameters like crystals quality, inhomogeneities, light collection etc. In this work we will follow a definition of intrinsic energy resolution which is simple and commonly used in literature and it is defined as a total energy resolution R_{tot} decreased by a counting statistic limit resolution R_M of a light detector $R_{int}(E) = \sqrt{R_{total}^2 - R_M^2}$. Contribution of a counting uncertainty introduced by a photo-detector is assumed to have a Poisson statistic origin (photon count-

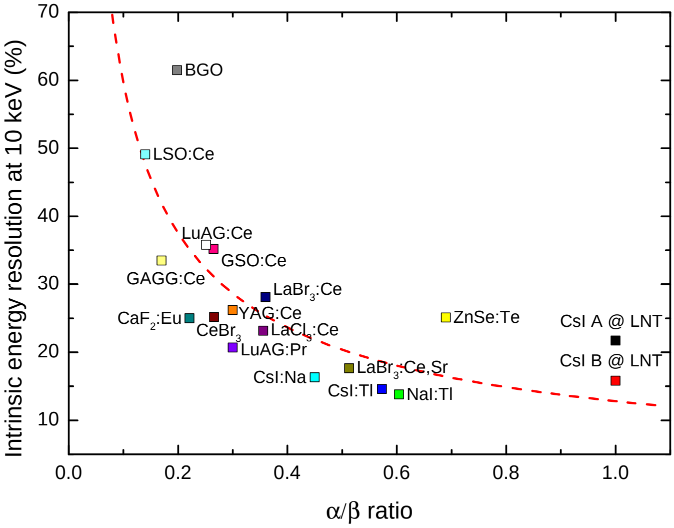

Figure 2.6: Intrinsic energy resolution of various scintillators measured at 10 keV gamma energy against their α/β ratio. The dashed curve is to guide the eye.

ing) and in the case of a photomultiplier tube (PMT) it depends on a light output according to the formula

$$R_M = 2.35\sqrt{\frac{1+\nu(M)}{N_{phe}}}, \tag{2.2}$$

where ν is the excess noise factor caused by multiplier gain variation and N_{phe} is a number of photoelectrons collected from a photocatode. More details on intrinsic energy resolution can be found elsewhere [2].

Fig. 2.6 shows the intrinsic energy resolution measured with gamma photons at 10 keV energy R_{int}(10 keV) versus the α/β ratio (based on data in Table 2.1). Increase of the α/β ratio is correlated with decrease of the intrinsic energy resolution. This trend is also followed by undoped cesium iodide samples CsI at liquid nitrogen temperature. CsI "A" and "B" denotes two different purities placed at the same α/β ratio (exact values were not available).

Fig. 2.7 shows the intrinsic energy resolution measured at 662 keV R_{int}(662 keV) versus the α/β ratio (based on data in Table 2.1). The group of scintillators in the orange ellipse do not follow the trend, and these are only alkali halides and a semiconducting scintillator.

2.4. ANALYSIS AND DISCUSSION

The stopping power $\frac{\mathrm{d}E}{\mathrm{d}x}$ for a charged particle is defined as the differential energy loss $\mathrm{d}E$ divided by the corresponding distance traveled $\mathrm{d}x$. In many theoretical models and experimental analysis of scintillation processes [19, 61–72] the stopping power $\frac{\mathrm{d}E}{\mathrm{d}x}$ is a starting point to evaluate the initial excitation density. Since the electron stopping power

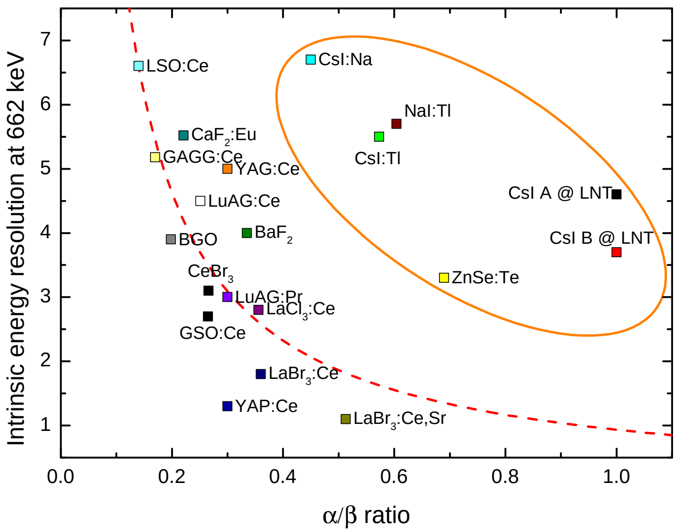

Figure 2.7: Intrinsic energy resolution of various scintillators measured at 662 keV gamma energy against their α/β ratio. The dashed curve is to guide the eye.

is a fundamental parameter for theoretical studies of gamma/electron nonproportionality, one can also consider to use other types of particles to study a high density excitation in scintillation material.

Fig. 2.8 shows the stopping power as a function of kinetic energy of an electron and an alpha particle in sodium iodide, calculated with multiple methods. The databases ASTAR and ESTAR, provided by The National Institute of Standards and Technology (NIST) of the U.S. contain stopping-power tables for alpha particles and electrons. Both databases, ASTAR and ESTAR, generate stopping powers according to International Commission on Radiation Units and Measurements (ICRU) Reports 37 and 49 [73, 74]. Unfortunately, in case of ASTAR, these data are provided only for a certain group of materials and do not include many potentially interesting scintillators. To overcome this limitation, we have used the SRIM package [75] for calculating stopping powers of alpha particles.

Theoretical calculations for electrons were compared with the empirical model of stopping power made by Bizarri [66], which is based on the dielectric theory and optical data from Evaluated Photon Data Library (EPDL97).

For electrons we used a modified Bethe equation as good approximation. An electron stopping power can by approximated by the non-relativistic Bethe equation

$$\frac{\mathrm{d}E}{\mathrm{d}x} = \frac{2\pi q_e^4 N_a \langle \frac{Z}{A} \rangle}{E_{kin}} \ln \frac{1.16(E_{kin} + cI)}{I}, \tag{2.3}$$

where q_e is the elementary charge, ρ is the scintillator density, E_{kin} is kinetic energy of the electron. $< Z/A >$ is average atomic number divided by atomic mass, calculated as weighted sum of the atomic constituents $< Z/A >= \sum_j w_j Z_j / A_j$, where w_j, Z_j and A_j are the fraction by weight, atomic number and mean excitation energy [76]. I is the

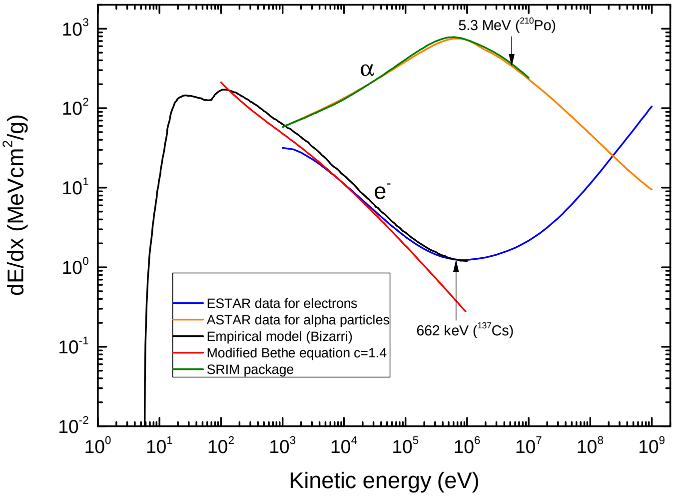

Figure 2.8: Comparison of different models of α particle and electron stopping power dE/dx in sodium iodide. ESTAR and ASTAR databases calculate stopping power according to methods described in ICRU Reports 37 and 49 [73, 74]. Empirical model of Bizarri [66] is based on Evaluated Photon Data Library (EPDL97). SRIM package [75] predictions are based on a quantum mechanical treatment of ion-atom collisions. Energies of popular ^{137}Cs gamma and ^{210}Po alpha sources are indicated.

average ionization energy of the material and was calculated with ESTAR database provided by NIST. Since the Bethe equation is not valid at low energy electrons (< 10 keV) we have introduced coefficient c as an empirical correction. By comparing the Bethe equation with the stopping power derived from optical data for sodium iodide, we have found that $c = 1.4$ is a fair approximation of stopping power at low energies.

Fig. 2.8 shows that the ASTAR data and SRIM package data for alpha particles provide very similar results. The advantage of using alpha particles in nonproportionality measurements is that the stopping process is better understood and provides higher accuracy of $\frac{\mathrm{d}E}{\mathrm{d}x}$ calculations then for electrons. The uncertainty of the alpha particle stopping power at 5.3 MeV is in range between 1% to 4%, while for 10 keV electrons is about 10%. Furthermore, the energy density is much higher while using alpha particles. Fig. 2.8 shows that 5.3 MeV alpha particles (^{210}Po alpha source) have two times higher initial stopping power 350 MeVcm^2/g then electrons in the energy range available in K-dip spectroscopy (30 eV - 70 keV): 170 MeVcm^2/g. At lower energies there are scarce data available for electrons, and it is very difficult to discuss the accuracy. In addition, the cylindrical track model, commonly used in theoretical calculations, is much more appropriate for α particles then for electrons [62].

We used K-dip electron nonproportionality data measured by Khodyuk et al. [7, 53, 77, 78] and converted the electron energy scale to an electron stopping power scale using Eq. 2.3. In case of alpha particles, we have used the literature data already shown on Fig. 2.1, and then we calculated the stopping power with the SRIM package as a function of energy for each scintillator. The maximum stopping power near 1 MeV (Fig. 2.8) corresponds with the minimum α/β in Fig. 2.1 for all studied scintillators.

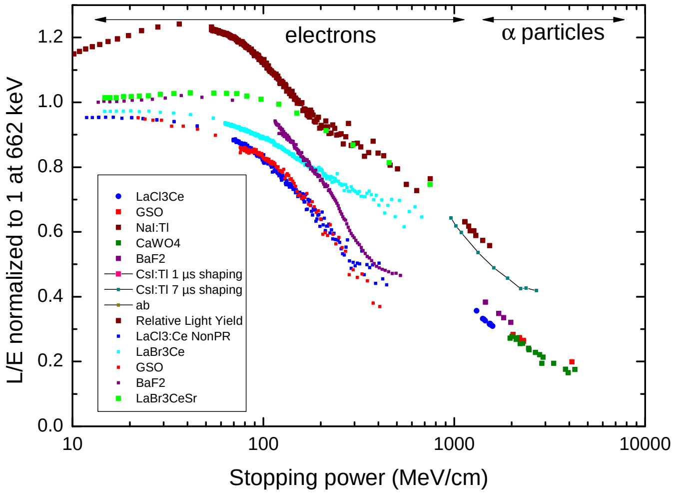

Figure 2.9: Electron data from K-dip spectroscopy displayed together with the α/β ratio on a common stopping power scale. The K-dip data were measured by Khodyuk et al. [7, 53, 77, 78], the alpha data have been already shown with references on Fig. 2.1.

Fig. 2.9 shows both electron and alpha nonproportionality in function of stopping power. The alpha data extends the trends observed in the electron data. Interestingly, the measurements with alpha particles seem to group into two separate classes. The first class is composed of NaI:Tl and CsI:Tl, but also $LaBr_3$:Ce,Sr and SrI_2:Eu can be added to the picture in similar range of the α/β ratio and stopping power. The second group contains GSO:Ce, $CdWO_4$, BaF_2 and $LaCl_3$:Ce. This suggests that at high density excitation we deal with two distinctive and universal trends of nonproportionality, what is not so clear for electron data. However, one may notice that electron responses of GSO:Ce and $LaCl_3$:Ce are also overlapping. Similar situation is observed for electron response of NaI:Tl and $LaBr_3$:Ce,Sr above 150 MeV/cm stopping power.

Fig. 2.6 shows that the intrinsic energy resolution at 10 keV correlates with the α/β ratio for all studied materials. The same is not true for intrinsic energy resolution at 662 keV, see Fig. 2.7, where a group of alkali halides and ZnSe:Te deviates from the general trend. The observed correlation suggests that the same physical processes are responsible for intrinsic energy resolution and light yield quenching at a high density of excitation (low gamma energy) for all studied scintillators. The same is not true at 662 keV excitation for alkali halides. Here a new type of quenching is present at a low density excitation (high gamma energies). Many theoretical models explain the presence of the "hump" in the non-proportionality curve of alkali halides (see NaI:Tl on Fig. 2.9) as an interplay of linear trapping and higher order quenching processes [62, 66]. The deviation of alkali halides in Fig. 2.7 may support statements that the "hump" is a result of charge separation in the electron track and increased trapping at low density excitation in this group of materials.

Latest scintillator's theory development [79] and laser experiments [80] provide a deeper explanation of the above observations. According to Williams and co-workers high energy density quenching is mainly caused by non-radiative annihilation of excitons and energy loss by Auger quenching involving free charge carriers. Exciton annihilation follows second order kinetics, Auger quenching follows third order kinetics. It is expected that materials exhibiting third order of quenching show more proportional response. In laser experiments Grim and co-workers [80] showed that BGO and $CdWO_4$ scintillators exhibit second order quenching. Figure 2.4 and 2.9 shows that these two scintillators are characterized by a low value of nonproportionality and small α/β ratio. Grim also studied SrI_2:Eu which was found to obey third order quenching. Figure 2.4 shows that SrI_2 is among the scintillators with high value of non-proportionality and high α/β ratio. In case of CsI:Tl and NaI:Tl they have found dependence of quenching order on energy of optical excitation. Under 5.9 eV excitation CsI:Tl has a mixed order: 65% of third order and 35% of second order, while NaI:Tl has a second order quenching. Under 6.1 eV excitation CsI:Tl has third order quenching, while NaI:Tl has mixed order 65% of third order and 35% of second order. In case of scintillation caused by high energy electrons, due to momentum conservation of electron-hole pairs we have energies exceeding bandgap energy. Because of that we may expect that quenching order will be similar to that one caused by 6.1 eV photons, so third order for CsI:Tl, and mostly third order for NaI:Tl.

2.5. CONCLUSIONS

We have found that the α/β ratio can be used for characterization of scintillators in the same way as a low energy electron and gamma non-proportionality. In many aspects measurement of the α/β ratio has advantages over other methods. It provides higher precision and higher density of excitation than is available with Compton or photoelectric effect electrons.

It has been shown that the α/β ratio can be used for characterizing scintillation materials, and it follows the same trends and patterns as previously found for nonproportionality of electron/gamma photon response. The α/β ratio also correlates with an intrinsic energy resolution measured with 10 keV gamma photons. Materials with the high α/β ratio have a high intrinsic energy resolution at high energy density excitation. The same trend is observed for 662 keV gamma photons with exception of alkali halides and ZnSe:Te.

Despite what processes are responsible for scintillation energy losses at high energy density excitation, we may conclude that strontium co-doping decreases intensity of quenching in $LaBr_3$:Ce. Interestingly, alkali halides have low intensity of quenching and perform better than $LaBr_3$:Ce and $LaCl_3$:Ce at high density excitation (with α particles or 10 keV electrons). The superiority of $LaBr_3$:Ce and $LaCl_3$:Ce over alkali halides probably comes not from high resistivity to high density quenching, but from lack of a low density quenching which is responsible for the "hump" in electron/gamma nonproportionality.

ACKNOWLEDGMENT

This work was supported by the Dutch Technology Foundation STW, which is part of the Netherlands Organization for Scientific Research (NWO), and which is partly funded by the Ministry of Economic Affairs. This work was partly funded by Saint Gobain Crystals,

France.

2.6. LITERATURE REVIEW ON α RESPONSE

2.6.1. DEFINITION OF THE α/β RATIO

Amount of light produced $L(E)$ per energy E of a particle absorbed in a scintillator varies with the particle energy. Because of historical reasons, in gamma/X-ray photon research of the non-proportional response $nonPR$, the L/E value is usually normalized by L/E measured at energy of 662 keV with ^{137}Cs gamma photons and expressed in percent:

$$nonPR(E) = \frac{\frac{L(E)}{E}}{\frac{L(662\text{ keV})}{662\text{ keV}}} \cdot 100\%. \tag{2.4}$$

The α/β ratio is the ratio of the alpha response to that of electron or gamma ray response in a scintillator. It is defined in a similar way as the electron/gamma/X-ray non-proportionality of response, normalized for light output at certain energy (usually 662 keV), but relating not only an energy, but also a particle type:

$$\alpha/\beta = \frac{\frac{L(E_\alpha)}{E_\alpha}}{\frac{L(E_\beta)}{E_\beta}} \tag{2.5}$$

where $L(E)$ is a light yield (expressed in photons) emitted due to a particle with initial energy E. Indexes stand for particle type [81]. It is assumed that the α/β ratio is identical with the α/γ ratio, because interactions of a gamma photon with a scintillator occurs by the photoelectric effect or Compton scattering leading to an energetic electron which is responsible for the light yield response.

For practical purposes the α/β ratio can be defined as

$$\alpha/\beta = \frac{E_\beta}{E_\alpha}\frac{ch(E_\alpha)_\alpha}{ch(E_\beta)_\beta}, \tag{2.6}$$

where $ch(E_\alpha)_\alpha$ and $ch(E_\beta)_\beta$ are the channel numbers of full absorption peaks on pulse height spectra due to α and β (γ) particles. It means that for $\alpha/\beta < 1$ we observe the α peak in a pulse height spectrum at a channel corresponding to a lower *gamma*-equivalent energy than that of the true alpha particle energy. This effect is usually explained by "high density excitation quenching". Some scintillators have higher immunity to this effect having high α/β ratio and others show much lower efficiency for α radiation than for β (γ).

2.6.2. FACTORS AFFECTING THE α/β RATIO

ALPHA PARTICLE ENERGY

Many researchers reported a dependence of the α/β ratio on the alpha particle energy [10, 19, 20, 22, 82]. Extensive review was done by Tretyak [83] with the aim of using the α/β ratio to predict quenching factors for heavy ions. Some of these results are shown in Fig. 2.1. All $\alpha/\beta(E_\alpha)$ curves share very similar shape, with a minimum around 1 MeV and a linear part starting from 2-3 MeV and going up. The only one exception was found for

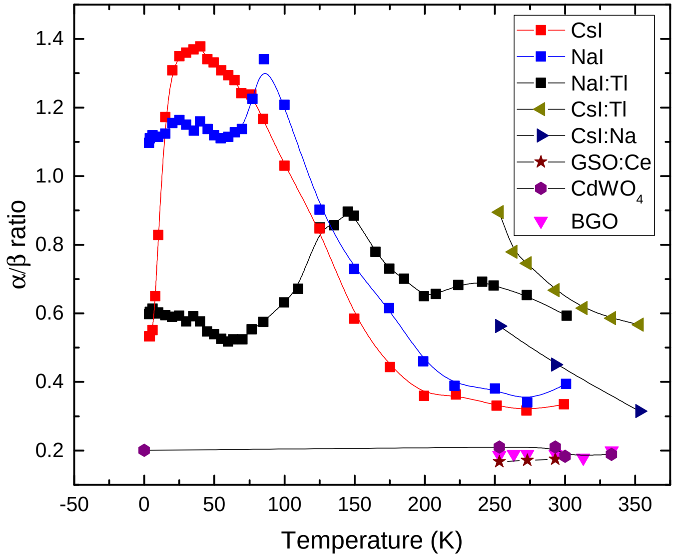

Figure 2.10: α/β ratio as a function of temperature. CsI, NaI, NaI:Tl [31] $E_\alpha = 4.7$ MeV, CsI:Tl, CsI:Na, $CdWO_4$, BGO [35] $E_\alpha = 5.5$ MeV, $CdWO_4$ [84], $CdWO_4$ [27], GSO:Ce [85]. Lines are provided to guide the eye.

the semiconducting scintillator, zinc selenide doped with tellurium ZnSe(Te). The minimum of the α/β ratio curves occurs always at the energy of 1 MeV, which corresponds to the energy of maximum stopping power of alpha particles, compare Fig. 2.8.

Fig. 2.1 shows that for many scintillators the assumption of a linear dependence of the α/β ratio on an alpha energy is justified in energy range from 2.5 to 10 MeV. The slope of the α/β ratio curve is steeper for materials with high α/β ratio, like CsI:Tl, NaI:Tl, and flatter for materials with low α/β ratio like $CaWO_4$, GSO:Ce, $CeBr_3$ or a plastic scintillator. For example $CaWO_4$ has a slope of 0.0125 per MeV, while CsI(Tl) has slope of 0.0311 per MeV. Schumacher and Flammersfeld [82] reported a slope of 0.0099 per MeV in energy range 5.3-8.78 MeV for organic single crystal scintillators (see Appendix 2.6.2).

TEMPERATURE

Fig. 2.10 shows the α/β ratio of multiple scintillators versus temperature. All halide scintillators exhibit strong and complex dependence of α/β on temperature. On the other hand, the α/β ratio of oxide scintillators appears to be very stable and independent of temperature.

An anomalous high α/β ratio has been reported by Arnaboldi et. al [86] for undoped ZnSe scintillator at temperature of 50 mK. It was measured with a 5.7 MeV external alpha source of ^{224}Ra and 2615 keV line of ^{298}Tl, and depending on the size of the detector the α/β ratio was found to be 2.9 for the small crystal (37.5 g), 2.5 for the large (120 g) and 2 for the huge one (337 g). The authors have ascribed this high value to the difference in the light pulse shape for gamma and alpha particles and probable extremely long time scale light emission from gammas.

Concluding, the α/β ratio can be very sensitive to temperature change, leading to a variation of the value by up to a factor of 3. In addition, the light yield due to alpha particles can be much higher than due to gamma particles ($\alpha/\beta > 1$). This is an unexpected observation, because the alpha particles induce higher excitation density compared to gammas, which should lead to higher quenching and a low light yield.

SHAPING TIME

Decrease of the α/β ratio with increase of shaping time was reported for NaI:Tl , CsI:Tl, CsI:Na and ZnSe:Te [19, 35]. For other scintillators like BaF_2, LiI:Eu, BGO, CWO and GSO:Ce the α/β ratio is independent from a shaping time [35]. An example how strong this dependence can be is shown in Fig. 2.1, where $\alpha/\beta(E_\alpha)$ of CsI:Tl has been measured with two shaping times: 1 μs and 7 μs, orange squares and red full circles curves respectively. The difference is almost 0.2 shift between curves.

Kudin et al. [87] has found that increase in shaping time causes decrease of the α/β ratio in CsI:Tl. Especially short shaping times (shorter than 1 μs) result in a large increase in the α/β ratio, up to almost 1 for crystals with high thallium concentration. The strong dependence on the shaping time is caused by a different scintillation pulse shape for an alpha particle and electron excitation. Because gamma-induced scintillation pulses are longer (slower) then alpha-induced, the α/β ratio decreases with increase of the shaping time. This effect is widely used for particle discrimination in scintillators, however its origin is not well understood.

CHEMICAL COMPOSITION

Table 2.1 lists values of the α/β ratio in different scintillating materials together with the energy of used alpha particles, the isotope and type of the source - an internal or external. In addition to that, Table 2.1 compiles the light yield LY measured with 662 keV gamma photons, the intrinsic energy resolution R_{int} at 10 and 662 keV gamma energy, and the gamma photon non-proportionality of response $NonPR$ measured at 10 keV. An intrinsic energy resolution has been calculated as the excess of measured energy resolution above the Poisson limit arising from photon counting. In this section we will discuss the data relevant for the alpha particle response, while details of the gamma photon data will be used later.

Organic and plastic scintillators – The lowest value of α/β in Table 2.1 is for BC-400 plastic scintillator. Similar values were reported for other plastic and liquid (organic) scintillators. Czirr [88] has measured the α/β ratio of liquid scintillator NE213 by dissolving a $^{210}PoCl_4$ alpha source and by evaporating it on the NE102 plastic scintillator surface. The α/β ratio for NE102 was 0.072 and 0.098 for NE213. Galunov [89] has reported measurements with an ^{241}Am external source (E_α = 5.4 MeV) for stilbene 0.05, anthracene 0.04 and p-terphenyl 0.07. These low values in the range from 0.04 to 0.098 show that organic and plastic scintillators do not perform well in alpha-induced high density excitation. Processes responsible for the low light yield are especially severe in these type of materials. More results on the α/β ratio of organic scintillators can be found in Appendix 2.6.2.

Hull et. al [90] reported exceptionally high values of the α/β ratio for a group of organic crystals: stilbene 0.294, anthracene 0.294, diphenylanthracene 0.716, tetraphenylbutadiene 0.225, triphenylbenzene 0.852, salicylamide 0.218. Since these values are extremely far from the literature data and provided by the author without any comment on this discrepancy, we will disregard them.

Oxide scintillators – The oxide scintillators shown in Table 2.1 have α/β in the range from 0.14 for cerium doped lutetium oxyorthosilicate $Lu_2(SiO_4)O$:Ce (LSO:Ce) to 0.33 for neodymium doped yttrium–aluminum garnet $Y_3Al_5O_{12}$:Nd (YAG:Nd). The α/β ratio of gadolinium oxyorthosilicate Gd_2SiO_5:Ce (GSO:Ce) and cerium doped ceramic garnet $(Gd,Y)_3(Al,Ga)_5O_{12}$:Ce (GYGAG:Ce) has been measured at different alpha energy than other scintillators in that group, which most were measured with a 5.49 MeV ^{241}Am source. For fair comparison, we have evaluated their values at 5.49 MeV using the energy dependence slope of 0.0125/MeV in Fig. 2.1, which leads to 0.255 for GSO:Ce and 0.284 for GYGAG:Ce.

The oxide compounds in Table 2.1 are listed in decreasing order of the α/β ratio. The α/β ratio is the lowest for oxyorthosilicates and germanates: LSO:Ce, GSO:Ce, and bismuth germanate $Bi_4Ge_3O_{12}$ (BGO). Interestingly, exchange of lutetium to gadolinium improves the alpha response in case of oxyorthosilicates. The highest alpha/beta ratio is observed in the group of aluminium garnets GYGAG:Ce, LuAG:Ce, LuAG:Pr, YAG:Ce, YAG:Nd and parovskites YAP:Ce. Gadolinium aluminium gallium garnet (GAGG:Ce) has much lower alpha/beta ratio than other garnets, but when gadolinium is partially replaced by yttrium in GYGAG:Ce the α/β ratio increases.

Alkaline earth halide scintillators – Tn this group CaF_2:Eu has the lowest $\alpha/\beta = 0.221$. A higher value of 0.335 has been measure for BaF_2, while the highest value of 0.55 has been reported for SrI_2:Eu.

Rare earth halide scintillators – This group of materials exhibits very interesting properties for studying non-proportionality of scintillators response. $CeBr_3$, $LaBr_3$:Ce, $LaCl_3$:Ce, $LaBr_3$:Ce,Sr have the same crystallographic structure, the luminescence center, very similar electronic structure, density, etc., but despite that, the α/β changes significantly and increases from 0.266 for $CeBr_3$ up to 0.513 for $LaBr_3$:Ce,Sr (see Table 2.1). Especially intriguing is the change of the α/β ratio between $LaBr_3$:Ce 0.36 to 0.513 for Sr co-doped $LaBr_3$:Ce,Sr. This means that the small addition of co-dopant (500 ppm of Sr) significantly changes the response of the material to a high density of excitation. A small addition of co-dopant changes the α/β ratio to a value typical for alkali halide scintillators (see below). On the other hand CeF_3 has very low α/β ratio of 0.183 [28] (internal ^{212}Po, $E_\alpha = 8.8$ MeV), much different than other compounds in this group.

Because of very similar properties and clear change of the α/β ratio this group of materials can be used as a workbench for studying quenching processes at high density excitation. Later in this work we will use $CeBr_3$ - $LaBr_3$:Ce system for studying the relation between the α/β and electron non-proportional response (see Section 2.3.3).

Alkali halide scintillators – One of the highest values of the α/β ratio have been observed for alkali halides. For doped materials the α/β ratio is in range between 0.45 for CsI:Na and 0.604 for NaI:Tl. Much higher values, even exceeding unity, have been reported for pure alkali halides at cryogenic temperatures (see Appendix 2.6.2).

Semiconductor scintillators – There are scarce data available on the α/β ratio of semiconducting scintillators. The only one example presented in Table 2.1 is zinc selenide doped with tellurium and it has the α/β ratio of 0.69, in the same range as that of alkali halide scintillators.

Noble gas scintillators – Very high values of the α/β ratio were found for noble gas scintillators. Value of 0.99 has been reported for 5.49 MeV alphas measured with 10 bar high-pressure xenon gas scintillator [91]. Tanaka et. al [92] measured an α/β ratio equal 0.78 in liquid xenon with 5.3 MeV alphas. Similar results of the α/β ratio were obtained by Peiffer et. al [93] with liquid argon: 0.85 with 7.68 MeV alpha particles from internal ^{214}Po contamination, in respect to 2.614 MeV gammas from the ^{228}Th source.

DIRECTIONAL ANISOTROPY

For multiple materials a dependence of the alpha/beta ratio on the incidence direction of the alpha beam has been found. Heckmann [94] reported that in case of anthracene the ratio of the maximum light yield, measured with α particle beam direction perpendicular to the main cleaving plane *ab*, to the minimum, measured parallel to the axis *a*, is about 1.55 at an α energy of 5.3 MeV. Since the light yield measured with electrons does not depend on electron direction this results in a change of the α/β ratio.

Schumacher and Flammersfeld [82] studied the directional dependence of the α/β ratio of multiple organic single crystal scintillators. Light yield due to alpha excitation has been measured with the 8.78 MeV alpha energy line from a ThC source and the electron light yield has been measured with the Compton edge of a 842 keV ^{54}Mn gamma source. The results are reproduced in Table 2.2. In Appendix 2.6.2 it has been shown that the α/β ratio of organic scintillators is rather low when compared to other scintillators in Table 2.1. Schumacher and Flammersfeld noticed that their results are higher when compared with literature data. This was successfully explained by the dependence of the α/β ratio on alpha particle energy used in experiment (energy dependence of the α/β ratio has been discussed in Appendix 2.6.2). In their experiments a 8.78 MeV alpha source has been used, while many other measurements were done with a 5.3 MeV ^{210}Po alpha source. They found that the α/β ratio of organic scintillators is 40% higher when measured at $E_\alpha = 8.78$ MeV, compared to $E_\alpha = 5.3$ MeV. Taking into account the above fact, the results of the α/β measurements shown in Table 2.2 are in good agreement with previously discussed data.

Some angles of incidence leads to higher α/β ratio: for example the maximum value of 0.156 for athracene is measured with the alpha beam parallel to the c' axes, while in the case of terphenyl the α/β ratio maximum is equal to 0.192 along the *a* axes. The highest difference between directions is observed for naphthalene, the α/β ratio is almost 70% higher when incidence beam is parallel to the c' axes, than when measured parallel to the *b* axes.

Danevich et. al [27] have measured the α/β ratio of cadmium tungstate $CdWO_4$ by irradiating it with α particles in three directions perpendicular to the (010), (001) and (100) crystal planes (directions 1,2 and 3 respectively). Energy of the α particles from external ^{241}Am source was adjusted by using different sets of absorbers. The difference of the α/β ratio between directions was the most pronounced at the lowest alpha energy of $E_\alpha = 2.07$ MeV: 0.13 for the direction 1, 0.09 for the direction 3 and 0.07 for the direction 2. At the alpha energy of $E_\alpha = 5.25$ MeV the relative difference of the α/β measured at different directions become smaller: 0.19 for the direction 1, 0.15 for the direction 3 and 0.14 for the direction 2.

An analogues study has been done for $ZnWO_4$ [95]. The α/β measured at the alpha

Table 2.2: The α/β ratio of organic scintillators measured with the alpha beam direction parallel to main crystallographic axes: c', b and a. Column two refers to light yield measurements with Compton electrons, normalized to 100 for anthracene. Data reproduced from Schumacher and Flammersfeld [82].

Scintillator	Light yield	$(\alpha/\beta)_{c'}$	$(\alpha/\beta)_b$	$(\alpha/\beta)_a$
Anthracen	100	0.156	0.104	0.132
Naphtalene	20	0.139	0.082	0.074
Terphenyl	36	0.154	0.175	0.192
Diphenyl	20	0.156	0.137	0.179
Diphenylenoxid	36	0.152	0.119	0.154
Fluoren	27	0.132	0.179	0.182
Plastic NE102	44	0.124		

energy of $E_\alpha = 2$ MeV at different direction was: 0.15 for the direction 1, 0.085 for the direction 3 and the lowest, 0.075 for the direction 2.

Dependence on direction of the alpha irradiation was not found for YAG:Nd [47] and CeF_3 [28].

CO-DOPING

Co-doping is a procedure where a small amount of an impurity is added to the scintillator leading to improvement of a light yield, an energy resolution or a non-proportionality, but the impurity is not a luminescence center itself. Such effect has been reported by Bardelli et. al [96] for $PbWO_4$ for which the α/β ratio of undoped material is 0.22 and co-doped with F, Gd and Mo it increases to 0.29 when measured with internal ^{210}Po contamination. Besides improving the α/β ratio also the light yield improves approximately by a factor of 1.5-3. Yang et al. [97] showed that $LaBr_3$:Ce co-doped with calcium or strontium has higher α/β ratio than non co-doped material. Also the difference between pulse shape due to alpha or gamma particles becomes significantly bigger in LaB_3:Ce,Ca and LaB_3:Ce,Sr, which improves pulse shape discrimination.

In contrary, boron co-doping of $Gd_3Ga_3Al_2O_{12}$:Ce does not increase the α/β ratio [98]. Probably, in this case energy resolution improvement is not caused by improved proportionality of response, but due to a reduced self-absorption of the scintillation light, and in the result, increased light yield.

DOPANT CONCENTRATION

Yanagida et. al [49] has studied the α/β ratio of ceramic lutetium-aluminium garnet $Lu_3Al_5O_{12}$:Pr (LuAG:Pr) as a function of praseodymium concentration. The α/β ratio increases with Pr concentration from 0.300 at 0.22 mol% to 0.346 at 0.7 mol% and then slightly decreases to 0.340 at 1 mol% Pr.

Kudin et. al [87] has studied dependence of the α/β ratio on Tl concentration in CsI:Tl in 0.02 - 0.35 mol% range. The α/β ratio increases with increase of Tl concentration and reaches maximum for the highest studied Tl concentration. The maximum value is strongly dependent on shaping time, for 12.8 μs $\alpha/\beta = 0.55$, for 0.2 μs $\alpha/\beta = 0.99$ (influence of shaping time has been discussed in Appendix 2.6.2).

SURFACE FINISHING

Simulation with the SRIM package shows that the range of a 5 MeV alpha particle in NaI is 27 μm and the Bragg peak is observed 23 μm from track beginning (own simulation with SRIM package). Any alteration of crystal structure within this depth will easily affect the α/β ratio measurement.

For CsI:Tl and CsI:Na a high sensitivity to a surface finishing was observed [60, 87, 99]. Kudin et al. [87] studied the influence of aging of CsI:Tl for various Tl concentration and found that the α/β ratio is especially sensitive to surface treatment when concentration of Tl is lower than 6×10^{-3} mol%. For this concentration α/β was 0.321 before polishing, 0.505 after polishing, and decreased back to 0.32 after 14 days of aging. Kudin pointed out that increase of the α/β ratio observed for alpha particles with energy lower than 1 MeV reported by Gwin and Murray [19] (also shown of Fig. 2.1), can be explained by deformation-induced point defects in a thin surface-adjacent layer.

Yang et al. have studied the influence of humidity on CsI:Tl and CsI:Na [60] by measuring a radioluminescence with 60 keV gamma source under different humidity conditions. They found that CsI:Tl is less sensitive to moisture then CsI:Na. A CsI:Na crystal after exposure to a high humidity environment (relative humidity higher than 50%) develops "dead" layers from which sodium out-diffuses to the surface. The study of crystallites on the crystal surface with Time-of-Flight Secondary Ion Mass Spectrometer (ToF-SIMS) showed a development of sodium-rich regions. This observations explain exceptionally low $\alpha/\beta = 0.023$ reported by Dinca [59] for CsI:Na. Since "dead" layers develop starting from the surface, a measurement with alpha particles can lead to very low light yield due to a limited depth of penetration, while 662 keV gamma particles can reach the "active" bulk crystal.

REFERENCES

[1] R. W. Pringle and S. Standil, *The gamma-rays from neutron-activated gold,* Phys. Rev. **80**, 762 (1950).

[2] P. Dorenbos, J. de Haas, and C. van Eijk, *Non-proportionality in the scintillation response and the energy resolution obtainable with scintillation crystals,* IEEE Transactions on Nuclear Science **42**, 2190 (1995).

[3] J. D. Valentine and B. D. Rooney, *Design of a compton spectrometer experiment for studying scintillator non-linearity and intrinsic energy resolution,* Nuclear Instruments and Methods in Physics Research Section A: Accelerators, Spectrometers, Detectors and Associated Equipment **353**, 37 (1994).

[4] B. D. Rooney and J. D. Valentine, *Benchmarking the compton coincidence technique for measuring electron response non-proportionality in inorganic scintillators,* in *Nuclear Science Symposium and Medical Imaging Conference Record, 1995., 1995 IEEE*, Vol. 1 (1995) pp. 404–408 vol.1.

[5] W. S. Choong, K. M. Vetter, W. W. Moses, G. Hull, S. A. Payne, N. J. Cherepy, and J. D. Valentine, *Design of a facility for measuring scintillator non-proportionality,* IEEE Transactions on Nuclear Science **55**, 1753 (2008).

[6] W. S. Choong, G. Hull, W. W. Moses, K. M. Vetter, S. A. Payne, N. J. Cherepy, and J. D. Valentine, *Performance of a facility for measuring scintillator non-proportionality,* IEEE Transactions on Nuclear Science **55**, 1073 (2008).

[7] I. V. Khodyuk, J. T. M. de Haas, and P. Dorenbos, *Nonproportional response between 0.1-100 keV energy by means of highly monochromatic synchrotron x-rays,* IEEE Transactions on Nuclear Science **57**, 1175 (2010).

[8] W. Wolszczak and P. Dorenbos, *Shape of intrinsic alpha pulse height spectra in lanthanide halide scintillators,* Nuclear Instruments and Methods in Physics Research Section A: Accelerators, Spectrometers, Detectors and Associated Equipment **857**, 66 (2017).

[9] P. Belli, R. Bernabei, R. Cerulli, F. Danevich, E. Galenin, A. Gektin, A. Incicchitti, V. Isaienko, V. Kobychev, M. Laubenstein, S. Nagorny, R. Podviyanuk, S. Tkachenko, and V. Tretyak, *Radioactive contamination of* SrI_2*(Eu) crystal scintillator,* Nuclear Instruments and Methods in Physics Research Section A: Accelerators, Spectrometers, Detectors and Associated Equipment **670**, 10 (2012).

[10] R. Bernabei, P. Belli, A. Bussolotti, F. Cappella, R. Cerulli, C. Dai, A. d'Angelo, H. He, A. Incicchitti, H. Kuang, J. Ma, A. Mattei, F. Montecchia, F. Nozzoli, D. Prosperi, X. Sheng, and Z. Ye, *The DAMA/LIBRA apparatus,* Nuclear Instruments and Methods in Physics Research Section A: Accelerators, Spectrometers, Detectors and Associated Equipment **592**, 297 (2008).

[11] W. Kernan, *Self-activity in lanthanum halides,* Nuclear Science, IEEE Transactions on **53**, 395 (2006).

[12] M. Balcerzyk, M. Moszyński, and M. Kapusta, *Comparison of* $LaCl_3$*:Ce and NaI(Tl) scintillators in* γ*-ray spectrometry,* Nuclear Instruments and Methods in Physics Research Section A: Accelerators, Spectrometers, Detectors and Associated Equipment **537**, 50 (2005), proceedings of the 7th International Conference on Inorganic Scintillators and their Use in Scientific adn Industrial Applications.

[13] B. Milbrath, R. Runkle, T. Hossbach, W. Kaye, E. Lepel, B. McDonald, and L. Smith, *Characterization of alpha contamination in lanthanum trichloride scintillators using coincidence measurements,* Nuclear Instruments and Methods in Physics Research Section A: Accelerators, Spectrometers, Detectors and Associated Equipment **547**, 504 (2005).

[14] J. Hartwell and R. Gehrke, *Observations on the background spectra of four* $LaCl_3$*(Ce) scintillation detectors,* Applied Radiation and Isotopes **63**, 223 (2005).

[15] F. Quarati, P. Dorenbos, J. van der Biezen, A. Owens, M. Selle, L. Parthier, and P. Schotanus, *Scintillation and detection characteristics of high-sensitivity CeBr3 gamma-ray spectrometers,* Nuclear Instruments and Methods in Physics Research Section A: Accelerators, Spectrometers, Detectors and Associated Equipment **729**, 596 (2013).

[16] G. Lutter, M. Hult, R. Billnert, A. Oberstedt, S. Oberstedt, E. Andreotti, G. Marissens, U. Rosengård, and F. Tzika, *Radiopurity of a CeBr$_3$ crystal used as scintillation detector,* Nuclear Instruments and Methods in Physics Research Section A: Accelerators, Spectrometers, Detectors and Associated Equipment **703**, 158 (2013).

[17] M.-M. Bé, V. Chisté, C. Dulieu, M. Kellett, X. Mougeot, A. Arinc, V. Chechev, N. Kuzmenko, T. Kibédi, A. Luca, and A. Nichols, *Table of Radionuclides*, Monographie BIPM-5, Vol. 8 (Bureau International des Poids et Mesures, Pavillon de Breteuil, F-92310 Sèvres, France, 2016).

[18] N. Nica, *Nuclear data sheets for A = 148,* Nuclear Data Sheets **117**, 1 (2014).

[19] R. Gwin and R. B. Murray, *Scintillation process in CsI(Tl). I. comparison with activator saturation model,* Phys. Rev. **131**, 501 (1963).

[20] W. Klamra, M. Balcerzyk, M. Kapusta, A. Kerek, M. Moszyński, L.-O. Norlin, D. Novák, and G. Possnert, *Studies of scintillation light nonproportionality of ZnSe(Te), CsI(Tl) and YAP(Ce) crystals using heavy ions,* Nuclear Instruments and Methods in Physics Research Section A: Accelerators, Spectrometers, Detectors and Associated Equipment **484**, 327 (2002).

[21] F. Quarati, personal communication.

[22] Y. Zdesenko, F. A. III, V. Brudanin, F. Danevich, S. Nagorny, I. Solsky, and V. Tretyak, *Scintillation properties and radioactive contamination of CaWO$_4$ crystal scintillators,* Nuclear Instruments and Methods in Physics Research Section A: Accelerators, Spectrometers, Detectors and Associated Equipment **538**, 657 (2005).

[23] F. Danevich, A. Georgadze, V. Kobychev, B. Kropivyansky, V. Kuts, V. Muzalevsky, A. Nikolaiko, O. Ponkratenko, A. Prokopets, V. Tretyak, and Y. Zdesenko, *Quest for neutrinoless double beta decay of ^{160}Gd,* Nuclear Physics B - Proceedings Supplements **48**, 235 (1996).

[24] F. Danevich, V. Kobychev, O. Ponkratenko, V. Tretyak, and Y. Zdesenko, *Quest for double beta decay of ^{160}Gd and Ce isotopes,* Nuclear Physics A **694**, 375 (2001).

[25] S. Wang, H. Wong, and M. Fujiwara, *Measurement of intrinsic radioactivity in a GSO crystal,* Nuclear Instruments and Methods in Physics Research Section A: Accelerators, Spectrometers, Detectors and Associated Equipment **479**, 498 (2002).

[26] P. Belli, R. Bernabei, F. Cappella, R. Cerulli, C. Dai, F. Danevich, A. d'Angelo, A. Incicchitti, V. Kobychev, S. Nagorny, S. Nisi, F. Nozzoli, D. Prosperi, V. Tretyak, and S. Yurchenko, *Search for α decay of natural europium,* Nuclear Physics A **789**, 15 (2007).

[27] F. A. Danevich, A. S. Georgadze, V. V. Kobychev, S. S. Nagorny, A. S. Nikolaiko, O. A. Ponkratenko, V. I. Tretyak, S. Y. Zdesenko, Y. G. Zdesenko, P. G. Bizzeti, T. F. Fazzini, and P. R. Maurenzig, *α activity of natural tungsten isotopes,* Phys. Rev. C **67**, 014310 (2003).

[28] P. Belli, R. Bernabei, R. Cerulli, C. Dai, F. Danevich, A. Incicchitti, V. Kobychev, O. Ponkratenko, D. Prosperi, V. Tretyak, and Y. Zdesenko, *Performances of a* CeF_3 *crystal scintillator and its application to the search for rare processes,* Nuclear Instruments and Methods in Physics Research Section A: Accelerators, Spectrometers, Detectors and Associated Equipment **498**, 352 (2003).

[29] J. Argyriades, R. Arnold, C. Augier, J. Baker, A. Barabash, A. Basharina-Freshville, M. Bongrand, C. Bourgeois, D. Breton, M. Brière, G. Broudin-Bay, V. Brudanin, A. Caffrey, S. Carcel, S. Cebrián, A. Chapon, E. Chauveau, T. Dafni, J. Díaz, D. Durand, V. Egorov, J. Evans, R. Flack, K.-I. Fushima, I. Irastorza, X. Garrido, H. Gómez, B. Guillon, A. Holin, J. Hommet, K. Holy, J. Horkey, P. Hubert, C. Hugon, F. Iguaz, N. Ishihara, C. Jackson, S. Jenzer, S. Jullian, M. Kauer, O. Kochetov, S. Konovalov, V. Kovalenko, T. Lamhamdi, K. Lang, Y. Lemière, G. Lutter, G. Luzón, F. Mamedov, C. Marquet, F. Mauger, F. Monrabal, A. Nachab, I. Nasteva, I. Nemchenok, C. Nguyen, M. Nomachi, F. Nova, H. Ohsumi, R. Pahlka, F. Perrot, F. Piquemal, P. Povinec, B. Richards, J. Ricol, C. Riddle, A. Rodríguez, R. Saakyan, X. Sarazin, J. Sedgbeer, L. Serra, Y. Shitov, L. Simard, F. Šimkovic, S. Söldner-Rembold, I. Štekl, C. Sutton, Y. Tamagawa, G. Szklarz, J. Thomas, R. Thompson, V. Timkin, V. Tretyak, V. Tretyak, V. Umatov, L. Vála, I. Vanyushin, R. Vasiliev, V. Vasiliev, V. Vorobel, D. Waters, N. Yahlali, and A. Žukauskas, *Results of the BiPo-1 prototype for radiopurity measurements for the SuperNEMO double beta decay source foils,* Nuclear Instruments and Methods in Physics Research Section A: Accelerators, Spectrometers, Detectors and Associated Equipment **622**, 120 (2010).

[30] M. Bongrand and S. collaboration, *The BiPo detector for ultralow radioactivity measurements,* AIP Conference Proceedings **897**, 14 (2007).

[31] P. Nadeau, *Cryogenic Scintillators for Rare-Event Searches*, Ph.D. thesis, Queen's University, Kingston, Ontario, Canada (2015).

[32] M. Moszyński, M. Balcerzyk, W. Czarnacki, M. Kapusta, W. Klamra, P. Schotanus, A. Syntfeld, M. Szawłowski, and V. Kozlov, *Energy resolution and non-proportionality of the light yield of pure CsI at liquid nitrogen temperatures,* Nuclear Instruments and Methods in Physics Research Section A: Accelerators, Spectrometers, Detectors and Associated Equipment **537**, 357 (2005), proceedings of the 7th International Conference on Inorganic Scintillators and their Use in Scientific adn Industrial Applications.

[33] Ł. Świderski, M. Moszyński, W. Czarnacki, M. Szawłowski, T. Szcześniak, G. Pausch, C. Plettner, K. Roemer, and P. Schotanus, *Gamma-ray and electron response in doped alkali halide scintillators,* in *Nuclear Science Symposium and Medical Imaging Conference (NSS/MIC), 2011 IEEE* (2011) pp. 982–986.

[34] M. S. Alekhin, J. T. M. de Haas, I. V. Khodyuk, K. W. Krämer, P. R. Menge, V. Ouspenski, and P. Dorenbos, *Improvement of* γ*-ray energy resolution of* $LaBr_3{:}Ce^{3+}$ *scintillation detectors by* Sr^{2+} *and* Ca^{2+} *co-doping,* Applied Physics Letters **102**, 161915 (2013).

[35] E. Sysoeva, V. Tarasov, O. Zelenskaya, and V. Sulyga, *The study of α/γ ratio for inorganic scintillation detectors,* Nuclear Instruments and Methods in Physics Research Section A: Accelerators, Spectrometers, Detectors and Associated Equipment **414**, 274 (1998).

[36] W. Chewpraditkul, Ł. Świderski, and M. Moszyński, *Light yield non-proportionality and intrinsic energy resolution of doped CsI scintillators,* Nukleonika **Vol. 53, No. 2**, 51 (2008).

[37] B. W. Sturm, N. J. Cherepy, O. B. Drury, P. A. Thelin, S. E. Fisher, S. P. O'Neal, S. A. Payne, A. Burger, L. A. Boatner, J. O. Ramey, K. S. Shah, and R. Hawrami, *Characteristics of undoped and europium-doped SrI_2 scintillator detectors,* in *Nuclear Science Symposium and Medical Imaging Conference (NSS/MIC), 2011 IEEE* (2011) pp. 7–11.

[38] M. Balcerzyk, W. Klamra, M. Moszyński, M. Kapusta, and M. Szawłowski, *Energy resolution and light yield non-proportionality of ZnSe : Te scintillator studied by large area avalanche photodiodes and photomultipliers,* Nuclear Instruments and Methods in Physics Research Section A: Accelerators, Spectrometers, Detectors and Associated Equipment **482**, 720 (2002).

[39] M. S. Alekhin, D. A. Biner, K. W. Krämer, and P. Dorenbos, *Improvement of $LaBr_3$:5%Ce scintillation properties by Li^+, Na^+, Mg^{2+}, Ca^{2+}, Sr^{2+}, and Ba^{2+} co-doping,* Journal of Applied Physics **113**, 224904 (2013).

[40] P. Belli, R. Bernabei, C. Dai, F. Grianti, H. He, G. Ignesti, A. Incicchitti, H. Kuang, J. Ma, F. Montecchia, O. Ponkratenko, D. Prosperi, V. Tretyak, and Y. Zdesenko, *New limits on spin-dependent coupled WIMPs and on 2β processes in ^{40}Ca and ^{46}Ca by using low radioactive CaF_2(Eu) crystal scintillators,* Nuclear Physics B **563**, 97 (1999).

[41] Ł. Świderski, R. Marcinkowski, M. Moszyński, W. Czarnacki, M. Szawłowski, T. Szcześniak, G. Pausch, C. Plettner, and K. Roemer, *Electron response of some low-Z scintillators in wide energy range,* Journal of Instrumentation **7**, P06011 (2012).

[42] M. Kapusta, M. Balcerzyk, M. Moszyński, and J. Pawelke, *A high-energy resolution observed from a YAP:Ce scintillator,* Nuclear Instruments and Methods in Physics Research Section A: Accelerators, Spectrometers, Detectors and Associated Equipment **421**, 610 (1999).

[43] M. Moszyński, M. Kapusta, D. Wolski, W. Klamra, and B. Cederwall, *Properties of the YAP:Ce scintillator,* Nuclear Instruments and Methods in Physics Research Section A: Accelerators, Spectrometers, Detectors and Associated Equipment **404**, 157 (1998).

[44] M. Moszyński, T. Ludziejewski, D. Wolski, W. Klamra, and L. Norlin, *Properties of the YAG:Ce scintillator,* Nuclear Instruments and Methods in Physics Research Section A: Accelerators, Spectrometers, Detectors and Associated Equipment **345**, 461 (1994).

[45] W. Chewpraditkul, Ł. Świderski, M. Moszyński, T. Szcześniak, A. Syntfeld-Każuch, C. Wanarak, and P. Limsuwan, *Comparative studies of* $Lu_3Al_5O_{12}$*:Ce and* $Y_3Al_5O_{12}$*:Ce scintillators for gamma-ray detection,* physica status solidi (a) **206**, 2599 (2009).

[46] W. Chewpraditkul, Ł. Świderski, M. Moszyński, T. Szcześniak, A. Syntfeld-Każuch, C. Wanarak, and P. Limsuwan, *Scintillation properties of LuAG:Ce, YAG:Ce and LYSO:Ce crystals for gamma-ray detection,* IEEE Transactions on Nuclear Science **56**, 3800 (2009).

[47] F. Danevich, V. Kobychev, S. Nagorny, and V. Tretyak, *YAG:Nd crystals as possible detector to search for and decay of neodymium,* Nuclear Instruments and Methods in Physics Research Section A: Accelerators, Spectrometers, Detectors and Associated Equipment **541**, 583 (2005).

[48] L. Świderski, M. Moszyński, A. Nassalski, A. Syntfeld-Kazuch, T. Szcześniak, K. Kamada, K. Tsutsumi, Y. Usuki, T. Yanagida, and A. Yoshikawa, *Light yield non-proportionality and energy resolution of praseodymium doped LuAG scintillator,* IEEE Transactions on Nuclear Science **56**, 934 (2009).

[49] T. Yanagida, Y. Fujimoto, K. Kamada, D. Totsuka, H. Yagi, T. Yanagitani, Y. Futami, S. Yanagida, S. Kurosawa, Y. Yokota, A. Yoshikawa, and M. Nikl, *Scintillation properties of transparent ceramic Pr:LuAG for different Pr concentration,* IEEE Transactions on Nuclear Science **59**, 2146 (2012).

[50] M. Balcerzyk, M. Moszyński, M. Kapusta, D. Wolski, J. Pawelke, and C. Melcher, *YSO, LSO, GSO and LGSO. A study of energy resolution and nonproportionality.* IEEE Transactions on Nuclear Science **47**, 1319 (2000), Nuclear Science Symposium (NSS), SEATTLE, WASHINGTON, OCT 26-28, 1999.

[51] P. Prusa, T. Cechak, J. A. Mares, M. Nikl, A. Beitlerova, N. Solovieva, Y. V. Zorenko, V. I. Gorbenko, J. Tous, and K. Blazek, *The* α*-particle excited scintillation response of the liquid phase epitaxy grown LuAG:Ce thin films,* Applied Physics Letters **92**, 041903 (2008), http://dx.doi.org/10.1063/1.2835458.

[52] A. Giaz, G. Hull, V. Fossati, N. Cherepy, F. Camera, N. Blasi, S. Brambilla, S. Coelli, B. Million, and S. Riboldi, *Preliminary investigation of scintillator materials properties:* SrI_2*:Eu,* $CeBr_3$ *and GYGAG:Ce for gamma rays up to 9 MeV,* Nuclear Instruments and Methods in Physics Research Section A: Accelerators, Spectrometers, Detectors and Associated Equipment **804**, 212 (2015).

[53] I. V. Khodyuk, *Nonproportionality of inorganic scintillators,* Ph.D. thesis, TU Delft, Uitgeverij BOXPress, Oisterwijk (2013).

[54] M. Moszyński, M. Balcerzyk, W. Czarnacki, M. Kapusta, W. Klamra, A. Syntfeld, and M. Szawłowski, *Intrinsic energy resolution and light yield nonproportionality of BGO,* IEEE Transactions on Nuclear Science **51**, 1074 (2004).

[55] D. Grigoriev, V. Kazanin, G. Kuznetcov, I. Novoselov, P. Schotanus, B. Shavinski, S. Shepelev, V. Shlegel, and Y. Vasiliev, *Alpha radioactive background in BGO crystals,* Nuclear Instruments and Methods in Physics Research Section A: Accelerators, Spectrometers, Detectors and Associated Equipment **623**, 999 (2010).

[56] M. Kobayashi, Y. Tamagawa, S. Tomita, A. Yamamoto, I. Ogawa, and Y. Usuki, *Significantly different pulse shapes for γ- and α-rays in $Gd_3Al_2Ga_3O_{12}:Ce^{3+}$ scintillating crystals,* Nuclear Instruments and Methods in Physics Research Section A: Accelerators, Spectrometers, Detectors and Associated Equipment **694**, 91 (2012).

[57] J. Iwanowska, Ł. Świderski, T. Szcześniak, P. Sibczyński, M. Moszyński, M. Grodzicka, K. Kamada, K. Tsutsumi, Y. Usuki, T. Yanagida, and A. Yoshikawa, *Performance of cerium-doped $Gd_3Al_2Ga_3O_{12}$ (GAGG:Ce) scintillator in gamma-ray spectrometry,* Nuclear Instruments and Methods in Physics Research Section A: Accelerators, Spectrometers, Detectors and Associated Equipment **712**, 34 (2013).

[58] G. Bertolini, A. D. Turco, and G. Restelli, *Alpha-pulse analysis by scintillation detectors,* Nuclear Instruments and Methods **7**, 350 (1960).

[59] L. Dinca, P. Dorenbos, J. de Haas, V. Bom, and C. V. Eijk, *Alpha–gamma pulse shape discrimination in CsI:Tl, CsI:Na and BaF_2 scintillators,* Nuclear Instruments and Methods in Physics Research Section A: Accelerators, Spectrometers, Detectors and Associated Equipment **486**, 141 (2002), proceedings of the 6th International Conference on Inorganic Scin tillators and their Use in Scientific and Industrial Applications.

[60] P. Yang, C. D. Harmon, F. P. Doty, and J. A. Ohlhausen, *Effect of humidity on scintillation performance in Na and Tl activated CsI crystals,* IEEE Transactions on Nuclear Science **61**, 1024 (2014).

[61] S. A. Payne, W. W. Moses, S. Sheets, L. Ahle, N. J. Cherepy, B. Sturm, S. Dazeley, G. Bizarri, and W. S. Choong, *Nonproportionality of scintillator detectors: Theory and experiment,* IEEE Transactions on Nuclear Science **58**, 3392 (2011).

[62] X. Lu, Q. Li, G. A. Bizarri, K. Yang, M. R. Mayhugh, P. R. Menge, and R. T. Williams, *Coupled rate and transport equations modeling proportionality of light yield in high-energy electron tracks: CsI at 295 K and 100 K; CsI:Tl at 295 K,* Phys. Rev. B **92**, 115207 (2015).

[63] S. A. Payne, N. J. Cherepy, G. Hull, J. D. Valentine, W. W. Moses, and W. S. Choong, *Nonproportionality of scintillator detectors: Theory and experiment,* IEEE Transactions on Nuclear Science **56**, 2506 (2009).

[64] S. A. Payne, S. Hunter, L. Ahle, N. J. Cherepy, and E. Swanberg, *Nonproportionality of scintillator detectors. temperature dependence studies,* IEEE Transactions on Nuclear Science **61**, 2771 (2014).

[65] S. A. Payne, *Nonproportionality of scintillator detectors. resolution contribution from delta-rays,* IEEE Transactions on Nuclear Science **62**, 372 (2015).

[66] G. Bizarri, N. J. Cherepy, W. S. Choong, G. Hull, W. W. Moses, S. A. Payne, J. Singh, J. D. Valentine, A. N. Vasilev, and R. T. Williams, *Progress in studying scintillator proportionality: Phenomenological model,* IEEE Transactions on Nuclear Science **56**, 2313 (2009).

[67] I. V. Khodyuk, F. G. A. Quarati, M. S. Alekhin, and P. Dorenbos, *Energy resolution and related charge carrier mobility in LaBr*$_3$*:Ce scintillators,* Journal of Applied Physics **114**, 123510 (2013), http://dx.doi.org/10.1063/1.4823737.

[68] R. Hill and A. J. L. Collinson, *The effect on the scintillation efficiency of NaI(Tl) of changes in the thallium concentration and strain: I. experimental,* British Journal of Applied Physics **17**, 1377 (1966).

[69] A. Meyer and R. B. Murray, *Effect of energetic secondary electrons on the scintillation process in alkali halide crystals,* Phys. Rev. **128**, 98 (1962).

[70] R. Hill, *The effect on the scintillation efficiency of NaI(Tl) of changes in the thallium concentration and strain: Ii. theoretical,* British Journal of Applied Physics **17**, 1385 (1966).

[71] R. B. Murray and A. Meyer, *Scintillation response of activated inorganic crystals to various charged particles,* Phys. Rev. **122**, 815 (1961).

[72] R. Gwin and R. B. Murray, *Scintillation process in CsI(Tl). II. emission spectra and the possible role of self-trapped holes,* Phys. Rev. **131**, 508 (1963).

[73] ICRU(1984), *Stopping Powers for Electrons and Positrons* (ICRU Report 37, 1984).

[74] ICRU(1993), *Stopping Powers and Ranges for Protons and Alpha Particles* (ICRU Report 49, 1993).

[75] J. F. Ziegler, M. Ziegler, and J. Biersack, *SRIM – the stopping and range of ions in matter (2010),* Nuclear Instruments and Methods in Physics Research Section B: Beam Interactions with Materials and Atoms **268**, 1818 (2010), 19th International Conference on Ion Beam Analysis.

[76] S. M. Seltzer and M. J. Berger, *Evaluation of the collision stopping power of elements and compounds for electrons and positrons,* The International Journal of Applied Radiation and Isotopes **33**, 1189 (1982).

[77] I. V. Khodyuk, P. A. Rodnyi, and P. Dorenbos, *Nonproportional scintillation response of NaI:Tl to low energy x-ray photons and electrons,* Journal of Applied Physics **107**, 113513 (2010), http://dx.doi.org/10.1063/1.3431009.

[78] I. V. Khodyuk and P. Dorenbos, *Trends and patterns of scintillator nonproportionality,* IEEE Transactions on Nuclear Science **59**, 3320 (2012).

[79] R. Williams, J. Q. Grim, Q. Li, K. Ucer, G. Bizarri, S. Kerisit, F. Gao, P. Bhattacharya, E. Tupitsyn, E. Rowe, *et al.*, *Experimental and computational results on exciton/free-carrier ratio, hot/thermalized carrier diffusion, and linear/nonlinear rate constants*

affecting scintillator proportionality, in *Hard X-Ray, Gamma-Ray, and Neutron Detector Physics XV,* Vol. 8852 (International Society for Optics and Photonics, 2013) p. 88520J.

[80] J. Q. Grim, K. B. Ucer, A. Burger, P. Bhattacharya, E. Tupitsyn, E. Rowe, V. M. Buliga, L. Trefilova, A. Gektin, G. A. Bizarri, W. W. Moses, and R. T. Williams, *Nonlinear quenching of densely excited states in wide-gap solids,* Phys. Rev. B **87**, 125117 (2013).

[81] J. Birks, *The theory and Practice of Scintillation Counting* (Pergamon Presse Ltd., 1964).

[82] M. Schumacher and A. Flammersfeld, *Szintillationslichtausbeuten organischer molekülkristalle für α-strahlen und elektronen,* Zeitschrift für Physik **178**, 11 (1964).

[83] V. Tretyak, *Semi-empirical calculation of quenching factors for ions in scintillators,* Astroparticle Physics **33**, 40 (2010).

[84] C. Arnaboldi, J. Beeman, O. Cremonesi, L. Gironi, M. Pavan, G. Pessina, S. Pirro, and E. Previtali, *$CdWO_4$ scintillating bolometer for double beta decay: Light and heat anticorrelation, light yield and quenching factors,* Astroparticle Physics **34**, 143 (2010).

[85] T. Yanagida, A. Yoshikawa, T. Itoh, M. Kawaharada, and F. Saito, *Temperature dependence α/β-ratio of GSO(Ce) scintillator,* in *2007 IEEE Nuclear Science Symposium Conference Record,* Vol. 2 (2007) pp. 1347–1350.

[86] C. Arnaboldi, S. Capelli, O. Cremonesi, L. Gironi, M. Pavan, G. Pessina, and S. Pirro, *Characterization of ZnSe scintillating bolometers for double beta decay,* Astroparticle Physics **34**, 344 (2011).

[87] A. Kudin, E. Sysoeva, E. Sysoeva, L. Trefilova, and D. Zosim, *Factors which define the α/γ ratio in CsI:Tl crystals,* Nuclear Instruments and Methods in Physics Research, Section A: Accelerators, Spectrometers, Detectors and Associated Equipment **537**, 105 (2005), cited By 0.

[88] J. Czirr, *The α/β ratio of several organic scintillators,* Nuclear Instruments and Methods **25**, 106 (1963).

[89] N. Galunov and E. Martynenko, *Ionizing radiation energy exchange in the regions of high activation density of organic scintillators,* Radiation Measurements **42**, 715 (2007), proceedings of the 6th European Conference on Luminescent Detectors and Transformers of Ionizing Radiation (LUMDETR 2006).

[90] G. Hull, N. P. Zaitseva, N. J. Cherepy, J. R. Newby, W. Stoeffl, and S. A. Payne, *New organic crystals for pulse shape discrimination,* IEEE Transactions on Nuclear Science **56**, 899 (2009).

[91] V. Álvarez, F. I. G. Borges, S. Cárcel, S. Cebrián, A. Cervera, C. A. N. Conde, T. Dafni, J. Díaz, M. Egorov, R. Esteve, P. Evtoukhovitch, L. M. P. Fernandes, P. Ferrario, A. L. Ferreira, E. D. C. Freitas, V. M. Gehman, A. Gil, A. Goldschmidt, H. Gómez, J. J. Gómez-Cadenas, D. González-Díaz, R. M. Gutiérrez, J. Hauptman, J. A. H. Morata,

D. C. Herrera, I. G. Irastorza, M. A. Jinete, L. Labarga, A. Laing, I. Liubarsky, J. A. M. Lopes, D. Lorca, M. Losada, G. Luzón, A. Marí, J. Martín-Albo, T. Miller, A. Moiseenko, F. Monrabal, C. M. B. Monteiro, F. J. Mora, L. M. Moutinho, J. M. Vidal, H. N. da Luz, G. Navarro, M. Nebot-Guinot, D. Nygren, C. A. B. Oliveira, R. Palma, J. Pérez, J. L. P. Aparicio, J. Renner, L. Ripoll, A. Rodríguez, J. Rodríguez, F. P. Santos, J. M. F. dos Santos, L. Seguí, L. Serra, D. Shuman, A. Simón, C. Sofka, M. Sorel, J. F. Toledo, A. Tomás, J. Torrent, Z. Tsamalaidze, D. Vázquez, J. F. C. A. Veloso, R. Webb, J. T. White, and N. Yahlali, *Ionization and scintillation response of high-pressure xenon gas to alpha particles,* Journal of Instrumentation **8**, P05025 (2013).

[92] M. Tanaka, T. Doke, A. Hitachi, T. Kato, J. Kikuchi, K. Masuda, T. Murakami, F. Nishikido, H. Okada, K. Ozaki, E. Shibamura, and E. Yoshihira, *LET dependence of scintillation yields in liquid xenon,* Nuclear Instruments and Methods in Physics Research Section A: Accelerators, Spectrometers, Detectors and Associated Equipment **457**, 454 (2001).

[93] P. Peiffer, T. Pollmann, S. Schönert, A. Smolnikov, and S. Vasiliev, *Pulse shape analysis of scintillation signals from pure and xenon-doped liquid argon for radioactive background identification,* Journal of Instrumentation **3**, P08007 (2008).

[94] P. H. Heckmann, *Richtungsabhängigkeit der szintillations-lichtausbeute von anthrazen beim beschüß mit α-strahlen,* Zeitschrift für Physik **157**, 139 (1959).

[95] F. Danevich, V. Kobychev, S. Nagorny, D. Poda, V. Tretyak, S. Yurchenko, and Y. Zdesenko, *$ZnWO_4$ crystals as detectors for decay and dark matter experiments,* Nuclear Instruments and Methods in Physics Research Section A: Accelerators, Spectrometers, Detectors and Associated Equipment **544**, 553 (2005).

[96] L. Bardelli, M. Bini, P. Bizzeti, F. Danevich, T. Fazzini, N. Krutyak, V. Kobychev, P. Maurenzig, V. Mokina, S. Nagorny, M. Pashkovskii, D. Poda, V. Tretyak, and S. Yurchenko, *Pulse-shape discrimination with $PbWO_4$ crystal scintillators,* Nuclear Instruments and Methods in Physics Research Section A: Accelerators, Spectrometers, Detectors and Associated Equipment **584**, 129 (2008).

[97] K. Yang, P. R. Menge, and V. Ouspenski, *Enhanced α - γ discrimination in co-doped $LaBr_3$:Ce,* IEEE Transactions on Nuclear Science **63**, 416 (2016).

[98] S. Rawat, M. Tyagi, P. Netrakanti, V. Kashyap, A. Singh, D. Desai, A. Mitra, G. A. Kumar, and S. Gadkari, *Pulse shape discrimination properties of $Gd_3Ga_3Al_2O_{12}$:Ce,B single crystal in comparison with CsI:Tl,* Nuclear Instruments and Methods in Physics Research Section A: Accelerators, Spectrometers, Detectors and Associated Equipment , (2016).

[99] Y. T. Vydai, V. A. Tarasov, A. M. Kudin, L. A. Andryushchenko, A. A. Ananenko, I. V. Kilimchuk, A. Y. Boyarintsev, and A. V. Klimov, *Stability of spectrometric characteristics of CsI:Tl detectors depending on the surface treatment method,* Instruments and Experimental Techniques **49**, 314 (2006).

3

SHAPE OF INTRINSIC ALPHA PULSE HEIGHT SPECTRA IN LANTHANIDE HALIDE SCINTILLATORS

Everyone has their own Everest to climb

Wanda Rutkiewicz

Internal contamination with actinium-227 and its daughters is a serious drawback in low-background applications of lanthanide-based scintillators. In this work we showed the important role of nuclear γ de-excitations on the shape of the internal alpha spectrum measured in scintillators. We calculated with Bateman equations the activities of contamination isotopes and the time evolution of actinium-227 and its progenies. Next, we measured the intrinsic background spectra of $LaBr_3$*(Ce),* $LaBr_3$*(Ce,Sr) and* $CeBr_3$ *with a digital spectroscopy technique, and we analyzed them with a pulse shape discrimination method (PSD) and a time-amplitude analysis. Finally, we simulated the* α *background spectrum with Geant4 tool-kit, consequently taking into account complex* α*-*γ*-electron events, the* α/β *ratio dependence on the* α *energy, and the electron/*γ *nonproportionality.*

We found that α*-*γ *mixed events have higher light yield than expected for alpha particles alone, which leads to overestimation of the* α/β *ratio when it is measured with internal* ^{227}*Th and* ^{223}*Ra isotopes. The time-amplitude analysis showed that the* α *peaks of* ^{219}*Rn and* ^{215}*Po in* $LaBr_3$*(Ce) and* $LaBr_3$*(Ce,Sr) are not symmetric. We compared the simulation results with the measured data and provided further evidence of the important role*

This chapter is adapted from: **W. Wolszczak** and P. Dorenbos, *Shape of intrinsic alpha pulse height spectra in lanthanide halide scintillators*, Nuclear Inst. and Methods in Physics Research, A, `http://dx.doi.org/10.1016/j.nima.2017.02.041`

of mixed α-γ-electron events for understanding the shape of the internal α spectrum in scintillators.

3.1. INTRODUCTION

Internal radioactive contamination is a serious drawback of lanthanide-based scintillators in low background applications. It reduces detector sensitivity [1], interferes with neutron measurements [2, 3] and complicates data analysis. A high internal background limits the usability of modern lanthanide-based scintillators when high radio-purity is important, for example in dark matter searches [4], gamma measurements in space exploration missions [5], detection of rare events [6, 7], and construction of high-sensitivity gamma detectors.

Intrinsic contamination with α and β-decaying isotopes has been found in many lanthanide-based scintillators, for example $LaBr_3$:Ce, $LaCl_3$:Ce [8–10], $CeBr_3$ [1], and $Cs_2LiLaBr_6$:Ce (CLLB) [3]. The sources of the contamination are naturally occurring radioactive isotopes: ^{138}La, ^{227}Ac, and their daughters undergoing α and β^- decays. Natural lanthanum is composed of stable ^{139}La (99.91% abundance) and radioactive ^{138}La [11]. Since it is not possible to separate both isotopes by chemical methods, ^{138}La contamination is unavoidable in scintillators containing lanthanum. Moreover, natural actinium contains a radioactive ^{227}Ac isotope. Actinium and lanthanum have very similar chemical properties, so all lanthanide-based scintillators are subjected to ^{227}Ac isotope contamination. Using cerium instead of lanthanum in cerium bromide makes it possible to obtain much higher radio-purity of the final material [1], but $CeBr_3$ has a lower energy resolution compared to other lanthanide scintillators.

Much research has addressed these issues trying to understand the origin of an internal background, simulate it, and find a way to avoid it. Hartwell and Gehrke [12] reported the presence of alpha emitting nuclides in $LaCl_3$:Ce and identified the contamination as ^{227}Ac and its daughters. Milbrath et al. [13] characterized an alpha contamination in $LaCl_3$:Ce with coincidence measurements and provided further evidence of ^{227}Ac presence. Later, Quarati et al. [14] studied radioactive decays of ^{138}La in $LaBr_3$:Ce and measured the shape of the internal β spectrum. These data were used later by Camp et el. [15] to successfully simulate an internal β and gamma spectrum from ^{138}La with PENELOPE/penEasy Monte Carlo code. Quarati et al. [1] also studied an alpha contamination in $CeBr_3$ and $LaBr_3$:Ce.

Despite these efforts, the shape of the internal alpha spectrum in lanthanide-based scintillators is still not fully understood. An attempt to simulate an internal alpha spectrum was not completely successful in $LaBr_3$:Ce [16], while recently Mesick et al. [2] simulated an alpha spectrum very accurately in CLLB. If an alpha activity in both scintillators is caused by the same ^{227}Ac contamination, then why does an alpha spectrum shape depend on a host material (compare [1, 3, 13])?

The aim of this study is to provide a deeper understanding of an internal α spectrum in the following lanthanide-based scintillators: $CeBr_3$, $LaBr_3$:Ce and $LaBr_3$:Ce,Sr (5% of Ce, 500 ppm of Sr). In Section 3.2 of this article, we discuss the origin of an intrinsic contamination in lanthanide-based scintillators in order to clarify which isotopes and alpha decays are expected in an internal background spectrum. Next, by analyzing the experimental data of Milbrath et. al [13] we show the influence of nuclear de-excitations on positions of internal alpha peaks. In Section 3.4, we calculate the time evolution of ^{227}Ac and its daughters with Bateman equations, which provides an understanding of the relative intensities of alpha peaks. Then, we present measurements of the background spectrum of the three mentioned materials performed with modern digital techniques. The results prove the usefulness of pulse shape discrimination (PSD) for separating α from γ events, and a time-amplitude analysis for selecting ^{219}Rn and ^{215}Po decays from a total α spectrum. Our results explain why the previous attempt to simulate an α spectrum in LaBr$_3$:Ce [16] was not successful. Finally, we compare our experimental results with a GEAN4 simulation to verify the role of nuclear gamma de-excitations in shaping an internal alpha spectrum.

3.2. ORIGIN OF INTRINSIC CONTAMINATION

The decay chain of ^{227}Ac is a sub-chain of the uranium 235 series (also called the "4n+3 chain"). The most probable path of ^{227}Ac decay goes through the following isotopes (see Fig. 3.1): $^{227}_{89}\mathrm{Ac} \rightarrow {}^{227}_{90}\mathrm{Th} \rightarrow {}^{223}_{88}\mathrm{Ra} \rightarrow {}^{219}_{86}\mathrm{Rn} \rightarrow {}^{215}_{84}\mathrm{Po} \rightarrow {}^{211}_{82}\mathrm{Pb} \rightarrow {}^{211}_{83}\mathrm{Bi} \rightarrow {}^{207}_{81}\mathrm{Tl} \rightarrow {}^{207}_{82}\mathrm{Pb}$ and ends on a stable lead-207. In this chain there are five α decays and three β^-. Since ^{227}Ac has the longest decay time, the rate of consequent decays is limited by that of actinium, and equal rate for all following daughter's decays may be expected (this will be discussed in detail in Section 3.4). On the other hand, in measurements of an intrinsic α particle background in ^{227}Ac contaminated crystals, we observe three broad bands, instead of five equal intensity α peaks. Shoulders or an additional low intensity peak are observed in some measurements, which makes an internal alpha spectrum difficult to analyze. Fig. 3.2 shows an exemplary spectrum of an intrinsic activity pulse height spectrum (PHS) measured in a commercial LaBr$_3$:Ce scintillator (BrilLance380™). A similar structure was reported for LaCl$_3$:Ce [10] and CeBr$_3$ [1]. On the right side of the picture we see a broad structure of three main peaks, ascribed to α particle detection, and a small satellite peak between the 2^{nd} and 3^{rd} main peaks. These peaks do not have the same intensity (height) as one would expect: the first and the second peak are equally intense, the satellite peak is two times less intense, and the third peak is the least intense.

3.3. COINCIDENCE MEASUREMENT ANALYSIS

Not only does the α energy spectrum have missing peaks, but identifying corresponding isotopes and α energies is also problematic.

Quarati et al. [1] analyzed the LaBr$_3$:Ce internal contamination spectrum and identified the peaks as follows: the first peak in the structure (see Fig. 3.2) as ^{223}Ra (E_α = 5716 keV), no peak from ^{227}Th, the second peak as ^{211}Bi (E_α = 6623 keV), the satellite peak as ^{219}Rn (E_α = 6819 keV), and the third peak as ^{215} Po (E_α=7386 keV). However, the values of the α/β ratio calculated with these energies are inconsistent (namely: 0.359, 0.343, 0.348, 0.359). The three last values increase with the energy, but the first one is exceptionally high. Recent research showed that the α/β ratio increases monotonically, approximately linear, with α energy in many scintillators at alpha energies higher than 2 MeV (a review on the α/β will be published separately [17]). This suggests that the identification of the first peak as ^{223}Ra needs to be reconsidered.

Hartwell et. al [9] identified the first peak as a mixed peak of ^{223}Ra and ^{227}Th, but in the analysis of the alpha response linearity they used the energy of ^{227}Th (~6 MeV), which resulted in a linear relation of the α/β ratio on the alpha energy. On the other hand, Negm et. al [16] have ascribed the first peak to ^{223}Ra E_α = 5716 keV, which again

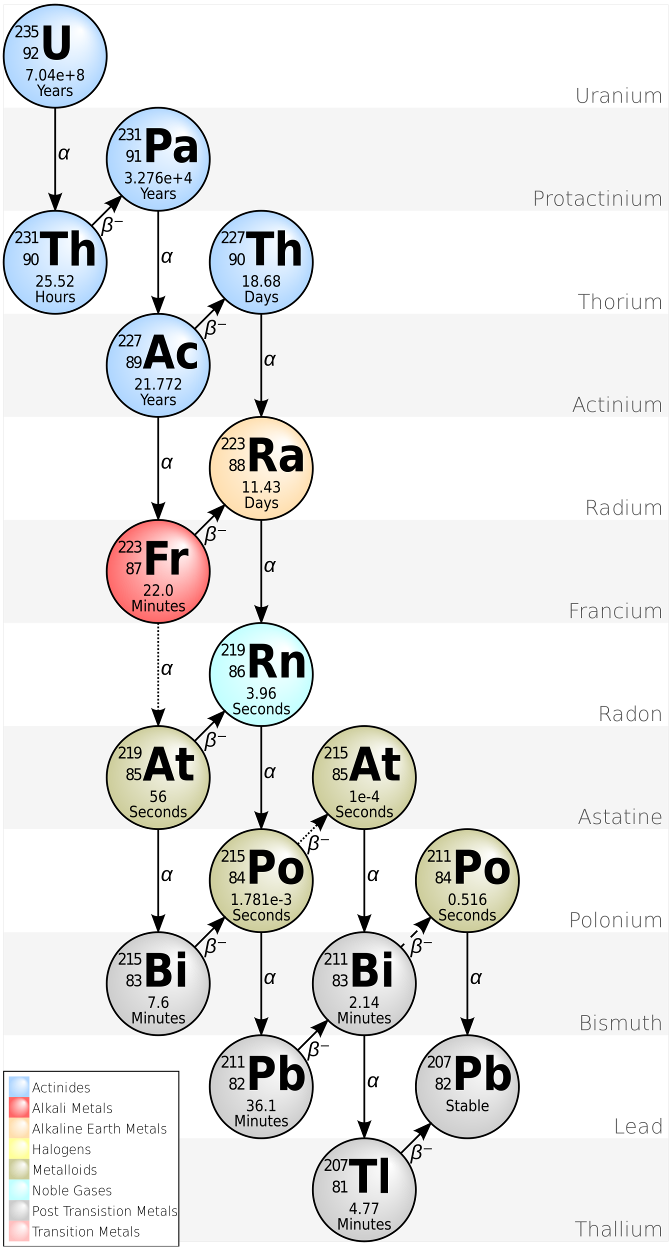

Figure 3.1: $^{235}_{92}$U decay chain: actinium series. Dashed arrow is a decay mode with <1% probability. Dotted arrows are decay modes with <0.01% probability. Graphics by Edgar Bonet used under CC BY-SA 3.0 license.

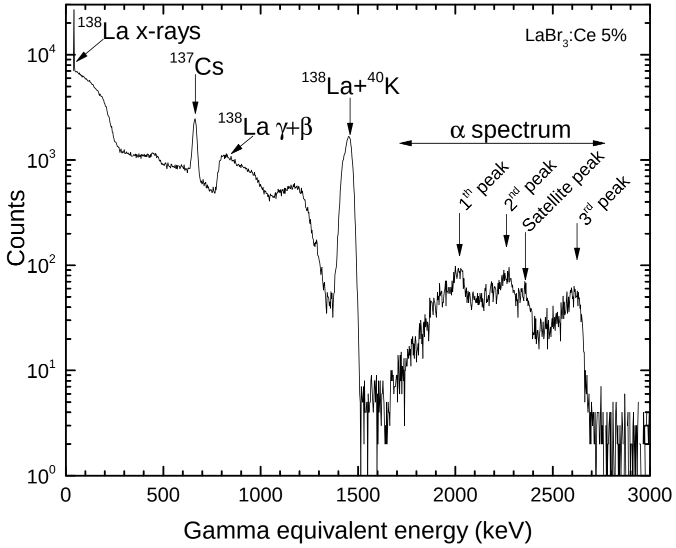

Figure 3.2: Exemplary intrinsic activity spectra of 1 inch $LaBr_3$:Ce (5 mol% of cerium). ^{137}Cs source was placed for energy reference.

resulted in a deviation from the linear relation between the α/β ratio and E_α.

To solve these inconsistencies we analyzed coincidence measurements done by Milbrath et al. for $LaCl_3$:Ce [8], but we found another complication for the α spectrum analysis. Milbrath et al. performed a measurement of the $LaCl_3$:Ce internal alpha spectrum in coincidence with gamma escapes detected by a High Purity Germanium (HPGe) detector. They looked for alpha decays followed by immediate gamma de-excitation and escape from the crystal. The same alpha particle energy was expected in coincidence with multiple γ energies, but in fact the measured alpha energies were also different. For instance, ^{227}Th decays with 5757 keV α emission and can be followed either by 236.0 keV, 256.3 keV or 286.1 keV γ (see Table 1 in [8]). Nevertheless, the α energies measured in coincidence were the following: 5831 keV, 5781 keV and 5727 keV. This means that for the same true α particle energy three different energies were actually measured. The difference exceeds the standard deviation which ranged from 44 to 65 keV. If one calculates the α/β ratio[1], the values for 5757 keV α energy are 0.324, 0.320 and 0.316, which is a non-physical result.

We can investigate this by taking a closer look at the simplified ^{227}Th decay scheme shown in Fig. 3.3. After the α decay with E_α = 5757 keV the daughter nucleus is in the excited state at 286.1 keV energy. It can de-excite by three different ways from this state:

- by emitting a single 286 keV γ photon,
- by emitting 256 keV and 50.1 keV γ photons, or

---

[1] α/β ratios were obtained by calculating measured α energies from Tab. 1 in [8] to γ-equivalent energy scale using equation $AlphaEnergy = (GammaEnergy) \times 2.2784 + 1578.6$ (in units of keV) and dividing by a true α particle energy.

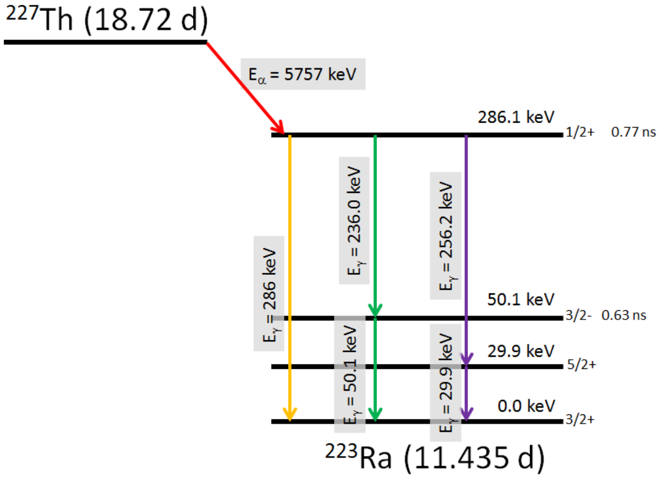

Figure 3.3: Simplified nuclear levels chart of ^{227}Th isotope decaying into ^{223}Ra by 5757 keV α emission. Other possible α decay modes, excited nuclear levels of ^{223}Ra and low intensity/forbidden γ transitions were excluded for clarity.

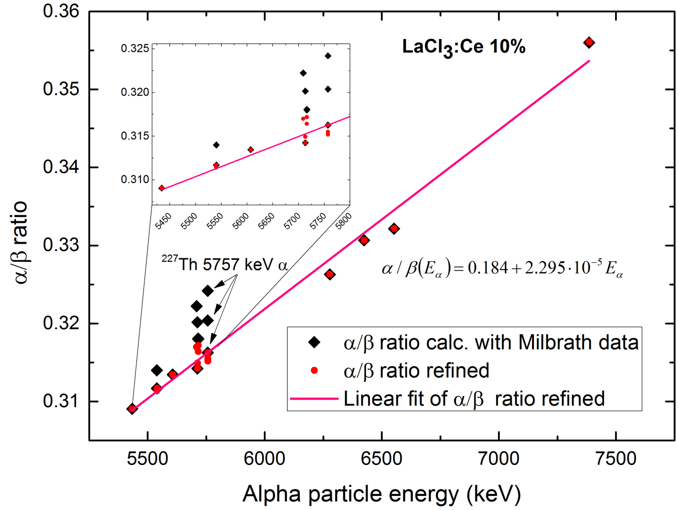

Figure 3.4: α/β ratio of LaCl$_3$:Ce 10 mol% calculated using Milbrath coincidence data [8] in function of true α particle energy (black diamonds) compared with α/β ratio calculated with subtracting γ photon energy left in scintillator (refined data, red circles). The inset shows energy range of ^{227}Th and ^{223}Ra isotopes for which multiple coincidences for the same true α energy were observed.

- by emitting 226 keV and 29.8 keV γ photons.

The lifetime of the ^{227}Th excited nuclear state is very short (shorter than 1 ns), so the gamma particle will be absorbed in a crystal and measured together with the alpha particle as a single event (shaping time used for collecting the scintillator signal is usually much longer than hundreds of ns). In case of 236 keV γ escape there is a high probability that a 50.1 keV gamma will be absorbed in a crystal and recorded together with the 5757 keV α. Because a γ photon has much higher light yield (per MeV) than an α particle, a significant amount of light will be added to an alpha event.

If one removes the energy of the second photon from an alpha event, then the α/β curve significantly improves when compared to the raw data. Fig. 3.4 shows the α/β ratio of $LaCl_3$:Ce calculated with raw Milbrath data [13] and the α/β ratio refined by subtracting the gamma energy. Deviation of the α/β ratio curve from linearity significantly decreases when the scintillation light added by gamma de-excitations is subtracted.

From the above analysis we can conclude that alpha decays followed by gamma nuclear de-excitations will be measured with a scintillator at higher energies than that of the alpha particle alone. Such an effect is not observed with typical α particle detectors (e.g., silicon surface barrier detectors), because they are not sensitive to gamma photons, and they measure an alpha particle energy alone. To understand the shape of an internal contamination α spectrum we need to take into account all electromagnetic processes following a nuclear decay: γ de-excitations, Compton effect, Auger electron emission, and X-ray fluorescence.

3.4. TIME EVOLUTION OF ^{227}AC CONTAMINATION

To investigate alpha peak intensities in an internal contamination spectrum, we first analyzed the time evolution of concentrations and activities of the ^{227}Ac isotope and its daughters. The differential equations governing successive radioactive decays can be written as

$$\begin{aligned}
\frac{dN_1(t)}{dt} &= -\lambda_1 N_1(t),\\
\frac{dN_2(t)}{dt} &= -\lambda_2 N_2(t) + \lambda_{1,2} N_1(t),\\
&\cdots\\
\frac{dN_n(t)}{dt} &= -\lambda_n N_n(t) + \lambda_{n-1,n} N_{n-1}(t),
\end{aligned} \tag{3.1}$$

where $N_i(t)$ is a number of atoms of a radioisotope i at a time t, λ_n is a total removal decay constant (including all decay branches), $\lambda_{i-1,i}$ is a partial decay constant (related to single decay branch from isotope $i-1$ to i) calculated from a branching ratio $\lambda_{i-1,i} = b_{i-1,i} \cdot \lambda_{i-1}$. The solution of this set of equations was first proposed by Bateman [18] for the case without a decay chain branching. The general problem solution, with included decay chain branching, was proposed by Skrable [19] as follows:

$$N_i(t) = N_1(0) \prod_{j=1}^{i-1} \lambda_{j,j+1} \times \sum_{j=1}^{i} \frac{e^{-\lambda_j t}}{\prod_{\substack{p=1\\ p\neq j}}^{i} (\lambda_p - \lambda_j)}. \tag{3.2}$$

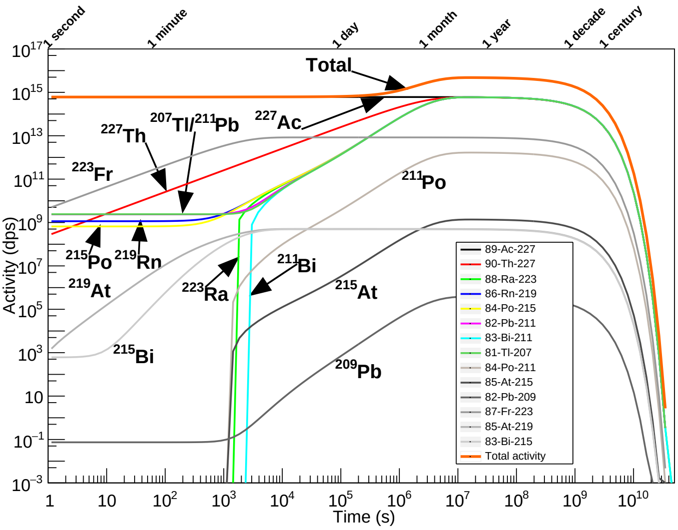

Figure 3.5: Evolution of activities of ^{227}Ac isotope and it's daughters starting from 1 mol of pure ^{227}Ac. Activities are expressed in decays per second (dps), including all possible decay branches of a particular isotope. Orange line shows the sum off all decay rates in the sample.

To calculate the solutions, we used TGeo package from the ROOT framework [20]. The calculations were performed assuming one mole of pure ^{227}Ac at the beginning, evaluated during 10^{11} seconds. There are 16 isotopes involved in the entire ^{227}Ac decay chain, which starts with ^{227}Ac and ends on stable $^{207}_{82}$Pb, accompanied by a small amount ($\sim 10^{14}$ atoms) of stable $^{209}_{83}$Bi produced through a cluster decay: $^{223}_{88}\mathrm{Ra} \rightarrow {}^{209}_{83}\mathrm{Bi} + {}^{14}_{6}\mathrm{C}$.

Equation (3.2) provides a solution for the number of atoms as a function of time. Since the number of atoms is not easily measurable, we are rather interested in activities. In Fig. 3.5 we show the calculated decay rates of the isotopes, according to the formula $A_i = N_i \lambda_i$, where λ_i is a decay constant of isotope i. Activities are expressed in the number of disintegrations per second, so they include all possible decay channels of a particular isotope. From this plot one can see that the total activity $A_{total} = \sum A_i$ increases first, and after reaching an equilibrium stage at day 109 it decreases exponentially, being limited by the ^{227}Ac decay rate. The important fact is that ^{227}Ac, ^{227}Th, ^{223}Ra, ^{219}Rn, ^{215}Po, ^{211}Pb and ^{207}Tl all have the same decay rate after reaching the equilibrium state.

Fig. 3.5 shows the decay rates of the isotopes. However, we are interested in alpha decay rates specifically, since they correspond to the intensities of the alpha peaks in the internal background spectrum. For instance, in case of the ^{227}Ac alpha decay, the branching ratio α-BR(^{227}Ac) = 1.38 % is very low. Consequently, the ^{227}Ac alpha peak intensity is almost a hundred times lower than the alpha peaks of ^{227}Th or ^{223}Ra, even though all three have the same decay rate. The amount of the initial contamination of ^{227}Ac is usually unknown, so from a practical point of view a ratio of an alpha decay rate to the total alpha activity is more useful than just an absolute activity. Fig. 3.6 shows the ratio of alpha isotopes decay activity A_i (multiplied by the α branching ratio) to the total

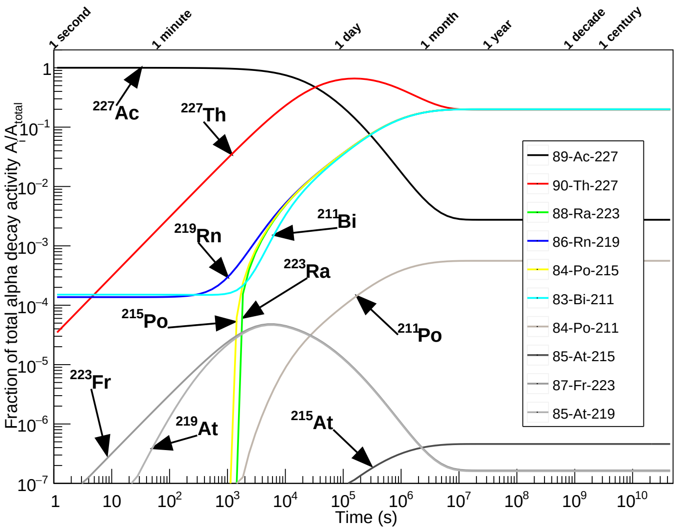

Figure 3.6: Time evolution of fractions of total alpha activity of ^{227}Ac isotope and it's daughters starting from 1 mol of pure ^{227}Ac.

activity A_{total} of all alpha decaying isotopes. During the first 8 hours, the alpha decays are dominated by decays of ^{227}Ac, then alpha activity from ^{227}Th increases. Finally, after 109 days the decays of ^{227}Th, ^{223}Ra, ^{219}Rn, ^{211}Bi and ^{215}Po reach equal decay rates, while the activity of ^{227}Ac decreases and becomes more than two orders of magnitude lower then others. The alpha activities of ^{211}Po, ^{215}At, ^{223}Fr and ^{219}At isotopes are many order of magnitude lower, so these isotopes are extremely difficult to detect on a statistically significant level.

The main conclusion is that after 109 days the decaying isotopes are in equilibrium and activities of alpha decays of ^{227}Th, ^{223}Ra, ^{219}Rn, ^{211}Bi, and ^{215}Po are equal. Very low activity from ^{227}Ac alpha decays may be also detected, and in fact a weak ^{227}Ac alpha peak was reported by Hartwell et al. [9].

3.5. MATERIALS AND METHODS

3.5.1. SAMPLES AND EXPERIMENTAL SETUP

The intrinsic activities of the following three samples were measured: a 3 by 3 inch cylinder of $LaBr_3$:Ce (5 mol% of Ce), a 2 by 2 inch cylinder of $CeBr_3$ and a bare sample of approximately 10 mm x 5 mm x 20 mm $LaBr_3$:Ce,Sr (5 mol% of Ce, <0.5 mol% of Sr). The first two samples were encapsulated by the manufacturer, Saint Gobain Corporation, and the third sample was encapsulated in our lab into a hermetic can with a quartz window.

Fig. 3.7 shows the schematic of the experimental setup. A measured sample was coupled with an optical grease to an XP4312 photomultiplier tube (PMT) and placed inside a light-proof casing. A laser diode was mounted in the casing pointing to the photocatode of the PMT. The laser light pulses were used in the later data analysis for a

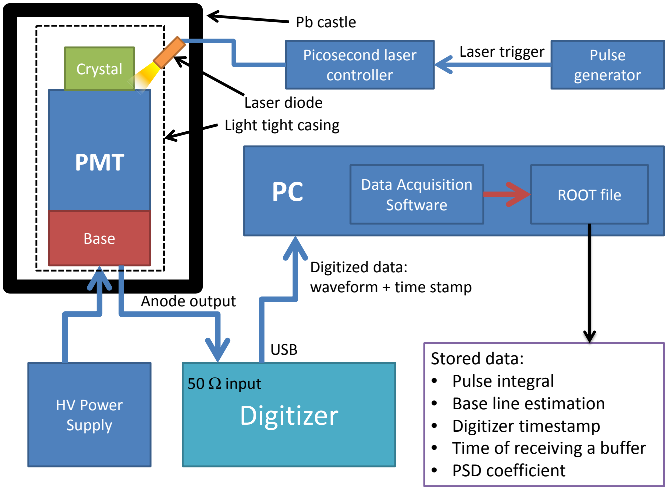

Figure 3.7: Schematic of the digital nuclear spectroscopy setup.

gain correction. The casing was put in a 15 cm thick lead castle in order to reduce natural background in the measurement. The raw signal from the 50 Ω terminated anode was directly connected to the 50 Ω input of a CAEN Digitizer model 5730.

3.5.2. DATA ACQUISITION AND ANALYSIS

The digitizer generates an internal trigger when an input signal exceeds the threshold voltage V_{th}. The input signal is sampled with 14-bit precision and 500 Mega Samples per Second (MSPS) sampling rate and stored in a buffer. Each stored waveform has 1280 samples (2560 ns) and is attached with a 32 bit counter of the Trigger Time Tag (TTT). The time resolution of TTT is 12 ns.

Home made data acquisition software (DAQ) was developed for controlling data acquisition, data transfer to a PC, performing an initial analysis, and storing the results in ROOT data file format [20]. Since the TTT counter overflows after around 17 s, every buffer received from the digitizer was attached by the DAQ with a local PC Time Tag (PTT). The PTT was used in a later analysis for time ranges exceeding the TTT counter size.

Fig. 3.8 shows the steps of the data analysis. The three first steps are calculated for every event during a data acquisition: a base line V_{BL}, a pulse integral Q_{total}, and a pulse shape discrimination (PSD) factor V_p/Q_{total}. The base line V_{BL} is calculated as an arithmetic average of the first 340 samples, when a scintillation pulse is not yet present. The pulse integral is calculated by subtracting the base line V_{BL} from the waveform and summing values of 150 samples (300 ns) starting from the end of the base line calculation window. The integration time of 300 ns is sufficient for the fast cerium scintillators studied in this work. For Pulse Shape Discrimination (PSD), a PSD factor V_p/Q_{total} as described by Ogawara et al. [21] was calculated as a ratio of a raw pulse maximum amplitude V_p to integrated charge Q_{total}.

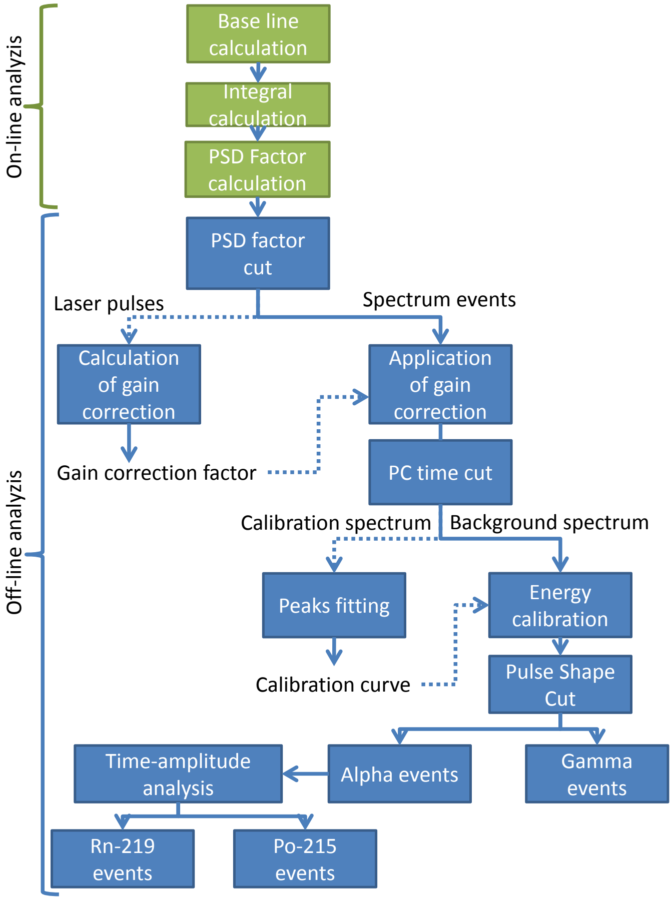

Figure 3.8: Steps of the data analysis.

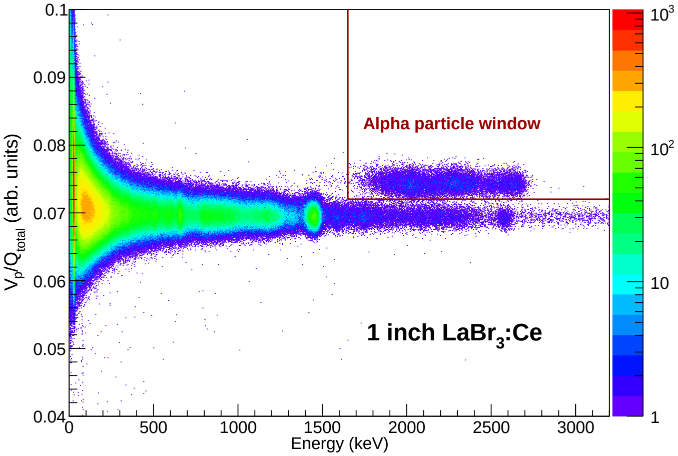

Figure 3.9: Pulse shape discrimination parameter V_p/Q_{total} in function of γ-equivalent energy measured with ϕ1 inch × 1 inch LaBr$_3$:Ce crystal, exposed to ambient radiation. Color represents the number of counts. Internal alpha decays are easily distinguishable from a gamma background.

Fig. 3.9 shows an exemplary plot of a PSD factor versus a gamma equivalent energy measured with a 1 inch LaBr$_3$:Ce sample exposed to ambient radiation. The band centered around $V_p/Q_{total} \approx 0.07$ displayed across all energies and widening toward lower energy comes from gamma/electron events, while a small band in the energy range 1.7 - 2.7 MeV, with slightly higher V_p/Q_{total}, is caused by alpha particle events. One may notice a gamma peak from ^{40}K/^{138}La events around 1.5 MeV and a weak gamma peak from ^{208}Tl around 2.6 MeV. An alpha particle window was accordingly adjusted for selection of alpha events in different samples. The example plot shows the importance of usage of PSD in this case, since the ^{208}Tl γ-peak overlaps with the alpha spectrum and without that technique it is difficult to distinguish gamma decays from ^{208}Tl and alpha decays from ^{215}Po.

3.5.3. TIME-AMPLITUDE ANALYSIS

We used features of the ^{226}Ac decay chain in the off-line analyses to select only a specific sequence of events in an energy-time space. Since ^{219}Rn decays into ^{215}Po with decay time of around 4 seconds, and ^{215}Po decays to ^{211}Pb with decay time around 1.8 ms (see Fig. 3.1), in off-line analysis we selected pairs of alpha decays falling within the 20 ms coincidence window. Additionally, we added energy criteria by requiring that the first event has the energy of a ^{219}Rn alpha decay, and the second that of a ^{215}Po decay: ^{219}Rn ($T_{1/2} = 3.98$ s, $Q_\alpha = 6946$ keV)$\rightarrow$^{215}Po ($T_{1/2} = 1.781$ ms, $Q_\alpha = 7526$ keV). This eliminated most random events and filtered out only Rn-Po event pairs.

3.5.4. SIMULATION

In order to verify the importance of the gamma de-excitations we simulated the internal alpha spectrum in $LaBr_3$:Ce,Sr with the Geant4 toolkit and home made analysis software. Decays of ^{223}Ra, ^{227}Th, ^{211}Bi, ^{219}Rn, ^{215}Po in equal amounts were simulated including α decays, internal conversion and Auger de-excitations. The observed energy E'_m in particular event m was calculated by including the α/β ratio of the α particle, and the gamma Y_γ and an electron nonproportionality Y_e, according to the following formula:

$$E'_m = E_\alpha \cdot \alpha/\beta(E_\alpha) + \sum_{i=1}^{n_e} E_e \cdot Y_e(E_e) + \sum_{i=1}^{n_\gamma} E_\gamma \cdot Y_\gamma(E_\gamma). \tag{3.3}$$

E_α, E_e, E_γ are true energies of the α, electrons and gammas in m event; summing goes over all electrons n_e and gammas n_γ in the event. We used electron nonproportionality data Y_e and gamma non proportionality Y_γ from [22].

We did not find appropriate data on the α/β ratio as a function of alpha energy, so we used a linear model as approximation (see also Fig. 3.4)

$$\alpha/\beta(E_\alpha) = a + b \cdot E_\alpha, \tag{3.4}$$

where a and b are free parameters fitted to the experimental data. Comprehensive justification of the linear approximation will be presented in a separate article on the α/β ratio [17].

The energy resolution was simulated by convoluting the generated spectrum with an energy resolution model $R(E') = A\sqrt{E'}$, where A is a free parameter and E' is an observed (quenched) energy.

3.6. RESULTS

3.6.1. MEASUREMENT

Fig. 3.10, 3.11 and 3.12 show the internal background spectra of the measured samples: $LaBr_3$:Ce, $CeBr_3$ and $LaBr_3$:Ce,Sr respectively. The main feature for all three samples is a peak located around 1450 keV which originates from potassium ^{40}K gamma decays and/or ^{138}La decay daughter de-excitation in the case of $LaBr_3$. In $LaBr_3$:Ce and $LaBr_3$:Ce,Sr this peak appears at a lower channel number than the measured alpha spectrum, but in the case of $CeBr_3$:Ce it overlaps with it. Hence, a suppression of the potassium presence or PSD becomes crucial for measuring a pure alpha spectrum in $CeBr_3$.

Alpha events were separated from electron/gamma events by using PSD (see Fig. 3.9). Peaks originating from ^{219}Rn and ^{215}Po alpha decays were separated from the rest of the alpha decays with time-amplitude analysis. In Fig. 3.10, 3.11 and 3.12 alpha particle spectra with separated peaks are shown for $LaBr_3$:Ce, $CeBr_3$:Ce and $LaBr_3$:Ce,Sr samples. The main difference between the samples is the position of the alpha spectrum on a gamma calibrated energy scale. Since the true energies of alpha decaying isotopes are the same, it means that the alpha particle light yield quenching is significantly different in these materials. The quenching is the lowest in $LaBr_3$:Ce,Sr and the highest in $CeBr_3$:Ce.

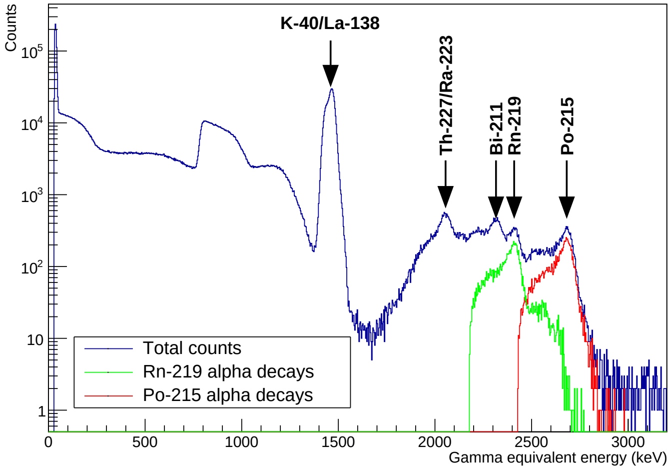

Figure 3.10: Intrinsic activity energy spectrum (dark blue) measured with 3 inch LaBr$_3$:Ce (5 mol% of Ce) crystal together with Radon-219 (green) and Polonium-215 (red) peaks separated using amplitude-time analysis (colour online).

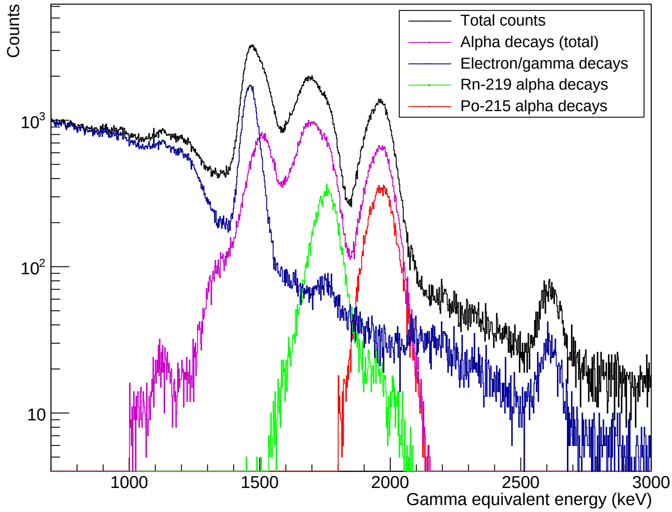

Figure 3.11: Intrinsic activity energy spectrum measured with 2 inch CeBr$_3$ crystal. Alpha (magenta) and gamma events (dark blue) were separated with PSD, then Radon-219 (green) and Polonium-215 (red) peaks were separated using time-amplitude analysis (colour online).

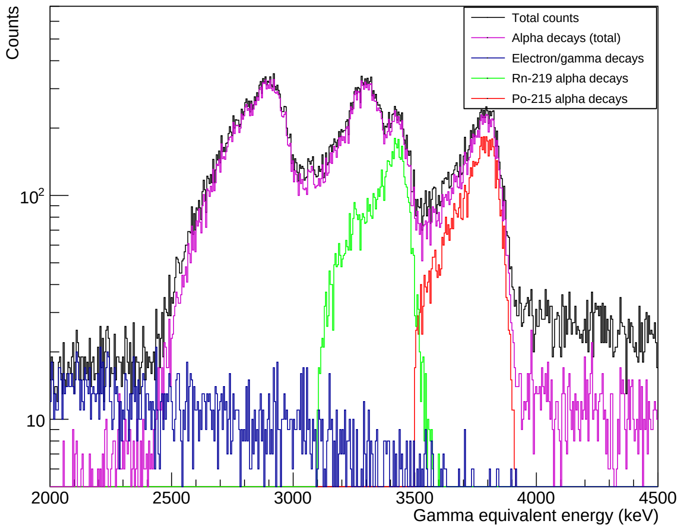

Figure 3.12: Internal background spectrum of LaBr$_3$:Ce,Sr sample with alpha and electron/gamma events separated (colour online). Alpha peaks from ^{215}Po and ^{219}Rn were separated from total alpha decays spectrum with time-amplitude method. Gamma/electron background is clean from any peaks at energy range where alpha particles are observed (2400-4000 keV). From the alpha discriminated spectrum, it is clear that alpha peaks are asymmetric.

Note that an asymmetric shape of the alpha peaks is observed for LaBr$_3$:Ce (Fig. 3.10) and LaBr$_3$:Ce,Sr (Fig. 3.12), but not for CeBr$_3$ (Fig. 3.11). Fig. 3.13 shows the alpha peaks from ^{219}Rn and ^{215}Po isotopes in LaBr$_3$:Ce,Sr with a double-Gaussian fit used as a model. This model is used for mathematical simplicity, without physical justification. Consequently, the energy resolutions shown in Fig. 3.13 should not be treated as precise and quantitative.

Table 3.1 lists the α/β ratio measured with an internal alpha activity and analyzed with the time-amplitude analyses. In case of asymmetric alpha peaks in LaBr$_3$:Ce and LaBr$_3$:Ce,Sr the highest intensity peak was used for calculating the α/β ratio. As one can notice, the α/β ratio increases from CeBr$_3$, LaBr$_3$:Ce up to LaBr$_3$:Ce,Sr. Furthermore, the α/β ratio increases with the true alpha energy for all studied materials.

3.6.2. SIMULATION

Fig. 3.14 compares the simulation (red curve) and the measurement (black curve) of the internal alpha background in LaBr$_3$:Ce,Sr. Separate energy spectra of the constituent isotopes are shown below the red curve, while the energies without including an energy resolution are shown as vertical lines. One may notice that ^{215}Po has a single vertical line corresponding to an α decay directly to the ground state of the daughter nucleus. The simulation successfully reproduces the main feature of the internal activity spectrum: the three band structure. However, a low energy tail is present for every band in the measured spectrum. It is especially visible for Ra/Th peak, which is followed by a long tail on the left side. As a consequence it has a lower intensity than expected from the

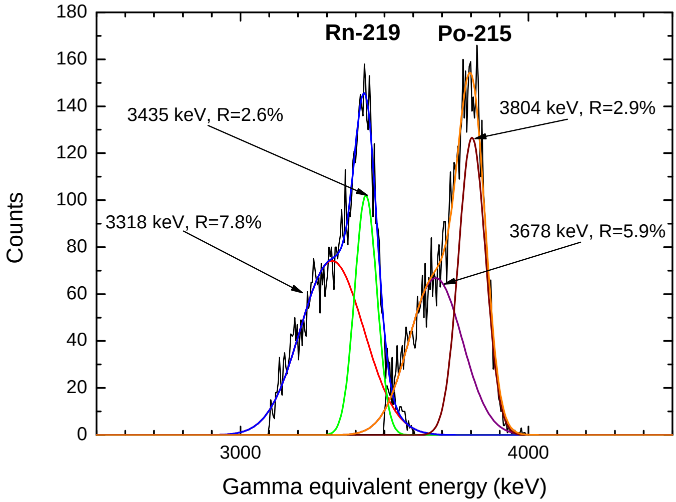

Figure 3.13: Rn-219 and Po-215 alpha peaks measured with internal contamination background in LaBr$_3$:Ce,Sr sample and separated from total background spectrum using pulse shape discrimination and time-amplitude analysis. Asymmetry of alpha peaks is clearly visible.

Table 3.1: α/β ratio measured in different materials using time-amplitude analysis to separate Po-215 and Rn-219 alpha peaks from α internal background.

Material	Isotope	True α energy (keV)	Measured γ equivalent (keV)	α/β ratio
LaBr$_3$:Ce,Sr	Po-215	7386.1	3804	0.515
LaBr$_3$:Ce,Sr	Rn-219	6819.2	3435	0.504
LaBr$_3$:Ce	Po-215	7386.1	2682	0.363
LaBr$_3$:Ce	Rn-219	6819.2	2410	0.353
CeBr$_3$	Po-215	7386.1	1966	0.266
CeBr$_3$	Rn-219	6819.2	1753	0.257

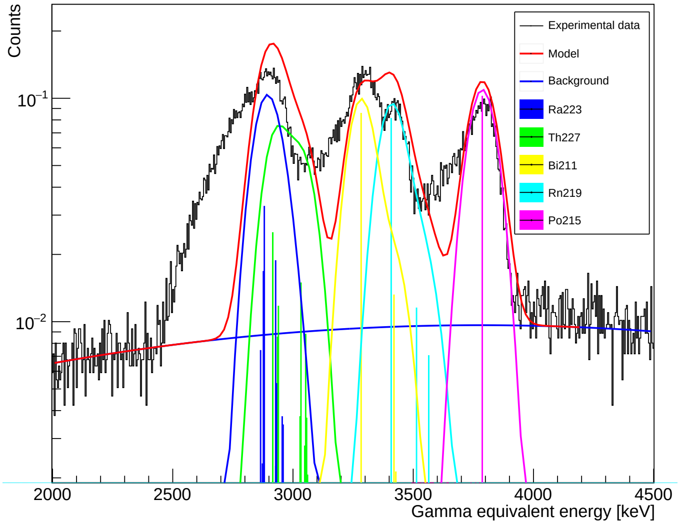

Figure 3.14: Comparison of simulation of internal alpha activity (red curve) of Ac-227 and the measured data (black curve) with LaBr$_3$:Ce,Sr (colour online). The simulation includes all de-excitation processes (X-ray fluorescence, Auger electrons emission) and assumes complete absorption of all γ photons.

simulation. Similarly the peak-to-valley ratio between ^{219}Rn and ^{215}Po is lower due to events coming from the tails. The disagreement is anticipated, since the asymmetric shape of alpha peaks was not included in the simulation. This provides further evidence that the asymmetric shape previously shown in Fig. 3.13 is crucial for understanding the spectrum shape.

Fig. 3.15 shows the simulation of the internal alpha spectrum excluding the contribution of gamma photons, assuming that all gamma photons escape from the crystal without being absorbed (the third term in Eq. 3.3 is abandoned). In this case, the Ra/Th peak is a double peak, which is not observed in the measurement. The spectrum simulated in this way is very different from the measured with CeBr$_3$ (Fig. 3.11) and LaBr$_3$:Ce (Fig. 3.10).

One may compare the ^{219}Rn peak in Fig. 3.14 and the same peak in Fig. 3.15. The low intensity lines of mixed α/γ events are on the right side of the highest intensity line in the simulation which included gamma de-excitations (Fig. 3.14). In the second case, when the gamma absorptions were excluded (all gamma photons escape), the low intensity lines are on the left (Fig. 3.15). This proves that a correct simulation of an internal background spectrum in scintillators is impossible without taking into account gamma interactions. In fact, the shape of a measured spectrum is somewhere in between a complete gamma absorption simulation and a complete escape, additionally smeared by Compton scattering.

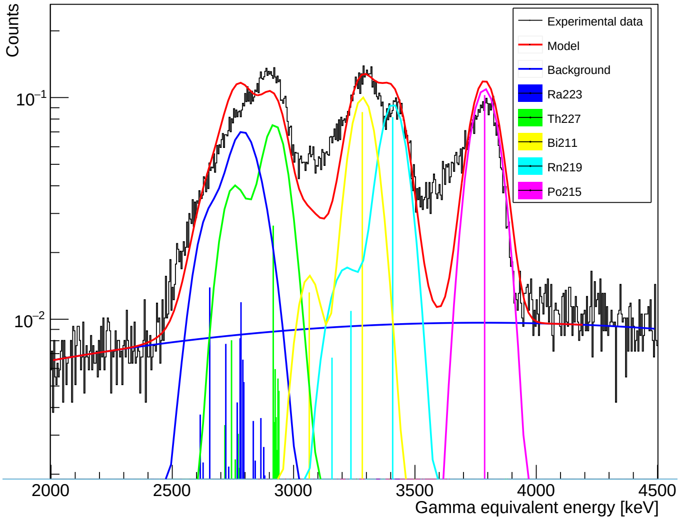

Figure 3.15: Comparison of Ac-227 alpha activity simulation (red curve) and the measured data (black curve) with $LaBr_3$:Ce,Sr (colour online). The simulation assumes no contribution from gamma photons (all photons escape from the crystal).

3.7. DISCUSSION

In case of lanthanum-based scintillators, we observe asymmetric alpha peaks (see Fig. 3.13 and 3.10). In contrast, in $CeBr_3$, alpha peaks are symmetric (compare Fig. 3.11). The asymmetric peaks with low energy tails are responsible for a low valley-to-peak ratio observed in an internal background spectrum of $LaBr_3$:Ce, $LaBr_3$:Ce,Sr, and probably in $LaCl_3$:Ce [13]. The origin of this phenomenon is unknown. We considered several hypotheses to explain the effect, and we concluded that the most probable is the presence of light yield non-uniformities in the crystal structure. These non-uniformities can exist on the length scale of the α particle track length ($\sim 25\ \mu$m) and are washed out with much longer β-tracks.

We excluded the role of X-ray or gamma escape in that process by analyzing coincidence measurements done by Milbrath [13]. From Fig. 3.13 one can see that energy difference between "main" peaks and "escape" peaks is around 100 keV, but such energies were not observed in a coincidence with ^{219}Rn and ^{215}Po peaks.

The simulation (Fig. 3.14) shows that ^{215}Po decays with emission of a single α energy, so it is not disturbed by gamma absorption. On the other hand, the ^{219}Rn alpha peak can be recorded with accompanying gamma de-excitations, which can be seen in Fig. 3.14 as a tail at the high energy side of the peak. The tail is caused by recording an α particle with de-excitation gamma photon. As gamma photons have higher light yield then alpha particles, the lines are seen on the right side from the main alpha peak. The reader may compare the simulated ^{219}Rn peak shape with the peaks measured with time-amplitude analysis in $LaBr_3$:Ce (Fig. 3.10) and $CeBr_3$ (Fig. 3.11).

In the simulation we assumed that all gamma photons are absorbed within the scintillator. This assumption is justified for big crystals, like 2 inch $CeBr_3$ (Fig. 3.10) and 3 inch $LaBr_3$:Ce (Fig. 3.11), but does not hold for the small sample of $LaBr_3$:Ce,Sr (Fig. 3.12). A high energy tail made of α-γ mixed events is visible in 3 inch $LaBr_3$:Ce and 2 inch $CeBr_3$, but it disappears in the small $LaBr_3$:Ce,Sr sample (Fig. 3.12).

3.8. CONCLUSIONS

Digital spectroscopy can be a powerful tool for studying scintillators, and it makes possible to perform a complex analysis like a pulse shape discrimination or a time-amplitude analysis. This permitted us to investigate the complex structure of an internal alpha spectrum in $LaBr_3$:Ce, $LaBr_3$:Ce,Sr and $CeBr_3$.

An alpha spectrum measured in a scintillator with an internal contamination can be significantly distorted by gamma de-excitations of decay products. This is because an alpha particle can be detected together with a gamma photon as a single event, but both particles have significantly different light yields. This conclusion is particularly important for everyone trying to simulate an internal alpha activity. In addition, measuring the α/β ratio with an internal alpha contamination seems to be an attractive way of avoiding surface effects, but it can not be easily done with an alpha isotope decaying into an excited state of a daughter nucleus.

By applying time-amplitude cuts on the acquired data, we were able to separate Po-215 and Rn-219 alpha peaks from the total spectrum. By this means, we found asymmetric alpha peaks in $LaBr_3$:Ce and $LaBr_3$:Ce,Sr but not in $CeBr_3$. The cause of this phenomenon is not known.

Our approach to include nuclear de-excitation processes in simulation is promising, and together with experimental data on asymmetric α peaks gives a way to construct a complete and accurate simulation of a scintillation response to an internal activity. We advise using the ^{215}Po alpha peak in future α/β ratio measurements, as this peak is made out of pure alpha decays to a ground state, not followed by any other type of de-excitation.

REFERENCES

[1] F. Quarati, P. Dorenbos, J. van der Biezen, A. Owens, M. Selle, L. Parthier, and P. Schotanus, *Scintillation and detection characteristics of high-sensitivity CeBr3 gamma-ray spectrometers,* Nuclear Instruments and Methods in Physics Research Section A: Accelerators, Spectrometers, Detectors and Associated Equipment **729**, 596 (2013).

[2] K. Mesick, D. Coupland, and L. Stonehill, *Pulse-shape discrimination and energy quenching of alpha particles in* $Cs_2LiLaBr_6$*:*Ce^{3+}, Nuclear Instruments and Methods in Physics Research Section A: Accelerators, Spectrometers, Detectors and Associated Equipment **841**, 139 (2017).

[3] R. S. Woolf, B. F. Phlips, and E. A. Wulf, *Characterization of the internal background for thermal and fast neutron detection with CLLB,* Nuclear Instruments and Methods in Physics Research Section A: Accelerators, Spectrometers, Detectors and Associated Equipment **838**, 147 (2016).

[4] R. Bernabei, P. Belli, A. Bussolotti, F. Cappella, R. Cerulli, C. Dai, A. d'Angelo, H. He, A. Incicchitti, H. Kuang, J. Ma, A. Mattei, F. Montecchia, F. Nozzoli, D. Prosperi, X. Sheng, and Z. Ye, *The DAMA/LIBRA apparatus,* Nuclear Instruments and Methods in Physics Research Section A: Accelerators, Spectrometers, Detectors and Associated Equipment **592**, 297 (2008).

[5] W. Drozdowski, P. Dorenbos, A. J. J. Bos, G. Bizarri, A. Owens, and F. G. A. Quarati, *$CeBr_3$ scintillator development for possible use in space missions,* IEEE Transactions on Nuclear Science **55**, 1391 (2008).

[6] F. Danevich, V. Kobychev, O. Ponkratenko, V. Tretyak, and Y. Zdesenko, *Quest for double beta decay of ^{160}Gd and Ce isotopes,* Nuclear Physics A **694**, 375 (2001).

[7] F. Danevich, V. Kobychev, S. Nagorny, and V. Tretyak, *YAG:Nd crystals as possible detector to search for and decay of neodymium,* Nuclear Instruments and Methods in Physics Research Section A: Accelerators, Spectrometers, Detectors and Associated Equipment **541**, 583 (2005).

[8] B. Milbrath, R. Runkle, T. Hossbach, W. Kaye, E. Lepel, B. McDonald, and L. Smith, *Characterization of alpha contamination in lanthanum trichloride scintillators using coincidence measurements,* Nuclear Instruments and Methods in Physics Research Section A: Accelerators, Spectrometers, Detectors and Associated Equipment **547**, 504 (2005).

[9] J. Hartwell and R. Gehrke, *Observations on the background spectra of four $LaCl_3$(Ce) scintillation detectors,* Applied Radiation and Isotopes **63**, 223 (2005).

[10] B. Milbrath, J. McIntyre, R. Runkle, and L. Smith, *Contamination studies of $LaCl_3$:Ce scintillators,* Nuclear Science, IEEE Transactions on **53**, 3031 (2006).

[11] J. Meija, T. B. Coplen, M. Berglund, W. A. Brand, P. De Bièvre, M. Gröning, N. E. Holden, J. Irrgeher, R. D. Loss, T. Walczyk, *et al., Isotopic compositions of the elements 2013 (IUPAC Technical Report),* Pure and Applied Chemistry **88**, 293 (2016).

[12] J. Hartwell and R. Gehrke, *Observations on the background spectra of four $LaCl_3$(Ce) scintillation detectors,* Applied Radiation and Isotopes **63**, 223 (2005).

[13] B. Milbrath, R. Runkle, T. Hossbach, W. Kaye, E. Lepel, B. McDonald, and L. Smith, *Characterization of alpha contamination in lanthanum trichloride scintillators using coincidence measurements,* Nuclear Instruments and Methods in Physics Research Section A: Accelerators, Spectrometers, Detectors and Associated Equipment **547**, 504 (2005).

[14] F. Quarati, I. Khodyuk, C. van Eijk, P. Quarati, and P. Dorenbos, *Study of ^{138}La radioactive decays using $LaBr_3$ scintillators,* Nuclear Instruments and Methods in Physics Research Section A: Accelerators, Spectrometers, Detectors and Associated Equipment **683**, 46 (2012).

[15] A. Camp, A. Vargas, and J. M. Fernández-Varea, *Determination of LaBr$_3$(Ce) internal background using a {HPGe} detector and monte carlo simulations,* Applied Radiation and Isotopes **109**, 512 (2016), proceedings of the 20th International Conference on Radionuclide Metrology and its Applications 8–11 June 2015, Vienna, Austria.

[16] H. Negm, M. Omer, H. Zen, I. Daito, T. Kii, K. Masuda, T. Hori, H. Ohgaki, R. Hajima, T. Hayakawa, T. Shizuma, N. Kikuzawa, and H. Toyokawa, *Monte carlo simulation of response function for LaBr$_3$(Ce) detector and its internal-activity,* in *Advancements in Nuclear Instrumentation Measurement Methods and their Applications (ANIMMA), 2013 3rd International Conference on* (2013) pp. 1–5.

[17] W. Wolszczak and P. Dorenbos, *Nonproportional response of scintillators to alpha particle excitation,* IEEE Transactions on Nuclear Science **64**, 1580 (2017).

[18] H. Bateman, *The solution of a system of differential equations occurring in the theory of radioactive transformations,* in *Proc. Cambridge Philos. Soc,* Vol. 15 (1910) pp. 423–427.

[19] K. Skrable, C. French, G. Chabot, and A. Major, *A general equation for the kinetics of linear first order phenomena and suggested applications.* Health physics **27**, 155 (1974).

[20] R. Brun and F. Rademakers, *ROOT — an object oriented data analysis framework,* Nuclear Instruments and Methods in Physics Research Section A: Accelerators, Spectrometers, Detectors and Associated Equipment **389**, 81 (1997), new Computing Techniques in Physics Research V.

[21] R. Ogawara and M. Ishikawa, *Feasibility study on signal separation for spontaneous alpha decay in LaBr$_3$:Ce scintillator by signal peak-to-charge discrimination,* Review of Scientific Instruments **86**, 085108 (2015), http://dx.doi.org/10.1063/1.4928115.

[22] M. S. Alekhin, D. A. Biner, K. W. Krämer, and P. Dorenbos, *Improvement of LaBr$_3$:5%Ce scintillation properties by Li$^+$, Na$^+$, Mg^{2+}, Ca^{2+}, Sr^{2+}, and Ba^{2+} co-doping,* Journal of Applied Physics **113**, 224904 (2013).

4

TIME-RESOLVED GAMMA SPECTROSCOPY OF SINGLE EVENTS

> *Nearly every understanding is gained by a painful struggle in which belief and unbelief are dramatically interwoven.*
>
> Leopold Infeld

In this article we present a method of characterizing scintillating materials by digitization of each individual scintillation pulse followed by digital signal processing. With this technique it is possible to measure the pulse shape and the energy of an absorbed gamma photon on an event-by-event basis. In contrast to time-correlated single photon counting technique, the digital approach provides a faster measurement, an active noise suppression, and enables characterization of scintillation pulses simultaneously in two domains: time and energy. We applied this method to study the pulse shape change of a CsI(Tl) scintillator with energy of gamma excitation. We confirmed previously published results and revealed new details of the phenomenon.

This chapter is adapted from: **W. Wolszczak** and P. Dorenbos, *Time-resolved gamma spectroscopy of single events*, Nuclear Inst. and Methods in Physics Research, A, 886 (2018) 30–35 `https://doi.org/10.1016/j.nima.2017.12.080`

4.1. INTRODUCTION

Despite many years of studies on scintillating materials many questions are still open. While luminescence processes and high energy radiation interactions with matter are well understood, the fundamental processes of energy transport and high density quenching are still puzzling [1–6]. It is well known that a scintillation pulse shape changes with change of type of excitation (γ-rays, neutrons, α particles, high energy ions) [7–13]. This phenomenon is commonly used for particle discrimination in variety of applications [14–17]. However, the origin and the exact mechanism are still not known. In last years, a dependence of a scintillation pulse shape on γ photons energy was reported for various materials [18–21]. Recent theoretical developments [2, 3, 5, 6] provided an explanation of these observations by modeling the charge separation inside the ionization track created during a gamma energy excitation.

Despite successful results of the theoretical modeling, many aspects still require an experimental study and verification. This raises a need for new data and a new experimental approach. The aim of this study is to provide a new method of characterizing scintillators in two domains simultaneously: in terms of the excitation energy, and time evolution of scintillation.

We will demonstrate that by digitization of individual scintillation pulses and digital signal processing it is possible to study the scintillation mechanism in terms of pulse shape and light yield at the same time. For each scintillation pulse it is possible to calculate the integral light output and corresponding deposited amount of energy. The acquired pulse height spectrum can be later subdivided into energy bins. An average scintillation pulse shape can be calculated for each energy bin by taking an average of all acquired events within that bin. However, to obtain undistorted pulse shapes additional signal processing and event selections are required before taking the average.

With this method we verified previous experimental results on CsI(Tl) pulse shape dependence on gamma energy, and we compared those results with theoretical models [6]. We have found that the pulse shape change predicted by the model is in good agreement with the measured data, however we observed some differences. The proposed method was used to characterize a scintillation decay time of CsI(Tl) excited with pulsed X-rays and gamma rays. It was found that X-ray pulses produce a significantly different pulse shape compared to single gamma events of an energy equal to the aggregate energy deposition of multiple lower-energy x-ray photons in the pulse. We will conclude that the proposed method provides a new way of characterization of scintillators.

4.2. MATERIALS AND METHODS

4.2.1. THE SETUP

The measuring setup is shown diagrammatically in Fig. 4.1. Scintillation pulses from a one inch CsI(Tl) sample are converted to electrical pulses by a Hamamatsu H5510 Photomultiplier Tube (PMT). The scintillation crystal is optically coupled with silicon oil to the PMT's entrance window. The PMT's anode signal is connected directly to the 10-bit 4 Giga Samples Per Second (GSPS) DT5761 digitizer from CAEN. The digitizer has an input range of 1 Vpp, input impedance $Z_{in} = 50\ \Omega$, and a memory buffer depth of $7.2{\cdot}10^6$ samples. No preamplifier nor other ways of analog signal shaping have been used. All data

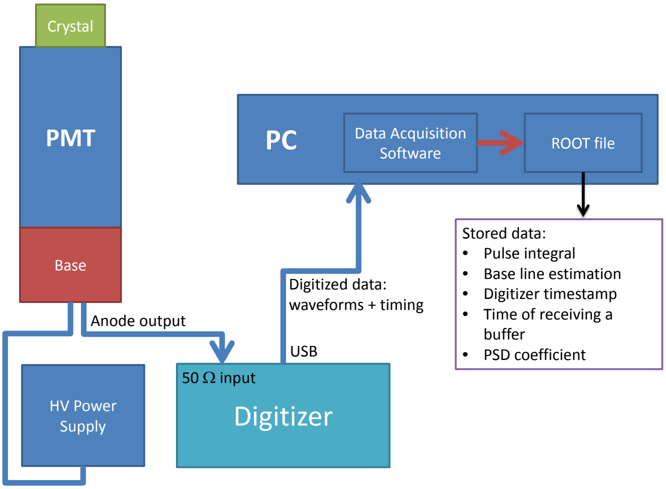

Figure 4.1: Schematic of the Time Resolved Gamma Spectroscopy setup. The gamma source or a pulsed X-ray tube excite the scintillation crystal. The resulting scintillation pulses are detected with a photomultiplier tube and digitized on event-by-event principle.

acquisition and on-line processing is done with a personal computer and homemade software *veroDigitizer*.

A ^{137}Cs source has been used for excitation. The barium X-rays (32 keV) were absorbed by a lead absorber placed between the ^{137}Cs source and the detector. In this way we avoided photoelectric absorption of low energy X-rays, and only photoelectrons or Compton electrons from 662 keV gamma interaction were detected. As an alternative to γ rays, we used a light excited X-ray tube N5084 from Hamamatsu for generation of ultra short X-ray pulses (<100 ps). The X-ray tube has a tungsten target and is powered with a 40 kV power supply. Each X-ray pulse contains multiple X-ray photons, which enables low energy excitation (~10 keV) but with a high light output.

4.2.2. DATA ACQUISITION

When the anode signal exceeds the digitizer's trigger voltage V_{tr} an event is triggered and stored in a local buffer. Each event contains a waveform consisting of 56k voltage samples (14 μs time range). When the internal buffer is full, all digitized events are transfered to the PC for data processing. In order to record low energy events, the digitizer's trigger voltage V_{tr} was set as close as possible to the signal's base line. However, the low V_{tr} results in pick-up of noise spikes like in the exemplary pulse shown in Fig. 4.2. Fig. 4.3 shows the steps of the data processing which are required before the triggered events can be used for calculating average pulse shapes. Only events fulfilling multiple criteria are selected in order to remove unwanted noise events, suppress pile-up, and assure good quality of each triggered pulse. The following sections will discuss in detail each step of the data processing.

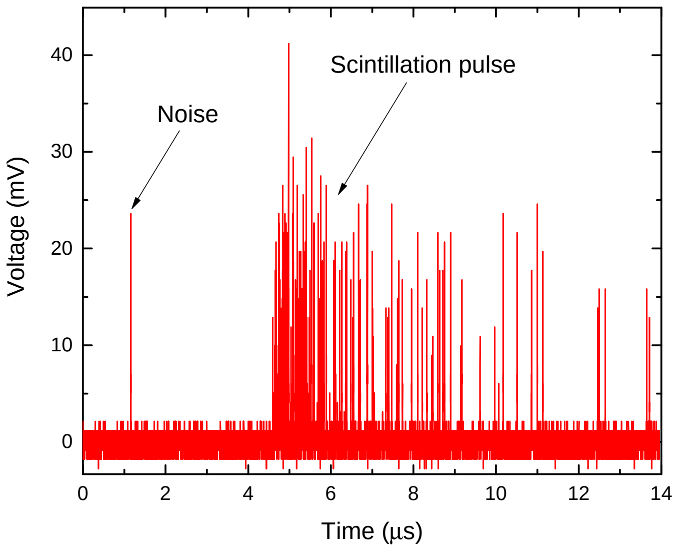

Figure 4.2: Event triggered by a noise spike at around 1 μs with a coincident scintillation pulse starting at around 5 μs.

4.2.3. FILTERING AND DECIMATION

The digitizer reduces a continuous-time signal from the PMT to a discrete-time digital signal (sampling). High sampling frequency of the used digitizer $f_s = 4$ GHz provides precise timing information, but in case of CsI(Tl) with slow decay time it results in high uncertainty of each value at a point in time of the measured signal (low signal to noise ratio). This can be seen in Fig. 4.2 and raw signal in Fig. 4.4. To increase the signal to noise ratio and decrease the uncertainty of a measured voltage each waveform was down-sampled (decimated) by first applying a low pass digital filter and then reducing the number of samples by a factor of $M = 256$.

To avoid aliasing it is needed to do a low pass filtering before downsampling [22]. The cutoff frequency of the filter has to be equal or lower than the Nyquist frequency of the down-sampled signal, which is $f_{co} = \frac{f_s/2}{M} = \frac{4000/2}{256} \approx 7.8$ MHz. Fig. 4.5 shows time and frequency domain responses of multiple standard digital filters designed for -3dB cutoff frequency at 7.8 MHz. Because in our measurements we want to preserve an undistorted time response of the signal, the filter choice is limited just to two filters: a moving average filter (length N = 227) or a Bessel filter. The moving average filter has the worst frequency response among considered filters. It has side lobes in the stop band, but provides the fastest rise time in response to the step input, and it is free of overshoots in the time domain. In addition, a recursive implementation of the moving average filter provides the shortest computation time compared to that of the other filters [22]. The moving average filter was used for the results presented here.

Each sample of the down-sampled waveform $d[i]$ is calculated by taking the average value of length $M = 256$ from the filtered waveform $f[i]$ according to the formula: $d[i] = \frac{1}{M}\sum_{k=M\cdot i}^{M\cdot(i+1)} f[i]$.

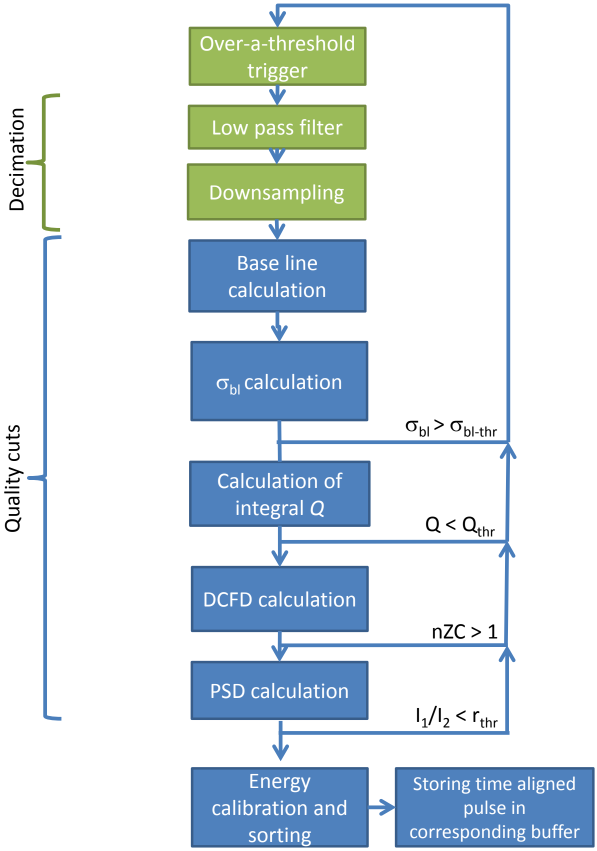

Figure 4.3: Diagram of data processing workflow. σ_{bl} is the standard deviation of the base line; σ_{bl-thr} is a maximum threshold for standard deviation of the base line; Q is the pulse integral; Q_{thr} is a pulse integral minimum threshold; nZC is the number of zero crossings in the Digital Constant Fraction Discriminator (DCFD) signal; I_1/I_2 is the pulse shape factor defined as the ratio of the short and long integration gates.

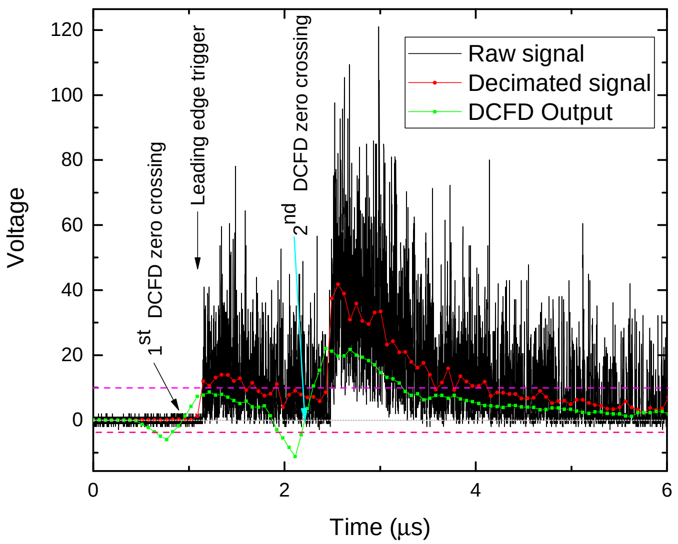

Figure 4.4: Exemplary pile-up event.

4.2.4. QUALITY CUTS

Selections were applied to data to remove noise events, assure proper triggering time within each waveform, and to select non distorted single scintillation pulses. Fig. 4.3 shows the steps of the data processing. After an event decimation a baseline BL and its' standard deviation σ_{bl} are calculated. If σ_{bl} exceeds the base line standard deviation threshold σ_{bl-thr} the event is discarded and no longer processed. In this way we assure a good quality of the calculated base line. Usually σ_{bl-thr} is exceeded when random noise is present within the base line window or a scintillation pulse was triggered too late and the leading edge is before the expected triggering time.

In the next step the integral Q of a decimated pulse is calculated using the previously obtained base line: $Q = \sum_0^L (w[i] - BL)$. If the calculated Q is lower than the minimum integral threshold Q_{thr}, the event is discarded and no longer processed. This requirement suppresses all events which exceed the digitizer's trigger threshold, but consist mostly of noise spikes, single photoelectron events, afterglow pulses, or other non-scintillation pulses. This requirement is crucial especially for low energy deposition events when noise is of the same order of magnitude as the scintillation pulses. If not suppressed properly it can lead to creation of an artificial fast component in a decay spectrum or other distortions of a pulse shape.

Fig. 4.2 shows an example of a "wrong" event: a scintillation pulse appears after the expected trigger point. A noise peak exceeded the trigger threshold and the event was digitized and stored. The scintillation pulse which coincided with the noise pulse caused that the event passed minimum energy requirement. However, the leading edge of the scintillation pulse is not properly located in the time window.

To properly measure a pulse shape it is important to suppress pile-up of scintillation events within the acquisition window. In Fig. 4.4 the black line shows a raw signal from

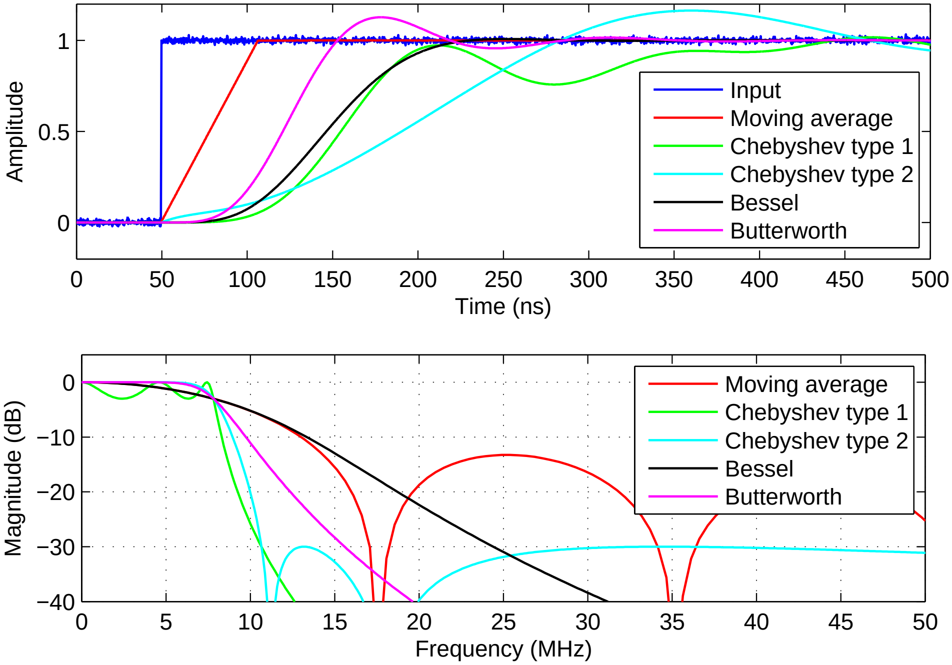

Figure 4.5: Comparison of five digital low pass filters in time (upper panel) and frequency domains (lower panel). (Colour online)

the digitizer; the red line shows the signal after low pass filtering and downsampling; the blue line shows the output of a digital constant fraction discriminator (DCFD). There are two points in the figure when the DCFD signal is crossing zero, which indicates that we are dealing with two scintillation pulses. If more then one zero crossing $nZC > 1$ was observed within the acquisition window the event was rejected from further processing. If only one zero crossing was observed the event was kept for further processing, and the zero crossing time was used later for aligning events in time.

4.3. RESULTS

Fig. 4.6 shows a pulse height spectrum measured with CsI(Tl) excited with 662 keV γ-photons. The barium x-ray peak was successfully suppressed by the lead absorber, and only Compton scattered events are present besides the 662 keV photopeak. The shown energy range was divided into 10 energy bins and an average pulse shape for each range has been calculated separately.

Fig. 4.7 shows pulse shapes of CsI(Tl) scintillation measured in multiple energy subranges. The only curve that deviates significantly is for 25-97 keV energies. Another measurement was performed with the requirement that the energy deposit is lower than 184 keV to investigate better the low energy range. Fig. 4.8 shows the decay curves at low energy deposition. The largest difference was observed for 25-41 keV events, a very small deviation was observed in the 41-89 keV range, and small but still significant pulse change was observed from 89 keV to 184 keV.

To quantify the pulse shape change shown in Fig. 4.8, the decay curves were fitted with a double exponential function $f(t) = A_1 \exp(-\frac{t}{\tau_1}) + A_2 \exp(-\frac{t}{\tau_2})$, where A_1 and A_2 are the amplitudes of the fast and the slow component, and τ_1 and τ_2 are decay times. The results of these fits are shown in Fig. 4.9 for the decay times vs energy and Fig. 4.10 for the intensities I_1 and I_2, which were calculated as follows: $I_i = \frac{A_i * \tau_i}{A_1 * \tau_1 + A_2 * \tau_2}$. Both decay constants are decreasing with decrease of energy, but there is a 'dip' present near 60 keV. The slow component decreases from around 5.8 μs to 4.7 μs in the studied energy range, while the fast component changes from around 900 ns to 850 ns.

The intensity of the slow component I_2 increases with increase of energy, see Fig. 4.10. The intensity change deviates from being smooth at energies around 50 keV, similarly to the decay components.

Fig. 4.11 shows a pulse height spectrum measured with a ^{137}Cs source together with X-ray pulses from a pulsed X-ray tube. The tube pulses are observed at equivalent deposited total energy of around 1.3 MeV with FWHM of 37%. Assuming that the average energy of a single X-ray photon from the tungsten anode is around ~10 keV, we may estimate that a single X-ray pulse leads to ~130 detected x-ray photons.

Fig. 4.12 compares a scintillation pulse shape of CsI(Tl) excited with high energy gamma photons (575-758 keV), low energy Compton electrons (25-96 keV), and pulsed X-rays (10 keV). Events excited by the pulsed x-ray tube exhibit the lowest intensity of the long decay component, while high energy γ photons have the highest intensity of the slow component. The pulses from Fig. 4.12 were fitted with a double exponential function and the results are shown in Table 4.1. The fast component under X-ray excitation is 6% faster compared to the 662 keV energy range. The slow decay constant decreases 11% in the same energy range. The intensity of the slow component increases 4.3% when the

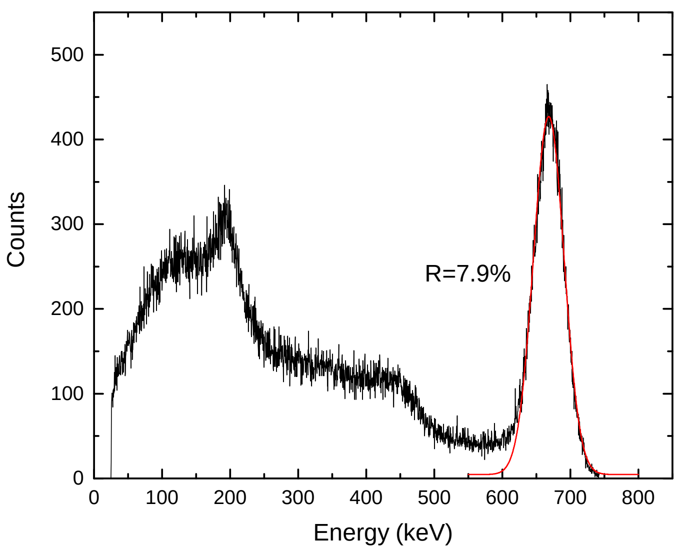

Figure 4.6: Pulse height spectrum of ^{137}Cs gamma source measured with CsI:Tl.

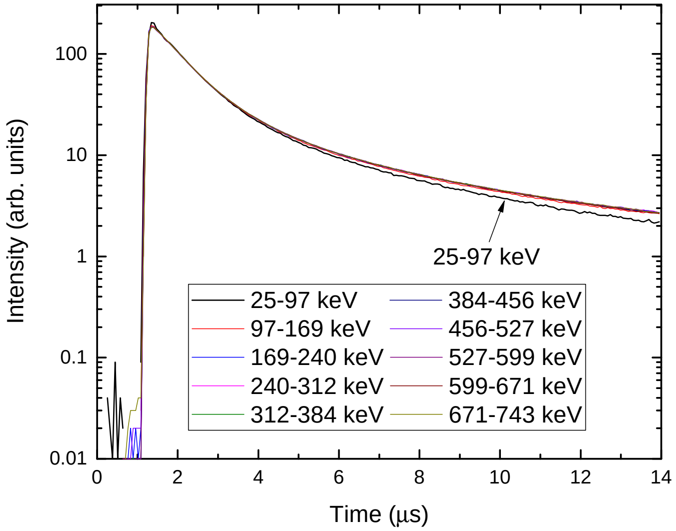

Figure 4.7: Energy-sorted pulse shapes of CsI(Tl) under Cs-137 excitation. Only the lowest energy range 25-97 keV displays a significantly different pulse shape. (Colour online)

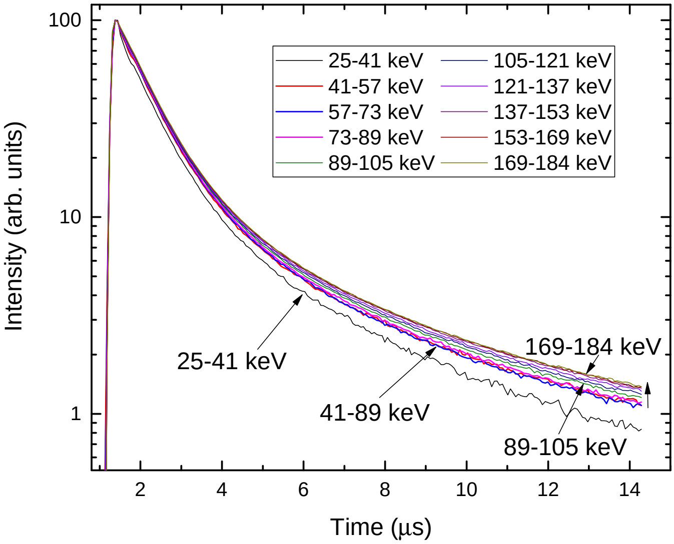

Figure 4.8: Energy-sorted pulse shapes of CsI(Tl) under Cs-137 excitation, events with energies lower then 228 keV. (Colour online)

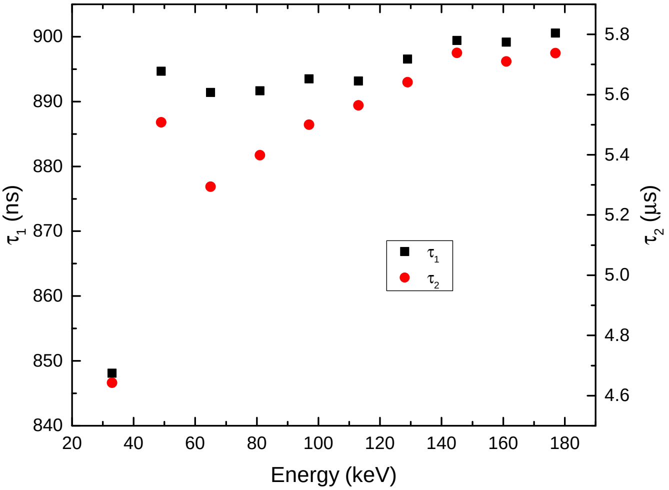

Figure 4.9: Decay constants of fast τ_1 and τ_2 slow luminescence decay components.

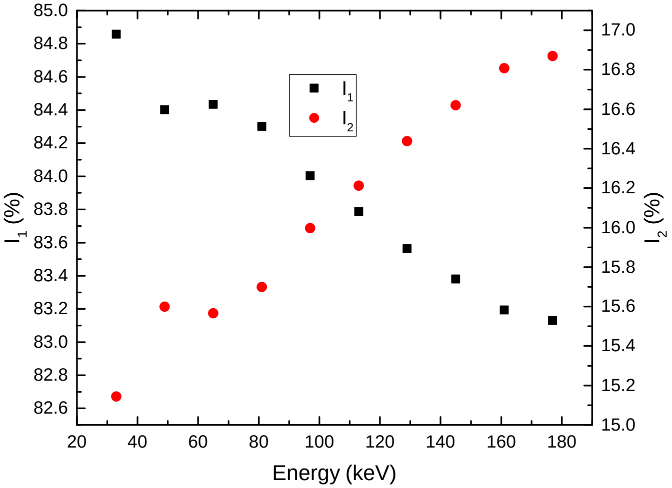

Figure 4.10: Intensities of fast I_1 and slow I_2 luminescence decay components.

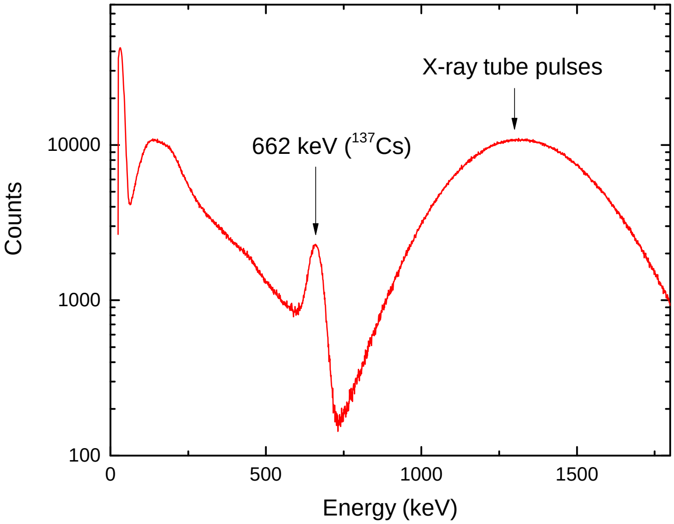

Figure 4.11: Pulse height spectrum measured with CsI(Tl) excited with a Cs-137 gamma source and pulsed X-ray tube.

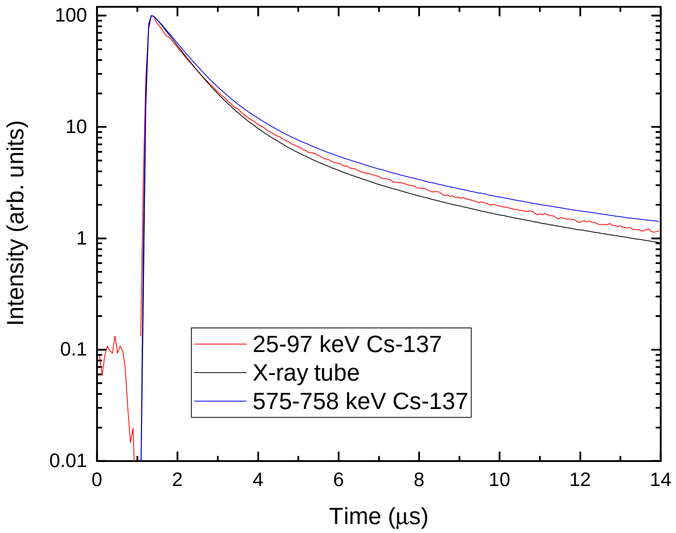

Figure 4.12: Comparison of CsI(Tl) scintillation pulse shape excited with Cs-137 gamma source and a pulsed X-ray tube. (Colour online)

Table 4.1: Decay constants and their intensities of CsI(Tl) luminescence excited with a pulsed X-ray tube, low, and high energy excitation.

Excitation	τ_1 (ns)	τ_2 (μs)	I_1 (%)	I_2 (%)
X-rays	800	4.7	87.1	12.9
25-97 keV	845	5.1	83.9	16.1
575-758 keV	850	5.3	82.8	17.2

source of excitation is changed from 662 keV to X-rays. The pulse change measured with low energy deposition (25-97 keV) compared to the 575-758 keV range is significantly smaller and it is less than 1% change of the fast decay component and less then 4% of the slow component. The change of intensity is around 1%.

The pulse shape factor was defined as a ratio of two integrals: the leading edge, and the tail part of the pulse. Length of both integrals was optimized to get the pulse shape factor value close to one. The integral limits for both edges were 1.92 μs for the early part, and 10.88 μs for the tail part of the pulse. Fig. 4.13 shows pulse shape factor versus energy of pulses. X-ray pulses (1000-2200 channels) have higher pulse shape factor then γ rays from Cs-137 source (662 keV at 800 channel).

4.4. DISCUSSION

Lu et al. [6] provided a detailed theoretical analysis of the pulse shape dependence on gamma energy in CsI(Tl). Three possible reactions leading to luminescence were considered. Reaction 1 is the direct Tl^+ excitation by sequential capture of free holes and electrons: $Tl^+ + e^- + h^+ \rightarrow (Tl^+)^* \rightarrow Tl^+ + h\nu$. Reaction 2 is the recombination of self-

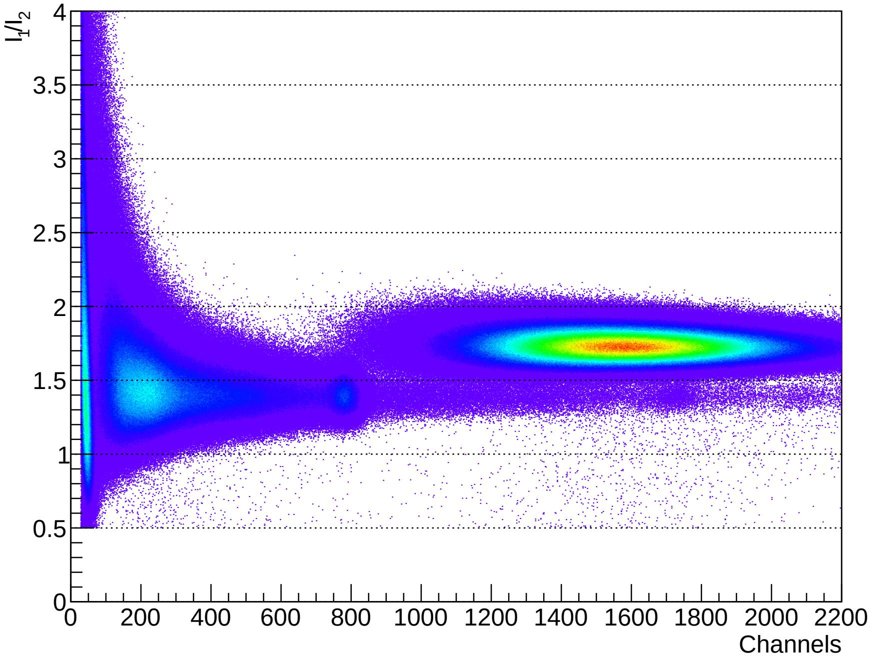

Figure 4.13: Pulse shape factor vs pulse integral. Scintillation pulses excited with X-ray tube exhibit a distinctively different shape.

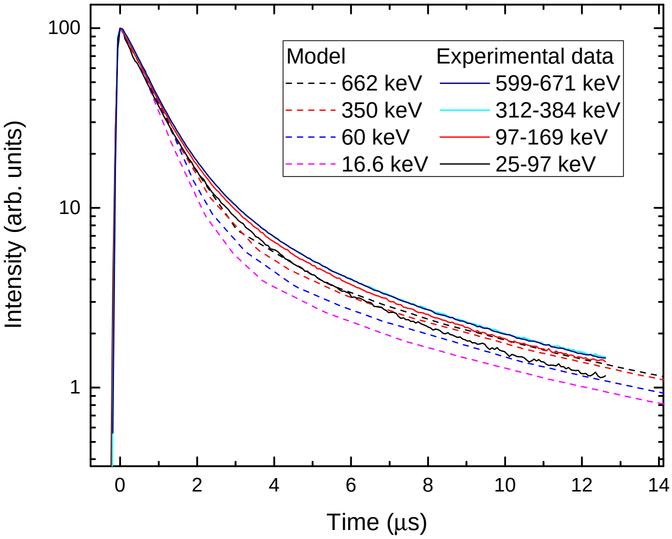

Figure 4.14: Comparison of the Lu model predictions [6] with the measured data. (Colour online)

trapped holes with electrons trapped on Tl^0: Tl^0 + STH → (Tl$^+$)*. Reaction 3 is the thermally activated release of electrons trapped as Tl^0 that subsequently recombine with holes trapped as Tl^{2+}: Tl^0 + Tl^{2+} → (Tl$^+$)*. According to Lu et al., the fast ~700 ns decay component can be mostly attributed to the 576 ns radiative decay of (Tl$^+$)* created in Reaction 2 and secondarily to a fast component of Reaction 3 found at high excitation densities. The 3- and 17-μs components are the rate- and transport-limited phases, respectively, of Reaction 3 that become more prominent at lower excitation densities. The energy dependence of the pulse shape can be explained by the change of efficiency of the Reaction 3 with excitation density, which is dependent on the electric field created between space-separated Tl^0 and Tl^{2+} reservoirs.

Fig. 4.14 shows a comparison of the theoretical modeling results by Lu [6] and experimental data presented in this work. The model provides a good qualitative description of the data; the same trend and magnitude of the experimental pulse shape change is reproduced by the calculations. However, there are some discrepancies. The model does not predict correctly a change of the slow component (~5 μs) decay constant, and the change of the fast component (~ 800 ns) is predicted to be bigger then observed in experiment. Some difficulty for a fair comparison is caused by the fact that the experimental data are measured with limited energy resolution ranges, while theoretical predictions are provided for monoenergetic gamma photons.

4.5. CONCLUSIONS

In this article we have presented a new method of charactering scintillators. We found a weak pulse shape dependence on gamma energy for CsI(Tl), and different scintillation decay time for gamma rays and X-ray pulsed excitations. The experimental results are in good agreement with theoretical predictions by Lu et al. [6], but minor differences are observed and require more research.

REFERENCES

[1] P. Dorenbos, J. de Haas, and C. van Eijk, *Non-proportionality in the scintillation response and the energy resolution obtainable with scintillation crystals,* IEEE Transactions on Nuclear Science **42**, 2190 (1995).

[2] R. Williams, J. Q. Grim, Q. Li, K. Ucer, G. Bizarri, S. Kerisit, F. Gao, P. Bhattacharya, E. Tupitsyn, E. Rowe, *et al.*, *Experimental and computational results on exciton/free-carrier ratio, hot/thermalized carrier diffusion, and linear/nonlinear rate constants affecting scintillator proportionality,* in *Hard X-Ray, Gamma-Ray, and Neutron Detector Physics XV*, Vol. 8852 (International Society for Optics and Photonics, 2013) p. 88520J.

[3] J. Q. Grim, K. B. Ucer, A. Burger, P. Bhattacharya, E. Tupitsyn, E. Rowe, V. M. Buliga, L. Trefilova, A. Gektin, G. A. Bizarri, W. W. Moses, and R. T. Williams, *Nonlinear quenching of densely excited states in wide-gap solids,* Phys. Rev. B **87**, 125117 (2013).

[4] G. Bizarri, N. J. Cherepy, W. S. Choong, G. Hull, W. W. Moses, S. A. Payne, J. Singh, J. D. Valentine, A. N. Vasilev, and R. T. Williams, *Progress in studying scintillator proportionality: Phenomenological model,* IEEE Transactions on Nuclear Science **56**, 2313 (2009).

[5] X. Lu, Q. Li, G. A. Bizarri, K. Yang, M. R. Mayhugh, P. R. Menge, and R. T. Williams, *Coupled rate and transport equations modeling proportionality of light yield in high-energy electron tracks: CsI at 295 K and 100 K; CsI:Tl at 295 K,* Phys. Rev. B **92**, 115207 (2015).

[6] X. Lu, S. Gridin, R. T. Williams, M. R. Mayhugh, A. Gektin, A. Syntfeld-Każuch, Ł. Świderski, and M. Moszyński, *Energy-Dependent Scintillation Pulse Shape and Proportionality of Decay Components for CsI:Tl: Modeling with Transport and Rate Equations,* Phys. Rev. Applied **7**, 014007 (2017).

[7] L. Dinca, P. Dorenbos, J. de Haas, V. Bom, and C. V. Eijk, *Alpha–gamma pulse shape discrimination in CsI:Tl, CsI:Na and* BaF_2 *scintillators,* Nuclear Instruments and Methods in Physics Research Section A: Accelerators, Spectrometers, Detectors and Associated Equipment **486**, 141 (2002), proceedings of the 6th International Conference on Inorganic Scin tillators and their Use in Scientific and Industrial Applications.

[8] M. Kobayashi, Y. Tamagawa, S. Tomita, A. Yamamoto, I. Ogawa, and Y. Usuki, *Significantly different pulse shapes for* γ*- and* α*-rays in* $Gd_3Al_2Ga_3O_{12}{:}Ce^{3+}$ *scintillating crystals,* Nuclear Instruments and Methods in Physics Research Section A: Accelerators, Spectrometers, Detectors and Associated Equipment **694**, 91 (2012).

[9] L. Bardelli, M. Bini, P. Bizzeti, F. Danevich, T. Fazzini, N. Krutyak, V. Kobychev, P. Maurenzig, V. Mokina, S. Nagorny, M. Pashkovskii, D. Poda, V. Tretyak, and S. Yurchenko, *Pulse-shape discrimination with* $PbWO_4$ *crystal scintillators,* Nuclear

Instruments and Methods in Physics Research Section A: Accelerators, Spectrometers, Detectors and Associated Equipment **584**, 129 (2008).

[10] K. Yang, P. R. Menge, and V. Ouspenski, *Enhanced* α *-* γ *discrimination in co-doped* $LaBr_3$*:Ce,* IEEE Transactions on Nuclear Science **63**, 416 (2016).

[11] S. Rawat, M. Tyagi, P. Netrakanti, V. Kashyap, A. Singh, D. Desai, A. Mitra, G. A. Kumar, and S. Gadkari, *Pulse shape discrimination properties of* $Gd_3Ga_3Al_2O_{12}$*:Ce,B single crystal in comparison with CsI:Tl,* Nuclear Instruments and Methods in Physics Research Section A: Accelerators, Spectrometers, Detectors and Associated Equipment , (2016).

[12] K. Mesick, D. Coupland, and L. Stonehill, *Pulse-shape discrimination and energy quenching of alpha particles in* $Cs_2LiLaBr_6$*:*Ce^{3+}*,* Nuclear Instruments and Methods in Physics Research Section A: Accelerators, Spectrometers, Detectors and Associated Equipment **841**, 139 (2017).

[13] N. Zaitseva, B. L. Rupert, I. Pawełczak, A. Glenn, H. P. Martinez, L. Carman, M. Faust, N. Cherepy, and S. Payne, *Plastic scintillators with efficient neutron/gamma pulse shape discrimination,* Nuclear Instruments and Methods in Physics Research Section A: Accelerators, Spectrometers, Detectors and Associated Equipment **668**, 88 (2012).

[14] P. Belli, R. Bernabei, R. Cerulli, C. Dai, F. Danevich, A. Incicchitti, V. Kobychev, O. Ponkratenko, D. Prosperi, V. Tretyak, and Y. Zdesenko, *Performances of a* CeF_3 *crystal scintillator and its application to the search for rare processes,* Nuclear Instruments and Methods in Physics Research Section A: Accelerators, Spectrometers, Detectors and Associated Equipment **498**, 352 (2003).

[15] R. Ogawara and M. Ishikawa, *Feasibility study on signal separation for spontaneous alpha decay in* $LaBr_3$*:Ce scintillator by signal peak-to-charge discrimination,* Review of Scientific Instruments **86**, 085108 (2015), http://dx.doi.org/10.1063/1.4928115.

[16] C. M. Whitney, L. Soundara-Pandian, E. B. Johnson, S. Vogel, B. Vinci, M. Squillante, J. Glodo, and J. F. Christian, *Gamma–neutron imaging system utilizing pulse shape discrimination with clyc,* Nuclear Instruments and Methods in Physics Research Section A: Accelerators, Spectrometers, Detectors and Associated Equipment **784**, 346 (2015), symposium on Radiation Measurements and Applications 2014 (SORMA XV).

[17] R. Cerulli, P. Belli, R. Bernabei, F. Cappella, F. Nozzoli, F. Montecchia, A. d'Angelo, A. Incicchitti, D. Prosperi, and C. Dai, *Performances of a* BaF_2 *detector and its application to the search for* $\beta\beta$ *decay modes in* ^{130}Ba*,* Nuclear Instruments and Methods in Physics Research Section A: Accelerators, Spectrometers, Detectors and Associated Equipment **525**, 535 (2004).

[18] A. Syntfeld-Każuch, M. Moszyński, Ł. Świderski, W. Klamra, and A. Nassalski, *Light pulse shape dependence on* γ*-ray energy in CsI(Tl),* IEEE Transactions on Nuclear Science **55**, 1246 (2008).

[19] W.-S. Choong, G. Bizarri, N. Cherepy, G. Hull, W. Moses, and S. Payne, *Measuring the dependence of the decay curve on the electron energy deposit in NaI(Tl),* Nuclear Instruments and Methods in Physics Research Section A: Accelerators, Spectrometers, Detectors and Associated Equipment **646**, 95 (2011).

[20] X. Wen and A. Enqvist, *Measuring the scintillation decay time for different energy deposited by* γ*-rays and neutrons in a* $Cs_2LiYCl_6{:}Ce^{3+}$ *detector,* Nuclear Instruments and Methods in Physics Research Section A: Accelerators, Spectrometers, Detectors and Associated Equipment **853**, 9 (2017).

[21] Ł. Świderski, M. Moszyński, A. Syntfeld-Każuch, M. Szawłowski, and T. Szcześniak, *Measuring the scintillation decay time for different energy depositions in NaI:Tl, LSO:Ce and* $CeBr_3$ *scintillators,* Nuclear Instruments and Methods in Physics Research Section A: Accelerators, Spectrometers, Detectors and Associated Equipment **749**, 68 (2014).

[22] S. W. Smith, *The Scientist and Engineer's Guide to Digital Signal Processing* (California Technical Publishing, San Diego, CA, USA, 1997).

5

$\mathrm{CsBa_2I_5{:}Eu^{2+},Sm^{2+}}$ - THE FIRST HIGH RESOLUTION BLACK SCINTILLATOR FOR γ-RAY SPECTROSCOPY

> *At a time when science plays such a powerful role in the life of society, when the destiny of the whole of mankind may hinge on the results of scientific research, it is incumbent on all scientists to be fully conscious of that role, and conduct themselves accordingly.*
>
> Joseph Rotblat

Scintillators are materials that absorb a high energy particle (α, β, γ radiation) and down-convert its energy into a short pulse of visible or near-visible light. The ultimate energy resolution for γ-photon detection as determined by photon detection statistics can only be approached for materials that show a perfect proportional response with γ-energy. A large amount of research has resulted in the discovery of highly proportional materials like $SrI_2{:}Eu^{2+}$ and $CsBa_2I_5{:}Eu^{2+}$. However, the resolution is still limited because of unavoidable self-absorption of Eu^{2+} emission especially when large sized scintillators are to be used. By co-doping with Sm^{2+} the emission of Eu^{2+} can be efficiently shifted to the far-red by exploiting non-radiative energy transfer. Here we apply that new idea to

---

This chapter is adapted from: **W. Wolszczak**, K. W. Kramer, P. Dorenbos, *$CsBa_2I_5{:}Eu^{2+},Sm^{2+}$ - The first high energy resolution black scintillator for γ-ray spectroscopy*, physica status solidi (RRL)–Rapid Research Letters, 2019.

CsBa$_2$I$_5$:Eu^{2+}. With emission wavelength around 755 nm, remarkable high energy resolution of 3.2% at 662 keV gamma excitation, and scintillation decay time of 2.1 μs, Sm codoped CsBa$_2$I$_5$:Eu^{2+} can be considered as the first black scintillator. The proposed double-doping principle can be used to develop an entirely new class of Near-Infrared (NIR) scintillators. Readout with high quantum efficiency silicon based photo-detectors instead of traditional photomultiplier tubes may then improve energy resolution to beyond the current resolution record of 2%.

5.1. INTRODUCTION

A precise measurement of γ-ray energy is a mayor requirement in nuclear spectroscopy, nuclear safeguarding, environmental monitoring, academic research, and medical imaging. Such requirement has powered extensive research to develop a scintillator with ultimate energy resolution [1]. Past 20 years the focus has been on Ce^{3+} and Eu^{2+} activated halide (chloride, bromide, and iodide) compounds with impressive results [2–6]. The latest development pushed the resolution limit to 2.0% at 662 keV γ-photon detection in $LaBr_3$:Ce,Sr [7], and this material holds the record for the best energy resolution obtained with an inorganic scintillator up today.

The fundamental limit in energy resolution as determined by Poisson statistics in the number of detected photons is almost reached with $LaBr_3$:Ce,Sr. To go beyond the 2% energy resolution, the number of detected photons needs to be significantly larger which requires a new approach in scintillation research. A small bandgap scintillator, needed to attain the highest light yield, must be combined with a highly sensitive photon detector.

Figure 5.1a shows the quantum efficiency (QE) curves for a bi-alkali photomultiplier tube (PMT) and of an avalanche photodiode (APD), and the photon detection efficiency (PDE) of a Si-photomultiplier (Si-PM). All commercial scintillators of today are developed for the ultraviolet or blue spectral range: NaI:Tl 410 nm [8], $LaBr_3$:Ce^{3+} 380 nm [3], $CeBr_3$ 380 nm [9], SrI_2:Eu^{2+} 430 nm [6]. Fig. 5.1a shows that such emission matches well the maximum sensitivity between 400-440 nm of PMTs. The quantum efficiency of 26-28% [10] is moderate, although it can reach up to 35% for a superbialkali photocathode. In contrary, modern large area APD silicon photodetectors offer quantum efficiency up to 80-90%, with a maximum sensitivity at longer wavelengths around 600-800 nm. The QE of an APD is limited mostly by silicon reflectivity, and the effective quantum efficiency can even be increased to around 98% by back-reflecting scintillation light towards the APD with appropriate scintillator encapsulation [11]. To exploit this high QE, it is required to develop a new class of scintillating materials with long-wavelength emission in the red or NIR.

Previous attempts to obtain efficient red emitting scintillators have failed. CaF_2:Sm^{2+} has 725 nm luminescence [12], but the low density of CaF_2 discards it from use in gamma spectroscopy. $Gd_3Al_2Ga_3O_{12}$:Yb^{3+} offers 650 to 1200 nm infra-red scintillation, but 4f-4f forbidden luminescence of ytterbium is much too slow for applications in scintillation counting [13]. Lu_2S_3:Ce^{3+} with maximum of emission at 592 nm was reported to be a promising red-emitting scintillator [14], but sulfide single crystals were found to be difficult to grow in large sizes required for efficient γ-photons absorption. A material which is probably closest to meet the requirements for a red scintillator is $LaBr_3$:Pr^{3+} [15]. It has good energy resolution of 3.2% at 662 keV gamma excitation and emission between 450 and 900 nm, but it has slow decay time of 11 μs and little advantage above $LaBr_3$:Ce^{3+}. In this work we will exploit Sm^{2+} as a new scintillating center that emits in the NIR where the APD has maximum efficiency. We will also exploit the known excellent scintillation performance of $CsBa_2I_5$:Eu^{2+} with a yield of 90'000 photons per MeV (ph/MeV) and 2.3% energy resolution at 662 keV γ-detection [16, 17]. The $CsBa_2I_5$ lattice enables incorporation of high Eu^{2+} concentration which increases efficiency of electron-hole capture from the ionization track created by a high energy particle. However, the blue Eu^{2+} emission needs to be measured with a PMT and high Eu^{2+} concen-

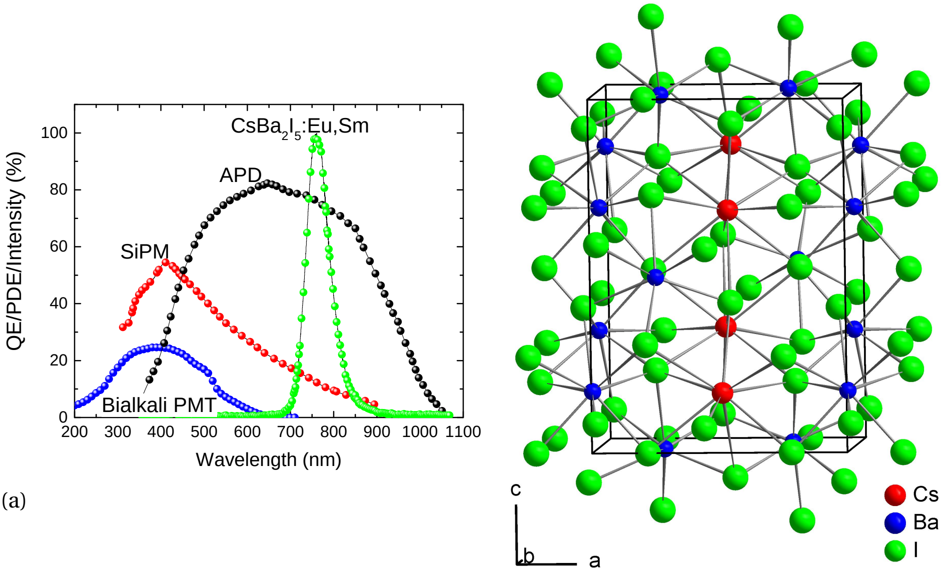

(a)

(b)

Figure 5.1: a) Quantum efficiencies of different types of photodetectors together with the emission of $CsBa_2I_5$:Eu,Sm, b) view onto the crystal structure of $CsBa_2I_5$ along the b-axis.

tration results in increased self-absorption and a light loss depending on the interaction point inside the crystal. This leads to energy resolution deterioration with increasing crystal size. Sm^{2+} as a co-dopant with a strong absorption in the Eu^{2+} emission range enables efficient energy transfer from Eu^{2+} to Sm^{2+} which radically shifts emission into the NIR. Self-absorption losses are avoided and high quantum efficiency Si-photodetectors can be used. The principle was first demonstrated for SrI_2:Eu,Sm, however, energy resolution was poor and increased concentration of Sm quenched the luminescence [18]. In this work we present $CsBa_2I_5$:2%Eu,1%Sm as the first successful material which offers both NIR emission and excellent energy resolution in γ-ray spectroscopy.

5.2. SAMPLE PREPARATION AND CRYSTAL GROWTH

Crystals of $CsBa_2I_5$: Eu^{2+}, Sm^{2+} were grown by the Bridgman technique from anhydrous CsI, BaI_2, EuI_2, and SmI_2. CsI (Merck, p.a.) was dried in vacuum at 400°C. BaI_2 was prepared from $BaCO_3$ (Alfa Aesar, 4N7) and HI acid (57%, Merck, p.a.), dried in vacuum, and crystallized from the melt for purification. EuI_2 and SmI_3 were synthesized from the elements in sealed silica ampoules. Eu and Sm (Metall Rare Earth Limited, 3N) were slowly heated to 500°C and 400°C, respectively, until the reaction was finished. Iodine (Merck, p.a.) was kept in the colder part of the ampoule to avoid overpressure. EuI_2 and SmI_3 were sublimed for purification in Ta ampoules under vacuum at 1000°C and 800°C, respectively. SmI_2 was obtained from SmI_3 and Sm in a Ta ampoule at 900°C.

For crystal growth stoichiometric amounts of the starting materials were sealed in silica ampoules under vacuum. $CsBa_2I_5$ melts congruently at 610 °C. After heating to 625°C the melt was slowly cooled to room temperature within 10 days. All handling of the starting materials and products was done under strictly dry and oxygen free conditions in a glove box (MBraun, Garching) or sealed sample containers.

5.3. EXPERIMENTAL METHODS

Optically excited luminescence spectra were measured with an FL-1039 Horiba 450 W Xenon lamp combined with a Gemini-180 Horiba double-grating monochromator. The emission from the sample was dispersed with an Acton SP2300 Princeton Instruments monochromator and detected with a Hamamatsu C9100-13 CCD camera.

X-ray excited luminescence spectra were recorded using an X-ray tube with tungsten anode. The emission from the sample was dispersed with an ARC VM504 monochromator and recorded with a Hamamatsu R493-02 PMT. The emission was not corrected for the monochromator transmission nor quantum efficiency of the PMT.

The scintillation decay time profiles were measured with the time-correlated single photon counting (TCSPC) method. The setup consists of a PicoQuant LDH-P-C-440M pulsed diode laser, a Hamamatsu N5084 light-excited x-ray tube, and an ID Quantique id100-50 single-photon counter. The laser driver was triggered from a Hewlett Packard function generator. The driver's reference output was connected to the start input of an Ortec 567 time-to-amplitude converter (TAC), while the photon counter was connected to the stop input. An Ortec AD114 amplitude-to-digital converter was used to digitize and collect the start-stop time differences. An Ortec 462 time calibrator was used to determine the TAC bin width.

γ-ray excited Pulse Height Spectra (PHS) were recorded with an Advanced Photonix Avalanche Photo-Diode 630-70-72-510, connected to a Cremat CR-112 pre-amplifier, and an Ortec 672 spectroscopic amplifier with 10 μ shaping time. The sample was mounted in a pressed-Teflon holder, and placed 0.1 mm from the surface of the APD. The APD temperature was stabilized at T=270K by a two stage Peltier device and a LakeShore temperature controller. The APD bias voltage was 1690V. The crystals were mounted without any optical coupling, and the APD was used without any protective entrance window.

γ-ray excited PHS were recored with a Broadcom AFBR-S4N44C013 Silicon Photomultiplier, connected directly to 50 Ω input of a CAEN DT5761 digitizer. Temperature of the SiPM was not actively stabilized, however, the setup was contained in a closed box and measurements were performed in a stable environment of a dry nitrogen glove-box. Home made software was used for data acquisition. Each scintillation pulse was numerically integrated for 10 μs, and the integrals were used for creation of a PHS.

5.4. RESULTS

$CsBa_2I_5$ crystallizes in the monoclinic $TlPb_2Cl_5$ structure [19] with space group $P12_1/c1$. The structure shown in Fig. 5.1b contains $[CsI_9]$ and $[Ba(1)I_8]$ polyhedra that share triangular faces and form chains along the a-axis. They are interconnected by halide bridges and $[Ba(2)I_7]$ polyhedra. The density calculated on basis of crystallographic data is 4.77

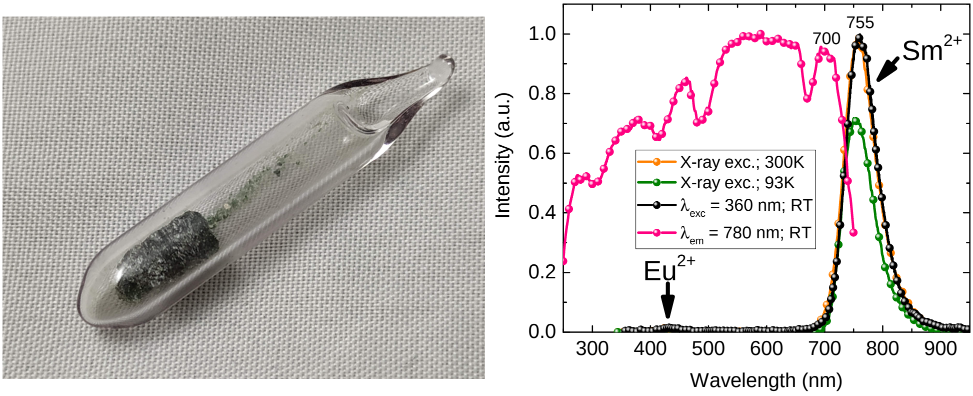

(a)

(b)

Figure 5.2: a) photo of the black scintillator in a quartz vial, b) optical and X-ray excited emission and excitation spectra.

g/cm^3. Eu^{2+} and Sm^{2+} are assumed to occupy a Ba^{2+} site. Fig. 5.2a shows the studied black $\mathrm{CsBa_2I_5}$:2%Eu,1%Sm sample which needs to be encapsulated in a quartz vial because it is hygroscopic. Fig. 5.2b shows the optical emission excited at 360 nm and the excitation spectra at room temperature. 99.5% of the emission comes from Sm^{2+} 5d-4f emission at 755 nm and a weak contribution is from Eu^{2+} near 430 nm. Emission from both luminescence centers becomes broader at 300 K, which can be explained by the standard theory on electron-phonon coupling. The Sm^{2+} absorption and luminescence excitation covers the entire visible range which explains the black color of the sample. The X-ray excited emission at 300K is more intense than at 93 K and is spectrally identical to the photon excited emission. There were no signs of thermal quenching up to 350 K. Fig. 5.3a shows the pulsed X-ray excited scintillation decay profile at 300K. The main decay component of 2.1 μs is fast enough for γ-ray nuclear spectroscopy but too slow for high-count rate application.

Fig. 5.3b shows the pulse height spectrum using a ^{137}Cs radioactive source emitting 662 keV γ photons and 32 keV X-ray photons for the scintillator coupled to an APD. From the total absorption peak at 662 keV we obtain a light yield of 45’000 ph/MeV and an energy resolution of 3.2% , expressed as the full width at half maximum (FWHM) intensity. This is narrow enough to observe the X-ray escape peak at 29 keV lower energy. 45’000 ph/MeV are still missing, but considering that crystal growth and the Eu and Sm concentrations are not yet optimized, the observed yield and 3.2% resolution is regarded an excellent result for a first trial into this new research direction. Fig. 5.4 and the pulse height spectrum for CsI:Tl in Fig. 5.3b demonstrates that energy resolution of $\mathrm{CsBa_2I_5}$:Eu,Sm stands-out when compared with other long-wavelength commercially available scintillators.

Instead of an APD one may also use a Si-PM for scintillation detection. The PDE for a Si-PM, as shown in Fig.5.1a, has maximum sensitivity at 400 nm and extends to 900 nm. In the case of recently developed infra-red (IR) enhanced Si-PMs, the detectors reach

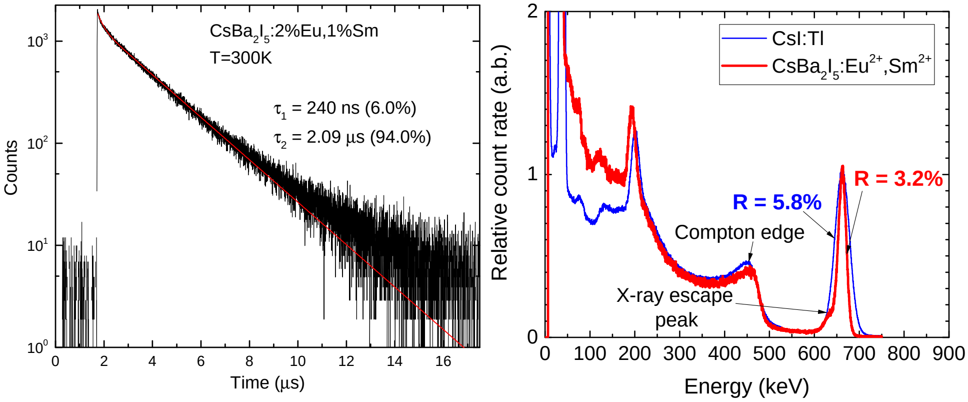

(a)

(b)

Figure 5.3: a) pulsed X-ray excited scintillation decay, b) pulse height spectra of CsBa$_2$I$_5$:Eu,Sm and CsI:Tl coupled to an APD and excited with 662 keV γ-rays.

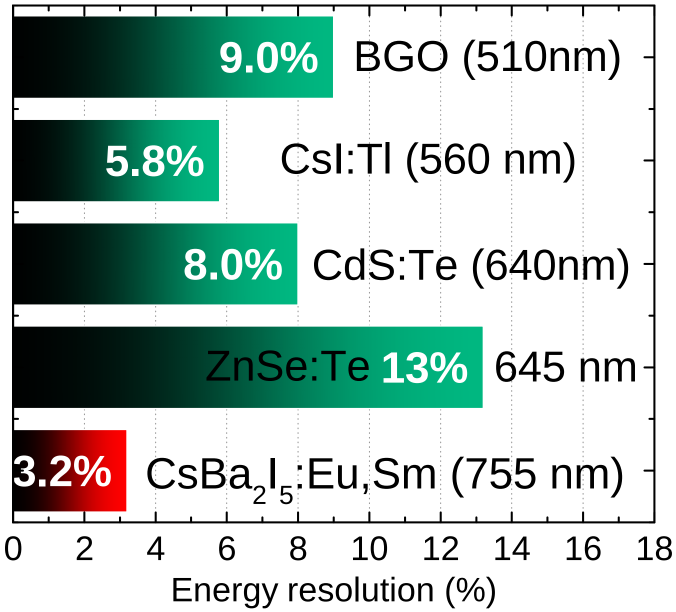

Figure 5.4: Energy resolution at 662 keV of various commercial scintillators with long wavelength emission

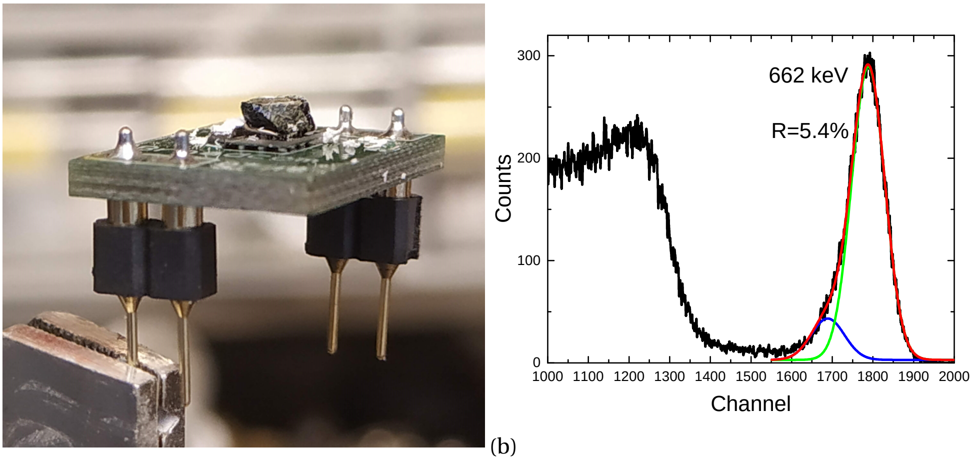

(b)

(a)

Figure 5.5: $CsBa_2I_5$:Eu,Sm application in nuclear spectroscopy. a) a Si-PM with a $CsBa_2I_5$:Eu,Sm sample mounted on top, b) the pulse height spectrum of $CsBa_2I_5$:Eu,Sm coupled to a SiPM and excited with 662 keV γ-rays.

over 20% QE at 690 nm [20]. Furthermore, the development of NIR sensitive Si-PMs is a current objective for developing LIDAR sensors for self-driving car applications, and we anticipate rapid development and further enhanced sensitivity in the 700-1100 nm range. Because Si-PMs are very low cost (~30 US$), not sensitive to magnetic fields, and small they enable the development of compact and portable gamma spectrometers at relatively low price. As a first assessment, we coupled a crystal of $CsBa_2I_5$:Eu,Sm to a Si-PM as shown in Fig. 5.5a. The ^{137}Cs pulse height spectrum in Fig. 5.5b shows an energy resolution of 5.4%. It is worse than the 3.2% with the APD mainly because of the 4-5 times lower QE, but still it demonstrates a low cost and miniaturized gamma spectrometer.

A gamma photon can interact with a scintillator by three basic interactions. 1) Compton scattering which is responsible for the Compton edge and Compton continuum in the spectrum of Fig. 5.3b. 2) The photoelectric effect which is responsible for the photopeak at 662 keV, and 3) pair production which only becomes important well above 1.022 MeV. Different interactions dominate depending on initial energy, but the final product of each is a hot cloud of charge carriers inside an ionization track. After an ionized track is created, hot electrons and holes thermalize to the conduction band bottom and valence band top through interactions with phonons as illustrated in Fig. 5.6a. Because of different dispersion relation of holes and electrons, holes reach the top of the valence band much faster than electrons the bottom of the conduction band. In addition, a strong Fröhlich coupling constant to optical phonons leads to rapid self-trapping of the holes. The self-trapping process has been studied extensively in alkali halides, and is very typical for halide materials. A recent study [21] showed that most holes are even self-trapped before they reach the activator dopant in the scintillator. After the charge carriers have been trapped at Eu^{2+}, energy is transferred non-radiative to Sm^{2+} which is then followed by the dipole allowed 5d-4f emission at 755 nm. The transfer at the chosen

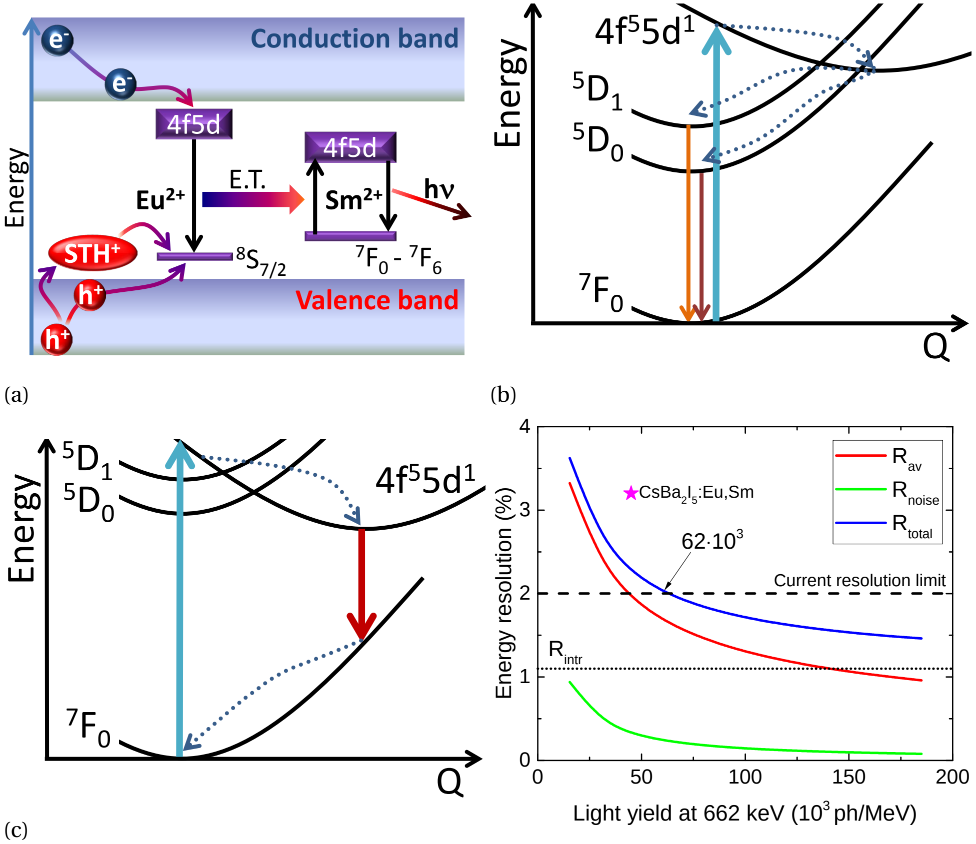

(a) (b) (c) (d)

Figure 5.6: Scintillation mechanism, theoretically predicted energy resolution, and requirements for Sm^{2+} 5d-4f emission. a) Illustration of the scintillation mechanism of $CsBa_2I_5$:Eu,Sm, b) and c) configuration coordination diagrams for the Sm^{2+} levels in two different host materials, d) the different contributions R_{intr}=1.1%, R_{av}, R_{noise}, and R_{inh}=0% to the energy resolution R_{total} as function of the light yield.

dopant concentrations appears very efficient because Fig. 5.2b shows that 99.5% of light emission originates from Sm^{2+}, while only 0.5% from Eu^{2+}.

The reason to select Sm^{2+} as a new activator in scintillators is because it can, depending on type of compound, show dipole-allowed 5d-4f luminescence in the infrared. Sm^{2+} has a $4f^6$ electron configuration and the relevant $^7F_0$, $^5D_0$, and $^5D_1$ 4f-levels are shown in the configuration coordinate diagram of Fig. 5.6b. After energy transfer from Eu^{2+}, Sm^{2+} is in its lowest $4f^55d^1$ state. Unlike the 4f-levels, this state has a strong interaction with the environment leading to a configurational coordinate offset in the excited state parabola, and the energy depends on type of compound. Fig. 5.6b shows a situation where the $4f^55d^1$ level is located well above the $^5D_0$ level. This results in relaxation to the $^5D_0$ or $^5D_1$ levels followed by forbidden and very slow (~1 ms) emission of no use for scintillation applications. In iodides like $CsBa_2I_5$ the 5d level is at lower energy and the situation shown in Fig. 5.6c applies. Now the $4f^55d^1$ level is below the $^5D_0$ level and the desired relatively fast 5d-4f emission is observed.

5.5. DISCUSSION

The energy resolution R_{total} of a scintillator coupled to an APD can be written as $R^2_{total} = R^2_{intr} + R^2_{av} + R^2_{noise} + R^2_{inh}$, where R_{intr} is the contribution from non-proportional response, also called the intrinsic resolution, $R_{av} = 2.35\sqrt{F/N_{eh}}$ is the contribution from the APD avalanche gain fluctuations and from counting statistics, $R_{noise} = 2.35\sigma_{noise}/N_{eh}$ is a contribution from the APD noise, and R_{inh} is related to crystal inhomogeneity [22]. F is the excess noise factor of an APD and N_{eh} is the number of electron-hole pairs generated in the APD by a scintillation pulse. σ_{noise} is the standard deviation in the noise contribution arising from surface and bulk charge recombination of an APD and expressed in RMS electrons. Fig. 5.6d shows the different contributions for realistic values of $F = 2$, $\sigma_{noise} = 40$ electrons RMS, effective QE = 98%, and $R_{intr} = 1.1\%$, and assuming a perfect crystal with R_{inh}=0. The curve for the total energy resolution R_{total} crosses the current resolution record of 2% when the scintillation yield passes 62'000 ph/MeV at 662 keV. This is not an unusually high light yield, and it has been observed for various Eu^{2+} doped iodide scintillators. This implies that for each of those scintillators we may add Sm^{2+} to shift the emission to wavelengths where an APD has maximum sensitivity, and then it is well-feasible to go below 2% energy resolution. Iodide compounds are then the most likely candidates because they already demonstrated the required scintillation yield with Eu^{2+} activation, and the iodides are known to have low intrinsic resolution [23] . In our first attempt we already achieved 3.2% resolution with $CsBa_2I_5$. The data point in Fig. 5.6d shows the current result. The arrow points at the projected result when we can improve crystal quality and manage to recover the 45'000 ph/MeV loss.

5.6. CONCLUSIONS

By adding Sm^{2+} to $CsBa_2I_5$:Eu^{2+} energy transfer from Eu to Sm results into an efficient 755 nm near infra-red emitting scintillator. The ^{137}Cs pulse height spectrum with 3.2% energy resolution at 662 keV with APD read-out can be considered as the birth certificate of the first black scintillator. There are many other potential iodide compounds where the new research strategy can be applied to, and a realistic evaluation shows that resolution lower than 2% is well-feasible. We also demonstrated 5.4% resolution with a very low cost Si-PM. Such a detector can for example easily be incorporated into miniature portable γ-spectrometers, even in a smartphone type of device, for safety applications.

REFERENCES

[1] C. Dujardin, E. Auffray, E. Bourret-Courchesne, P. Dorenbos, P. Lecoq, M. Nikl, A. N. Vasil'ev, A. Yoshikawa, and R. Y. Zhu, *Needs, trends, and advances in inorganic scintillators,* IEEE Transactions on Nuclear Science **65**, 1977 (2018).

[2] M. S. Alekhin, D. A. Biner, K. W. Krämer, and P. Dorenbos, *Improvement of*

$LaBr_3$:5%Ce scintillation properties by Li^+, Na^+, Mg^{2+}, Ca^{2+}, Sr^{2+}, and Ba^{2+} co-doping, Journal of Applied Physics **113**, 224904 (2013).

[3] E. Van Loef, P. Dorenbos, C. Van Eijk, K. Krämer, and H.-U. Güdel, *High-energy-resolution scintillator: Ce^{3+} activated $LaBr_3$,* Applied physics letters **79**, 1573 (2001).

[4] G. Bizarri, E. D. Bourret-Courchesne, Z. Yan, and S. E. Derenzo, *Scintillation and optical properties of BaBrI:Eu^{2+} and $CsBa_2I_5$:Eu^{2+},* IEEE Transactions on Nuclear Science **58**, 3403 (2011).

[5] U. Shirwadkar, J. Glodo, E. V. van Loef, R. Hawrami, S. Mukhopadhyay, A. Churilov, W. M. Higgins, and K. S. Shah, *Scintillation properties of $Cs_2LiLaBr_6$ (CLLB) crystals with varying Ce^{3+} concentration,* Nuclear Instruments and Methods in Physics Research Section A: Accelerators, Spectrometers, Detectors and Associated Equipment **652**, 268 (2011), symposium on Radiation Measurements and Applications (SORMA) XII 2010.

[6] N. J. Cherepy, B. W. Sturm, O. B. Drury, T. A. Hurst, S. A. Sheets, L. E. Ahle, C. K. Saw, M. A. Pearson, S. A. Payne, A. Burger, L. A. Boatner, J. O. Ramey, E. V. van Loef, J. Glodo, R. Hawrami, W. M. Higgins, K. S. Shah, and W. W. Moses, *SrI_2 scintillator for gamma ray spectroscopy,* (2009) pp. 7449 – 7449 – 6.

[7] M. S. Alekhin, J. T. M. de Haas, I. V. Khodyuk, K. W. Krämer, P. R. Menge, V. Ouspenski, and P. Dorenbos, *Improvement of γ-ray energy resolution of $LaBr_3$:Ce^{3+} scintillation detectors by Sr^{2+} and Ca^{2+} co-doping,* Applied Physics Letters **102**, 161915 (2013).

[8] R. Hofstadter, *The detection of gamma-rays with thallium-activated sodium iodide crystals,* Phys. Rev. **75**, 796 (1949).

[9] K. S. Shah, J. Glodo, W. Higgins, E. V. D. van Loef, W. W. Moses, S. E. Derenzo, and M. J. Weber, *$CeBr_3$ scintillators for gamma-ray spectroscopy,* IEEE Transactions on Nuclear Science **52**, 3157 (2005).

[10] *Photomultiplier Tubes*, Philips photonics (Philips, 1993).

[11] I. Holl, E. Lorenz, and G. Mageras, *A measurement of the light yield of common inorganic scintillators,* IEEE Transactions on Nuclear Science **35**, 105 (1988).

[12] L. C. Dixie, A. Edgar, and C. M. Bartle, *Samarium doped calcium fluoride: A red scintillator and x-ray phosphor,* Nuclear Instruments and Methods in Physics Research Section A: Accelerators, Spectrometers, Detectors and Associated Equipment **753**, 131 (2014).

[13] A. Suzuki, S. Kurosawa, S. Nagata, T. Yamamura, J. Pejchal, A. Yamaji, Y. Yokota, K. Shirasaki, Y. Homma, D. Aoki, T. Shikama, and A. Yoshikawa, *Crystal Growth and Luminescence Properties of Yb-doped $Gd_3Al_2Ga_3O_{12}$ Infra-red Scintillator,* Optical Materials **36**, 1484 (2014).

[14] J. van't Spijker, P. Dorenbos, C. Allier, C. van Eijk, A. Ettema, and G. Huber, *Lu_2S_3:Ce^{3+}, A new red luminescing scintillator,* Nuclear Instruments and Methods in Physics Research Section B: Beam Interactions with Materials and Atoms **134**, 304 (1998).

[15] J. Glodo, R. Farrell, E. V. D. van Loef, W. M. Higgins, and K. S. Shah, *$LaBr_3$: Pr^{3+} - A new red-emitting scintillator,* in *IEEE Nuclear Science Symposium Conference Record, 2005*, Vol. 1 (2005) pp. 98–101.

[16] M. S. Alekhin, D. A. Biner, K. W. Krämer, and P. Dorenbos, *Optical and scintillation properties of $CsBa_2I_5$:Eu^{2+},* Journal of Luminescence **145**, 723 (2014).

[17] E. Bourret-Courchesne, G. Bizarri, R. Borade, Z. Yan, S. Hanrahan, G. Gundiah, A. Chaudhry, A. Canning, and S. Derenzo, *Eu^{2+}-doped Ba_2CsI_5, a new high-performance scintillator,* Nuclear Instruments and Methods in Physics Research Section A: Accelerators, Spectrometers, Detectors and Associated Equipment **612**, 138 (2009).

[18] R. Awater, M. Alekhin, D. Biner, K. Krämer, and P. Dorenbos, (2019), , in review.

[19] G. Schilling and G. Meyer, *Ternäre Bromide und Iodide zweiwertiger Lanthanide und ihre Erdalkali-Analoga vom Typ AMX_3 und AM_2X_5,* Zeitschrift für anorganische und allgemeine Chemie **622**, 759 (1996), https://onlinelibrary.wiley.com/doi/pdf/10.1002/zaac.19966220502 .

[20] F. Acerbi, G. Paternoster, A. Gola, N. Zorzi, and C. Piemonte, *Silicon photomultipliers and single-photon avalanche diodes with enhanced NIR detection efficiency at FBK,* Nuclear Instruments and Methods in Physics Research Section A: Accelerators, Spectrometers, Detectors and Associated Equipment **912**, 309 (2018), new Developments In Photodetection 2017.

[21] X. Lu, Q. Li, G. A. Bizarri, K. Yang, M. R. Mayhugh, P. R. Menge, and R. T. Williams, *Coupled rate and transport equations modeling proportionality of light yield in high-energy electron tracks: CsI at 295 K and 100 K; CsI:Tl at 295 K,* Phys. Rev. B **92**, 115207 (2015).

[22] M. Moszyński, M. Szawłowski, M. Kapusta, and M. Balcerzyk, *Large area avalanche photodiodes in scintillation and x-rays detection,* Nuclear Instruments and Methods in Physics Research Section A: Accelerators, Spectrometers, Detectors and Associated Equipment **485**, 504 (2002).

[23] W. Wolszczak and P. Dorenbos, *Nonproportional response of scintillators to alpha particle excitation,* IEEE Transactions on Nuclear Science **64**, 1580 (2017).

6

ENGINEERING NEAR-INFRARED EMITTING SCINTILLATORS WITH EFFICIENT EU^{2+} → SM^{2+} ENERGY TRANSFER

> *A man can control only what he comprehends, and comprehend only what he is able to put into words. The inexpressible therefore is unknowable.*
>
> Stanisław Lem, The Futurological Congress

In this chapter we present a concept to develop a new class of Near-Infrared (NIR) scintillators employing efficient Eu^{2+} → Sm^{2+} energy transfer. By studying optical spectroscopy of BaBrI:Eu,Sm we derived a criterion for obtaining fast Sm^{2+} 5d→4f emission. By exploiting lanthanides phenomenology we created a list of possible new NIR scintillators.

6.1. INTRODUCTION

Scintillators are important materials used for detection of ionizing radiation [1–3]. They can absorb a high energy particle and down-convert its energy into a short pulse of visible light. The linear dependence between the absorbed energy and the number of emitted photons is the basis of gamma spectroscopy. Scintillators are used in numerous applications like homeland security [4], medical imaging [5], space exploration [6–8], or high energy physics [9, 10]. High energy resolution is one of the important properties vital for these applications.

Europium-doped halide scintillators (SrI_2:Eu^{2+} [11], BaBrI:Eu^{2+} [12], $CsBa_2I_5$:Eu^{2+} [13]) are among the ones that offer the highest energy resolution and light yield [14].

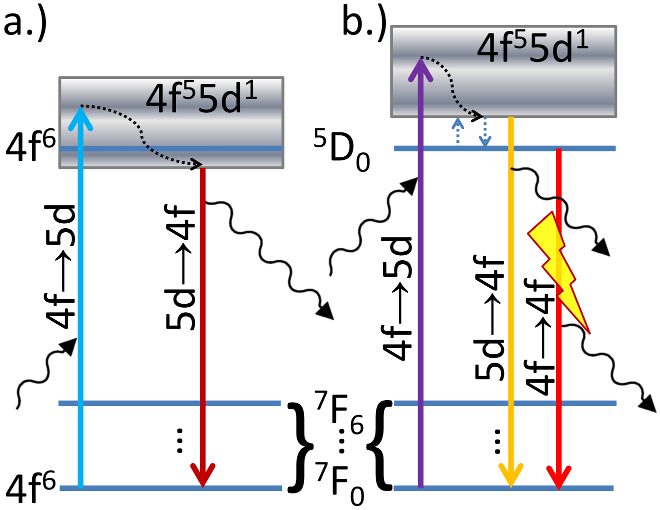

Figure 6.1: Energy level diagram of two distinctive locations of the lowest 4f level in respect to 4f5d levels. a.) The lowest excited 4f level is above minimum 5d level b.) The lowest excited 4f level is below minimum 5d level.

One of the reasons is that Eu^{2+} can be incorporated in high concentration without concentration quenching. However, the re-absorption of Eu^{2+} luminescence by other Eu^{2+} atoms (self-absorption) is detrimental to the scintillation process in large crystals required for γ-spectroscopy. It affects decay time, light yield, and energy resolution [11]. One possible solution to that problem can be addition of a co-dopant at low concentration which absorbs Eu^{2+} emission and re-emits it at a longer wavelength. The idea has been verified recently in SrI_2:Eu,Sm [15] and $CsBa_2I_5$:Eu,Sm (Chapter 5). Besides limiting the self-absorption, shifting the wavelength emission to NIR can be a way to energy resolution better than 2%, see Chapter 5 and Fig. 5.6d.

Sm^{2+} has [Xe]$4f^6$ electronic configuration in its ground state [16]. It can be excited to $4f^6$ states or to $4f^5 5d^1$ states (4f5d for short). The energy of 4f lanthanide electrons is weakly affected by the host environment. However, the electron at the $5d^1$ orbital is not screened, and its energy can be controlled by changing the host environment. The 4f→4f transitions of lanthanide ions are parity-forbidden, have very slow decays (~ 1ms) and narrow emission lines, and are characterized by narrow absorption lines. Thus, the 4f→4f transitions are not suitable for application in scintillators. The allowed 5d→4f transitions show broad spectral bands with high absorption and emission intensities and short luminescence decay time (~ 1μs). These spin and parity allowed 5d→4f transitions can be used for developing new scintillators [1].

Fig. 6.1 shows two examples of distinctive energy locations of the $4f^5 5d^1$ level in two different host environments. Fig. 6.1 a.) shows a desired case for scintillation applications. It is when the bottom of the $4f^5 5d^1$ band is below the $^5D_0$ level of the $4f^6$ electron configuration. As a result, parity-allowed 5d→4f emission is dominating. Fig. 6.1 b.) illustrates the situation when the bottom of the $4f^5 5d^1$ band is above the $^5D_0$ level. The emission branches between the parity-allowed 5d→4f and the parity-forbidden 4f→4f emission. The intensities depend on the transition probability and the population of the states. In addition, thermally-excited transitions from the $^5D_0$ state to the $4f^55d^1$ state may make the situation even more complex and dependent on temperature.

In this article we explore a possibility of efficient energy transfer between europium and samarium for scintillation applications. As a starting point we have chosen barium bromide iodide BaBrI, as it is a high density host with experimentally proven high energy resolution of 3.4% at 662 keV γ-excitation, and high light yield of 97,000 photoelectrons/MeV [12]. We will present x-ray and optical characterization of BaBrI:Eu,Sm, and derive a criterion for a host in which Sm^{2+} has fast 5d→4f emission.

6.2. SAMPLE SYNTHESIS AND CRYSTAL GROWTH

$BaBrI:Eu^{2+},Sm^{2+}$ was synthesized from stoichiometric amounts of the binary halides $BaBr_2$, BaI_2, EuI_2, and SmI_2. $BaBr_2$ and BaI_2 were prepared from $BaCO_3$ (Alfa Aesar, 4N7). The carbonate was dissolved in concentrated hydrobromic (Merck, suprapur 47%) or hydroiodic acid (Merck, suprapur 57%), respectively. The product was dried up on a sandbath, heated to 450°C in vacuum ($< 10^{-3}$ mbar), and purified by Bridgman crystal growth in a glassy carbon ampoule. EuI_2 was synthesized from Eu metal (Stanford materials, 4N) and iodine (Merck, p.a.). The starting materials were sealed in a silica ampoule under vacuum. The ampoule was heated in a tube furnace keeping the colder end at about 100°C to avoid an overpressure. The metal was slowly heated and kept at 500°C until the iodine had reacted completely. EuI_2 was sublimed for purification in a tantalum ampoule under vacuum at 1000°C. SmI_3 was prepared in a similar way from Sm metal (Alfa, 3N). The ampoule was heated to 400°C and SmI_3 was sublimed at 800°C in a silica ampoule. SmI_2 was obtained by reacting SmI_3 with Sm in a tantalum ampoule at 900°C for 2 days. The tantalum ampoule was sealed by He-arc welding and encapsulated into a silica ampoule under vacuum.

Crystals of BaBrI:Eu,Sm were grown by the Bridgman technique using a vertical, static ampoule with seed selection tip and a moving furnace. The starting materials were sealed in a silica ampoule under vacuum and heated to 780°C for 1 day. BaBrI melts congruently at 770°C. Then the furnace was slowly moved up by a controlled stepper motor with 0.6 mm/hour cooling the crystal to room temperature within about 10 days. The ampoules were opened in a glove box (MBraun, Graching, D) equipped with a microscope and with water and oxygen values < 0.1 ppm. Crystals were cleaved from the boule and pieces of about 5 mm size were sealed in small silica ampoules for further spectroscopic characterization. The phase purity of the product was verified by powder X-ray diffraction on a Stoe Stadip diffractometer in Bragg-Brentano (reflection) geometry with $CuK_{\alpha 1}$ radiation from a curved (101) α-SiO_2 monochromator and a linear position sensitive detector. BaBrI adopts the $PbCl_2$ crystal structure (orthorhombic, Pnma, no. 62) as its parent compounds $BaBr_2$ and BaI_2 [17]. Since starting materials and products are hygroscopic all handling was done under strictly dry conditions in glove boxes or sealed containers.

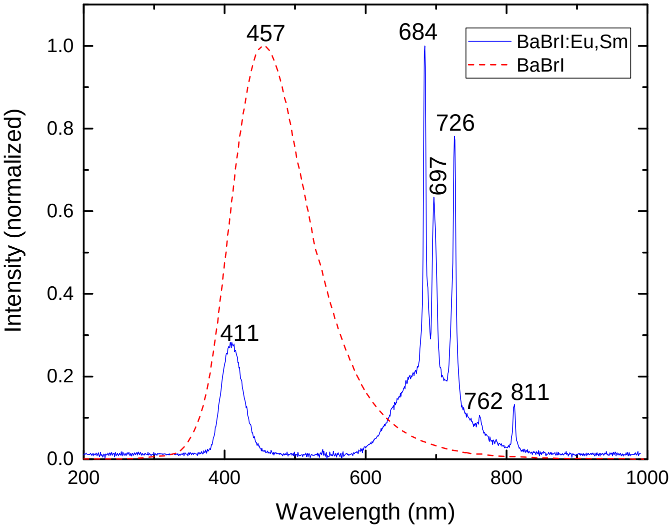

Figure 6.2: X-ray excited emission spectra of BaBrI and BaBrI:Eu,Sm.

6.3. EXPERIMENTAL METHODS

X-ray excited emission spectra were measured with an X-ray tube with a cobalt anode operating at 60 kV and 10 mA. The emission was recored using an Ocean Optics optical fiber detector. Photoluminescence excitation and emission measurements were made with an Ekspla NT230 Optical Parametric Oscillator (OPO) laser or Newport 66921 xenon lamp excitation in combination with a Horiba Gemini 180 monochromator. The emission light of the sample was dispersed with a Princeton Instruments Acton SP 2300 and detected with a Hamamatsu R7600U-20 (300-920 nm) or R7600U-03 (185-650 nm) photomultiplier tube (PMT), or a Hamamatsu C9100-13 electron multiplier CCD camera. Time resolved spectra were recorded using a CAEN DT5724 or DT5730 digitizer connected to one of the PMTs and controlled by home made software. The sample was placed in a Janis Research VPF-700 cryostat, and its' temperature has been stabilized with a LakeShore 331 controller. A closed cycle helium chiller has been used for low temperature measurements.

6.4. RESULTS

Fig. 6.2 shows X-ray excited emission spectra of pure BaBrI host and BaBrI:5%Eu^{2+},0.5%Sm^{2+} at room temperature. The host emission is characterized by a single broad peak with maximum at 457 nm, and the peak is absent in the Eu and Sm doped sample. In the BaBrI:Eu,Sm sample we can identify the 411 nm peak as 5d→4f emission of Eu^{2+}, and Sm^{2+} emission is between 600 and 820 nm. Sm^{2+} emission consists of a broad 5d→4f band at ~700 nm, and five sharp lines which can be ascribed to parity forbidden 4f→4f transitions.

Fig. 6.3 shows photoluminescence and photoluminescence excitation spectra measured at room temperature and 13 K. The optically excited luminescence spectrum at

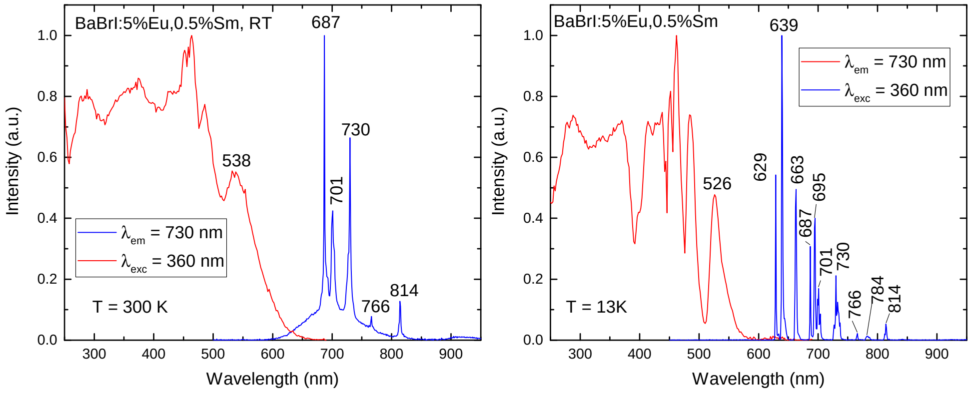

(a) (b)

Figure 6.3: Emission and excitation spectra of BaBrI:5%Eu,0.5%Sm at a) room temperature and b) 13 K.

room temperature is identical to the X-ray excited emission in Fig. 6.2. A small ~3 nm shift observed between both spectra is due to a calibration uncertainty of the two different spectrometers used for each measurement. The room temperature excitation spectrum shown in Fig. 6.3a has a distinctive peak at 538 nm which can be ascribed to 4f→5d excitation of Sm^{2+}. Excitation wavelengths from 400 to 600 nm are responsible for a direct Sm^{2+} excitation, while below 400 nm we expect both a direct Sm^{2+} excitation and Eu^{2+} excitation with a following energy transfer to Sm^{2+}.

Fig. 6.3b depicts a significant change of the emission spectrum at 13K. The broad 5d→4f emission at ~700 nm disappears, and five new sharp lines appear. The excitation spectrum is much better resolved at 13 K (Fig. 6.3b) than at room temperature (Fig. 6.3a) and clearly shows a series of Sm^{2+} 4f→5d excitation bands between 400 and 600 nm. The lowest excitation peak is shifted compared to room temperature from 538 nm to 526 nm, and an additional shoulder at around 540 nm appears. These two excitation bands are usually referred as samarium A and B bands [18]; in this case 540 nm and 526 nm, correspondingly.

Fig. 6.4a shows BaBrI:Eu,Sm emission spectra at 16 K and 300 K compared with 4f→4f Sm^{2+} transition energies measured in BaClF:Sm^{2+} by Kiss and Weakliem [19]. A good match is observed between 4f→4f transition energies in both compounds, and it illustrates a low sensitivity of 4f→4f transitions energies on the host environment. The $^5D_0 \rightarrow {}^7F_J$ transitions with J=0-4 can be easily identified as dominating at room temperature. The strongest line at 1.804 eV (687 nm) is the $^5D_0 \rightarrow {}^7F_0$ transition. $^5D_1 \rightarrow {}^7F_J$ emissions with J=0-5 arise at low temperature and become dominating. No de-excitation to the $^7F_6$ level is observed. The broad 5d→4f band is absent at 16 K. We conclude that in BaBrI:Eu,Sm we deal with the situation shown in Fig. 6.1 b). Tab. 6.1 collects all wavelengths and energies of the observed 4f→4f transitions. Fig. 6.4b shows the room temperature spectrum with a Gaussian function fitted to the spectrum with 4f→4f peaks masked. The band center is at 1.755 eV which corresponds to 707 nm emission.

The anticipated energy transfer from Eu^{2+} to Sm^{2+} is not 100% efficient at room tem-

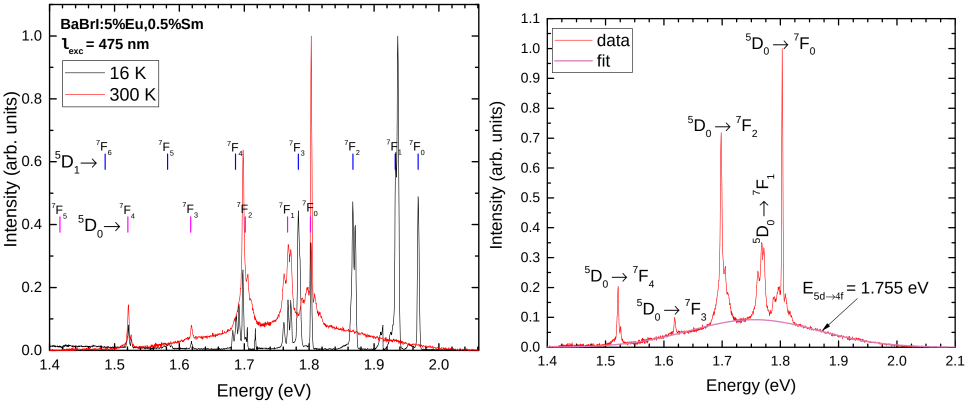

(a)

(b)

Figure 6.4: a.) Emission spectrum of BaBrI:5%Eu,0.5%Sm excited at 475 nm with OPO laser at 16K and 300K. b.) Gaussian fit of Sm^{2+} 5d→4f emission peak under 4f→4f lines observed at 300 K.

perature and light emission is from both luminescence centers, see the X-ray excited spectrum in Fig. 6.2. Fig. 6.5a shows the Eu^{2+} photoluminescence decay profile at 412 nm emission fitted with a single-exponential decay time of 365 ns. Fig. 6.5b shows the Sm^{2+} ion photoluminescence decay of the $^5D_0 \rightarrow {}^7F_0$ transition at 686 nm. The single-exponential decay time of 1024 μs is too long for most applications as a scintillator. A fast spike observed at the leading edge of Sm^{2+} emission in Fig. 6.5b comes from the 5d→4f emission band which overlaps with all 4f→4f lines, and it has decay time of 14 ns. Such short decay time can be explained with fast depopulation of the 4f5d level to the lower energy $^5D_0$ level.

Table 6.1: Energies of 4f-4f transitions of Sm^{2+}.

Excited state	Ground state	Wavelength (nm)	Energy (eV)
$^5D_0$	$^7F_0$	687	1.805
	$^7F_1$	702	1.766
	$^7F_2$	730	1.699
	$^7F_3$	767	1.617
	$^7F_4$	815	1.521
$^5D_1$	$^7F_0$	629	1.971
	$^7F_1$	640	1.938
	$^7F_2$	663	1.870
	$^7F_3$	695	1.784
	$^7F_4$	733	1.692
	$^7F_5$	784	1.582

Fig. 6.6 and 6.7 show time-resolved photoluminescence of BaBrI:Eu,Sm at room and 11 K temperature. Fig. 6.6 is characterized by a Gaussian band from fast 5d→4f Sm^{2+} emission, and following it slow 4f→4f line emissions. The line emissions are on top of

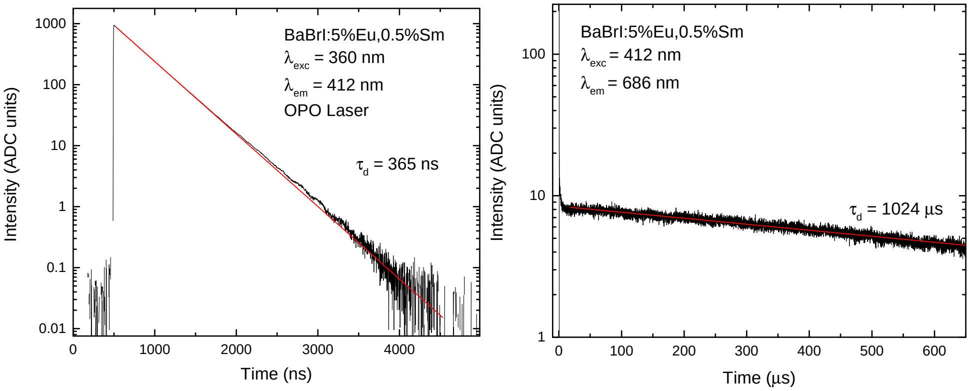

(a) (b)

Figure 6.5: a.) Photoluminescence decay profile of BaBrI:5%Eu,0.5%Sm recorded at room temperature using 360 nm optical excitation and emission observed at 412 nm (Eu^{2+} 4f-5d transition). b.) Photoluminescence decay profile of BaBrI:5%Eu,0.5%Sm recorded at room temperature using 412 nm optical excitation and emission observed at 686 nm (Sm^{2+} $^5D_0 \rightarrow ^7F_0$ transition).

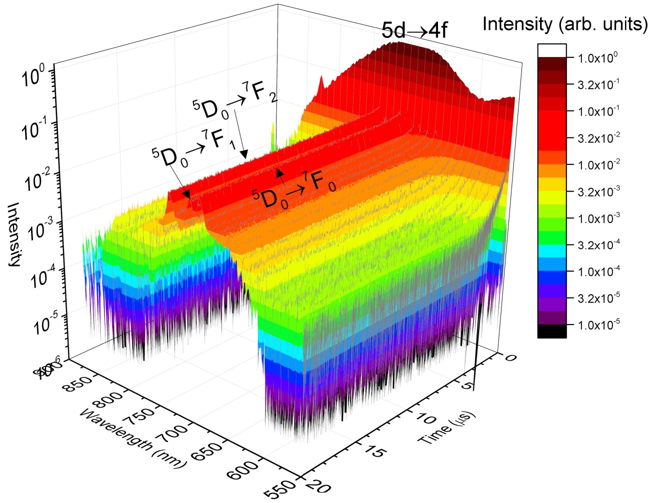

Figure 6.6: Time-resolved photoluminescence of BaBrI:5%Eu,0.5%Sm at room temperature excited at 410 nm with an OPO laser.

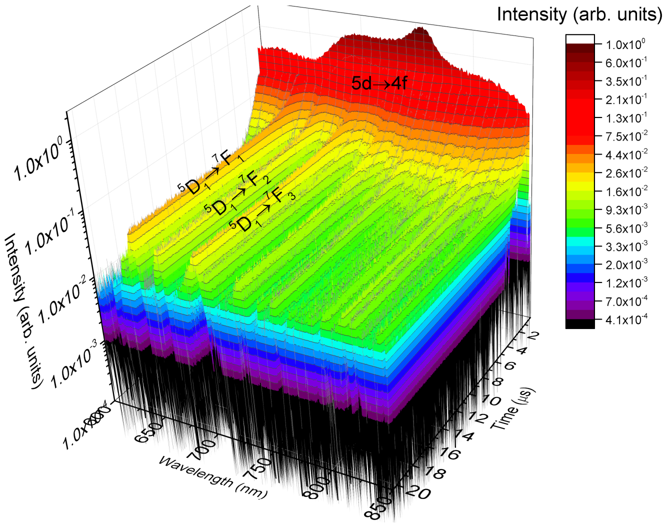

Figure 6.7: Time resolved photoluminescence of BaBrI:5%Eu,0.5%Sm at 11 K excited at 360 nm with an OPO laser..

a Gaussian shape emission long time after the initial fast 5d→4f emission has decayed. This suggest thermal re-population of the emitting 4f5d state from the lower energy $^5D_0$ state. The situation changes significantly at 11K in Fig. 6.7, when the 5d→4f emission is observed after the excitation, and it completely decays within 2 μs. Apparently, thermal re-population of the 4f5d state is impossible at 11 K, so only initially excited 5d→4f emission can be detected.

Fig. 6.8 shows time-gated emission spectra of Sm^{2+} at room and 10 K temperatures. A short 100 ns gate enables elimination of slow 4f→4f emission from the emission spectrum, and only fast 5d→4f emission is observed. The peak at room temperature is very broad, and has no structure. Measurement at 10 K reveals structure in the band, and sub-bands at 1.627, 1.76, and 1.993 eV can be distinguished. This suggests that multiple 4f final state levels are involved in 5d→4f emission resulting in a multi-peak structure in the emission spectrum.

6.5. DISCUSSION

6.5.1. ENERGY TRANSFER

When the concentration of luminescence centers is high, it may be possible that two centers are close enough to enable excitation to be transferred from one to another. The energy transfer process in inorganic materials was first studied theoretically by Förster [20] and Dexter [21]. On the microscopic level, the excitation is transferred from a donor ion, D, to an acceptor ion, A, over distance R. In BaBrI:5%Eu,0.5%Sm Eu^{2+} is a donor, and Sm^{2+} is an acceptor. Initially $(Eu^{2+})^*$ is in an excited state, and Sm^{2+} is in a ground state. An interaction $\mathscr{H}$ between the ions causes transition from $|(Eu^{2+})^*, Sm^{2+}\rangle$ to

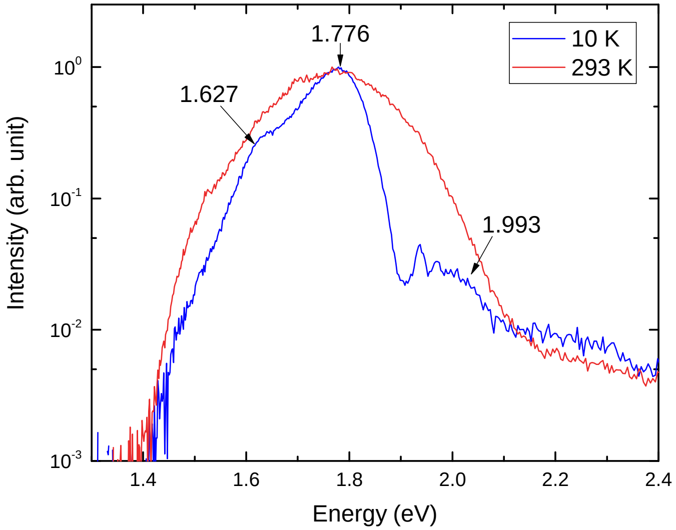

Figure 6.8: Time-gated OPO laser excited emission of Sm^{2+} at 10K and room temperature. Excitation 412 nm and 100 ns gate were used.

$|\mathrm{Eu}^{2+},(\mathrm{Sm}^{2+})^*\rangle$ state. The transition probability is

$$k_{ET} = \frac{2\pi}{\hbar}\langle(\mathrm{Eu}^{2+})^*,\mathrm{Sm}^{2+}|\mathscr{H}|\mathrm{Eu}^{2+},(\mathrm{Sm}^{2+})^*\rangle \int \epsilon_{\mathrm{Eu}}(E)\epsilon_{\mathrm{Sm}}(E)\mathrm{d}E, \qquad (6.1)$$

where $\epsilon_{\mathrm{Eu}}(E)$ and $\epsilon_{\mathrm{Sm}}(E)$ are normalized line-shape functions of europium emission and samarium absorption [22]. The interactions $\mathscr{H}$ which cause energy transfer are electrostatic/magnetic coupling, and/or exchange interaction between ions. Probability of energy transfer can be expressed in terms of the oscillator strengths in electric dipole-dipole approximation:

$$k_{ET}^{dd} = \left(\frac{1}{4\pi\epsilon_0}\right)^2 \frac{3\pi\hbar e^4}{n^4 m_e^2\omega^2}\frac{1}{R^6} f_{Eu^{2+}} f_{Sm^{2+}} \int \epsilon_{\mathrm{Eu}}(E)\epsilon_{\mathrm{Sm}}(E)\mathrm{d}E, \qquad (6.2)$$

where $f_{Eu^{2+}}$ and $f_{Sm^{2+}}$ are the oscillator strengths of the $(Eu^{2+})^* \rightarrow Eu^{2+}$ and $Sm^{2+} \rightarrow (Sm^{2+})^*$ transitions, ϵ_0 is vacuum permittivity, e is electron charge, n refractive index, m_e an electron mass, and ω is taken as the average frequency of the involved transitions. The probability of electric dipole-dipole energy transfer decreases as $1/R^6$ with a microscopic distance R between the donor and acceptor ions. On a macroscopic level there is a distribution of distances between donors and acceptors. The distribution of distances depends on the lattice structure, unit cell parameters, and the ion concentration. Low concentrations correspond to large distances and lower rate of energy transfer. The energy transfer rate is also determined by the overlap of the emission lines of the donor and the excitation lines of the acceptor.

Here we consider the simplest case where energy migration among Eu^{2+} ions is absent, and only energy transfers from Eu^{2+} to Sm^{2+} ions take place. We also assume that the average ion-ion distance does not change with time (every $(Eu^{2+})^*$ ion has a neighbor Sm^{2+} ion). Then, the energy transfer between Eu^{2+} and Sm^{2+} can been be modeled with the following set of rate equations:

$$\begin{aligned} \frac{\mathrm{d}N_{(Eu^{2+})^*}}{\mathrm{d}t} &= -\frac{N_{(Eu^{2+})^*}}{\tau_{(Eu^{2+})^*}} - \frac{N_{(Eu^{2+})^*}}{\tau_{ET}} \\ \frac{\mathrm{d}N_{(Sm^{2+})^*}}{\mathrm{d}t} &= \frac{N_{(Eu^{2+})^*}}{\tau_{ET}} - \frac{N_{(Sm^{2+})^*}}{\tau_{(Sm^{2+})^*}} \end{aligned} \tag{6.3}$$

where $N_{(Eu^{2+})^*}$ and $N_{(Sm^{2+})^*}$ are correspondingly numbers of exited Eu^{2+} and Sm^{2+} ions, $\tau_{(Eu^{2+})^*}$ and $\tau_{(Sm^{2+})^*}$ are radiative decay constants in absence of a co-dopant, and τ_{ET} is the energy transfer constant. The first equation describes the dynamics of the excited state population of Eu^{2+}. The first term describes a radiative decay of Eu^{2+}, the second is responsible for energy transfer from Eu^{2+} to Sm^{2+}. The second equation describes the dynamics of Sm^{2+}, where the first term is energy transfer while the second is Sm^{2+} radiative decay rate. We introduce the Eu^{2+} total decay rate in presence of Sm^{2+} as $k_1 = 1/\tau_{(Eu^{2+})^*} + 1/\tau_{ET}$, and the Sm^{2+} decay rate in absence of Eu^{2+} as $k_2 = 1/\tau_{(Sm^{2+})^*}$. We assume that initially only Eu^{2+} ions are excited: $N_{(Eu^{2+})^*}(t=0) = N^0_{(Eu^{2+})^*}$ and $N_{(Sm^{2+})^*}(t=0) = 0$. Thus, the set of equations 6.3 has the following solution:

$$\begin{aligned} N_{(Eu^{2+})^*}(t) &= N^0_{(Eu^{2+})^*} e^{-k_1 t} \\ N_{(Sm^{2+})^*}(t) &= N^0_{(Eu^{2+})^*} \frac{k_1}{k_1 - k_2} \left(e^{-k_2 t} - e^{-k_1 t}\right) \end{aligned} \tag{6.4}$$

We can define the energy transfer efficiency as a ratio of energy transfer rate k_{ET} to the total decay rate of the excited europium population k_1:

$$\epsilon = \frac{k_{ET}}{k_1}, \tag{6.5}$$

where k_{ET} is the rate of the non-radiative energy transfer from europium to samarium. From Eq. 6.3 we can write $k_1 = 1/\tau_{(Eu^{2+})^*} + k_{ET}$, and k_{ET} can be expressed as $k_1 - 1/\tau_{(Eu^{2+})^*}$, so the energy transfer efficiency is $\epsilon = 1 - \frac{1}{k_1 \cdot \tau_{(Eu^{2+})^*}}$. Shendrik et al. measured Eu^{2+} luminescence decay time of $\tau = 400$ ns ($\lambda_{exc} = 337$ nm) in BaBrI:0.05%Eu, and Bizarri et al. [12] obtained 420 ns in BaBrI:8%Eu ($\lambda_{exc} = 370$ nm, $\lambda_{em} = 415$ nm). Since the sample studied in this work has an intermediate europium concentration, we take the average of these data as estimation of europium decay time in absence of samarium in BaBrI:5%Eu. Decay time of photoluminescence of Eu^{2+} in presence of samarium in BaBrI:5%Eu,0.5%Sm is 365 ns (Fig. 6.5a). From this we calculate the energy transfer efficiency $\epsilon = 1 - 365/410 \approx 11\%$. This is a rather low value, and the energy transfer from europium to samarium ions seems to be inefficient. One of the reasons can be too low concentration of samarium, and too large distances between ions. This is highly improbable at the donor concentration of 5% and acceptor concentration of 0.5%. However, these are concentrations in the melt during crystal growth, and it is possible that the actual samarium concentration in the single crystal sample is much lower. The simplicity of the applied model can result in underestimated energy transfer efficiency,

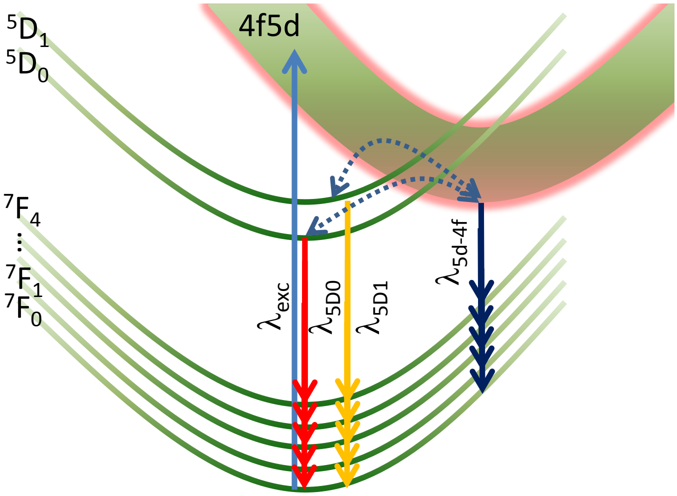

Figure 6.9: Configurational coordinates diagram of Sm^{2+} in BaBrI with depicted radiative and non-radiative processes. Solid arrows indicate radiative, dotted arrows non-radiative processes.

since we have omitted the donor-donor transfer within the europium ions population. Europium-europium energy transfer is expected to increase the chance of excitation getting in a proximity of a samarium ion, which was not included in the model. This simplification may result in underestimation of the energy transfer efficiency. However, the measured decay curves (Fig. 6.5) do not show significant deviations from the exponential behavior predicted by the model, see Eq. 6.4, so the assumed approximation seems to be justified.

Interestingly, despite the low efficiency of energy transfer and low Sm^{2+} concentration, 81% of the X-ray excited emission comes from Sm^{2+}, see Fig. 6.2. It seems that in BaBrI:5%Eu,0.5%Sm despite 10-times lower concentration of Sm^{2+} it captures about 2/3 of all electron-holes.

6.5.2. 5D→4F EMISSION OF SM^{2+}

Fig. 6.9 shows a configurational coordinates diagram of Sm^{2+} in BaBrI which explains the observed emission spectrum change with temperature in Fig. 6.6 and 6.7. At 13 K, 4f→5d excitation is followed by non-radiative relaxation to $^5D_0$ and $^5D_1$ states, and 5d→4f emission is observed only shortly after the excitation. Thermally activated transitions back to 4f5d state are impossible. As temperature rises the excited 4f5d state becomes thermally populated from the $^5D_0$ and $^5D_1$ states, and both types of luminescent transitions are observable at room temperature. The $^5D_1$ emission disappears at room temperature, which can be explained either by ionization to the conduction band or thermally-activated transition from $^5D_1$ back to 4f5d state.

Fig. 6.8 shows that the time-gated emission spectrum measured at 10 K has a structure which is not visible at room temperature. There are three peaks visible, and a shoulder at 2.3 eV extending to higher energies. Similar three-peak emission structure was observed in other Sm^{2+}-doped materials [23] and interpreted as de-excitations from the 4f5d level to the $^7F_0$, $^7F_1$, and $^7F_2$ final states [24]. However, the energy spacing between the sub-bands in Fig. 6.8 does not match the energy spacing between the $^7F_{0-2}$ final levels (Tab. 6.1). Possibly, the harmonic approximation of the proposed configurational diagram is not valid, and the change of energy level with lattice distortion is non-quadratic. Then, the spacing between levels changes at higher vibrational levels and does not reflect the same spacing as in the vibrational ground state.

To obtain the preferred 5d→4f emission for scintillation application we have to make sure that the bottom of 4f5d band is at similar or below energy as the $^5D_0$ excited state. It is known that the 4f5d level red-shifts towards lower energies with change of anion of the host according to the nephelauxetic sequence:

$$F^- < Cl^- < Br^- < I^-.$$

Iodides are then the most promising hosts for obtaining 5d→4f emission of the Sm^{2+} dopant. We can provide a much stronger and practical requirement based on systematics in lanthanide spectroscopy.

Since there are much more data on Eu^{2+} emission energy $E_{Eu^{2+}}$, we can use lanthanide phenomenology to predict Sm^{2+} emission. Dorenbos showed that the 4f5d level energy of divalent lanthanides is linearly correlated [16]. The energy of Sm^{2+} 5d→4f emission can be written as:

$$E_{Sm^{2+}} = E_{Eu^{2+}} - 1.22 \text{ eV}. \tag{6.6}$$

Based on the knowledge of the location of $^5D_0$ level we can state a criterion for 5d→4f emission as follows: $E_{Sm^{2+}} < 1.805$ eV. If we include 25 meV margin for thermal excitation it results in a requirement that europium emission energy must be lower than 2.995 eV or

$$\lambda^{\text{em.}}_{Eu^{2+}} > 414 \text{ nm}. \tag{6.7}$$

On basis of this requirement we propose in Tab. 6.2 suitable candidate scintillators for applying the Eu^{2+}→Sm^{2+} energy transfer mechanism. We selected europium doped materials with known high light yield and high energy resolution, and calculated the expected Sm^{2+} emission wavelengths using Eq. 6.6. These values agree well with measured optical Sm^{2+} 5d→4f emissions in $CsBa_2I_5$ (Chapter 5), SrI_2 [25], BaBrI (Fig. 6.4b), and $CsSrI_3$ (Chapter 7).

6.6. CONCLUSIONS

BaBrI:5%Eu,0.5%Sm is one of the first scintillating materials with double doping. BaBrI is a "border-case" host in which Sm^{2+} ions shows both 5d→4f and 4f→4f emission. The long decay time of 4f→4f emission makes a scintillation pulse height spectrum measurement virtually impossible, and BaBrI:5%Eu,0.5%Sm can not be used as a scintillator in γ-ray spectroscopy. The energy transfer in BaBrI:5%Eu,0.5%Sm has low efficiency of 11%, and for obtaining higher efficiency it requires optimization of dopant concentrations. Although it may not find application in γ spectroscopy, it still may be used e.g. as a red-emitting X-ray phosphor or luminescence thermometer [28, 29]. The 5d→4f emission of Sm^{2+} goes to one of the seven ^7F_J, J=0-6, final states which reduces self-absorption as compared to Eu^{2+}. It was found that most of X-ray excited emission comes

Table 6.2: Candidate scintillators for applying the $Eu^{2+} \rightarrow Sm^{2+}$ energy transfer mechanism for NIR scintillation. L.Y. – light yield of Eu^{2+} doped material at 662 keV of γ-photon excitation, R – energy resolution at 662 keV, $\tau_{Eu^{2+}}$ – decay time of Eu^{2+} scintillation, $\lambda^{em.}_{Sm^{2+}}$ – 5d-4f emission of Sm^{2+} predicted with Eq. 6.6, $\lambda^{em.}_{Sm^{2+}}$ – 5d-4f Sm^{2+} emission measured, references.

Compound	L.Y. (kPh/MeV)	R (% FWHM)	$\tau_{Eu^{2+}}$ (ns)	$\lambda^{em.}_{Eu^{2+}}$ (nm)	Ref. Eu^{2+} (nm)	$\lambda^{em.}_{Sm^{2+}}$ pred. (nm)	$\lambda^{em.}_{Sm^{2+}}$ meas.
KSr_2I_5:Eu	94	2.4	990	445	[26]	792	–
K_2BaI_4:Eu	57	2.7	720	448	[26]	801	–
KSr_2Br_5:Eu	75	3.5	1080	427	[26]	736	–
KBa_2I_5:Eu	87	2.6	910	444	[26]	788	–
$CsBa_2I_5$:Eu	80-102	2.3-2.55	1000	432	[12, 13]	751	758 (Chapter 5)
SrI_2:Eu	100	2.6	1000	431	[11]	748	753 [25]
BaBrI:Eu	97	3.4	432	413	[12]	696	701 (Chapter 6)
$CsSrI_3$	65	5.9	3300	454	[27]	820	839 (Chapter 7)

from samarium, despite its low concentration and inefficient energy transfer from europium to samarium. This is one of the first experimental cases which shows that different dopants have significantly different cross sections for electron-hole capture from X-ray excited ionization.

REFERENCES

[1] P. A. Rodnyi, *Physical processes in inorganic scintillators*, Vol. 14 (CRC press, 1997).

[2] G. F. Knoll, *Radiation detection and measurement* (John Wiley & Sons, 2010).

[3] P. Lecoq, A. Gektin, and M. Korzhik, *Inorganic scintillators for detector systems: physical principles and crystal engineering* (Springer, 2016).

[4] J. Glodo, Y. Wang, R. Shawgo, C. Brecher, R. H. Hawrami, J. Tower, and K. S. Shah, *New developments in scintillators for security applications,* Physics Procedia **90**, 285 (2017), conference on the Application of Accelerators in Research and Industry, CAARI 2016, 30 October – 4 November 2016, Ft. Worth, TX, USA.

[5] P. Lecoq, *Development of new scintillators for medical applications,* Nuclear Instruments and Methods in Physics Research Section A: Accelerators, Spectrometers, Detectors and Associated Equipment **809**, 130 (2016), advances in detectors and applications for medicine.

[6] I. Mitrofanov, A. Kozyrev, A. Konovalov, M. Litvak, A. Malakhov, M. Mokrousov, A. Sanin, V. Tret'ykov, A. Vostrukhin, Y. Bobrovnitskij, T. Tomilina, L. Gurvits, and A. Owens, *The Mercury Gamma and Neutron Spectrometer (MGNS) on board the Planetary Orbiter of the BepiColombo mission,* Planetary and Space Science **58**, 116 (2010), comprehensive Science Investigations of Mercury: The scientific goals of the joint ESA/JAXA mission BepiColombo.

[7] C. C. Hansson, A. Owens, and J. v.d. Biezen, *X-ray, γ-ray and neutron detector development for future space instrumentation,* Acta Astronautica **93**, 121 (2014).

[8] A. Kozyrev, I. Mitrofanov, A. Owens, F. Quarati, J. Benkhoff, B. Bakhtin, F. Fedosov, D. Golovin, M. Litvak, A. Malakhov, M. Mokrousov, I. Nuzhdin, A. Sanin, V. Tretyakov, A. Vostrukhin, G. Timoshenko, V. Shvetsov, C. Granja, T. Slavicek, and S. Pospisil, *A comparative study of* $LaBr_3(Ce^{3+})$ *and* $CeBr_3$ *based gamma-ray spectrometers for planetary remote sensing applications,* Review of Scientific Instruments **87**, 085112 (2016), https://doi.org/10.1063/1.4958897 .

[9] P. Lecoq, *The high energy physics demand for a new generation of scintillators,* Journal of Luminescence **60-61**, 948 (1994).

[10] R. Mao, L. Zhang, and R. Zhu, *Optical and scintillation properties of inorganic scintillators in high energy physics,* IEEE Transactions on Nuclear Science **55**, 2425 (2008).

[11] M. S. Alekhin, J. T. M. de Haas, K. W. Krämer, I. V. Khodyuk, L. de Vries, and P. Dorenbos, *Scintillation properties and self absorption in* $SrI_2:Eu^{2+}$, in *IEEE Nuclear Science Symposuim Medical Imaging Conference* (2010) pp. 1589–1599.

[12] G. Bizarri, E. D. Bourret-Courchesne, Z. Yan, and S. E. Derenzo, *Scintillation and optical properties of* $BaBrI:Eu^{2+}$ *and* $CsBa_2I_5:Eu^{2+}$, IEEE Transactions on Nuclear Science **58**, 3403 (2011).

[13] M. S. Alekhin, D. A. Biner, K. W. Krämer, and P. Dorenbos, *Optical and scintillation properties of* $CsBa_2I_5:Eu^{2+}$, Journal of Luminescence **145**, 723 (2014).

[14] C. Dujardin, E. Auffray, E. Bourret-Courchesne, P. Dorenbos, P. Lecoq, M. Nikl, A. N. Vasil'ev, A. Yoshikawa, and R. Y. Zhu, *Needs, trends, and advances in inorganic scintillators,* IEEE Transactions on Nuclear Science **65**, 1977 (2018).

[15] R. Awater, M. Alekhin, D. Biner, K. Krämer, and P. Dorenbos, (2019), , in review.

[16] P. Dorenbos, $f \rightarrow d$ *transition energies of divalent lanthanides in inorganic compounds,* Journal of Physics: Condensed Matter **15**, 575 (2003).

[17] W. Döll and W. Klemm, *Messungen an zwei-und vierwertigen Verbindungen der seltenen Erden. VII. Über die Struktur einiger Dihalogenide,* Zeitschrift für anorganische und allgemeine Chemie **241**, 239 (1939).

[18] D. Wood and W. Kaiser, *Absorption and fluorescence of* Sm^{2+} *in* CaF_2, SrF_2, *and* BaF_2, Physical Review **126**, 2079 (1962).

[19] Z. Kiss and H. Weakliem, *Stark effect of* $4f$ *states and linear crystal field in* $BaClF:Sm^{2+}$, Physical Review Letters **15**, 457 (1965).

[20] T. Förster, *Zwischenmolekulare Energiewanderung und Fluoreszenz,* Annalen der Physik **437**, 55 (1948), https://onlinelibrary.wiley.com/doi/pdf/10.1002/andp.19484370105 .

[21] D. L. Dexter, *A theory of sensitized luminescence in solids,* The Journal of Chemical Physics **21**, 836 (1953), https://doi.org/10.1063/1.1699044 .

[22] B. Henderson and G. F. Imbusch, *Optical spectroscopy of inorganic solids*, Vol. 44 (Oxford University Press, 2006).

[23] M. Karbowiak, P. Solarz, R. Lisiecki, and W. Ryba-Romanowski, *Optical spectra and excited state relaxation dynamics of* Sm^{2+} *ions in* $SrCl_2$*,* $SrBr_2$ *and* SrI_2 *crystals,* Journal of Luminescence **195**, 159 (2018).

[24] P. Larsen, *Lumineszenz zweiwertiger Selten-Erd-Ionen in bromidischen Wirtsgittern*, Ph.D. thesis, Universität zu Köln (2004).

[25] M. S. Alekhin, R. H. Awater, D. A. Biner, K. W. Krämer, J. T. de Haas, and P. Dorenbos, *Luminescence and spectroscopic properties of* Sm^{2+} *and* Er^{3+} *doped* SrI_2, Journal of Luminescence **167**, 347 (2015).

[26] L. M. Stand Stracuzzi, *Discovery and Development of Potassium-Based Metal Halide Scintillators for Radiation Detection Applications*, Ph.D. thesis, University of Tennessee, Knoxville (2018).

[27] K. Yang, M. Zhuravleva, and C. L. Melcher, *Crystal growth and characterization of* $CsSr_{1-x}Eu_xI_3$ *high light yield scintillators,* physica status solidi (RRL) – Rapid Research Letters **5**, 43 (2011), https://onlinelibrary.wiley.com/doi/pdf/10.1002/pssr.201004434 .

[28] M. Dramicanin, *Luminescence Thermometry: Methods, Materials, and Applications* (Elsevier, 2018).

[29] C. D. S. Brites, S. Balabhadra, and L. D. Carlos, *Lanthanide-based thermometers: At the cutting-edge of luminescence thermometry,* Advanced Optical Materials **0**, 1801239 (2018), https://onlinelibrary.wiley.com/doi/pdf/10.1002/adom.201801239 .

7

EXPLORING PROPERTIES OF NEW HALIDE SCINTILLATORS WITH EFFICIENT $\mathrm{Eu}^{2+}\rightarrow\mathrm{Sm}^{2+}$ ENERGY TRANSFER AND NEAR-INFRARED EMISSION

> *It is most important in creative science not to give up. If you are an optimist you will be willing to "try" more than if you are a pessimist.*
>
> Stanisław Ulam

In the previous chapter we discussed requirements for obtaining a spin-allowed 5d-4f emission of Sm^{2+}*. We proposed a list of potential candidates for efficient energy transfer between* Eu^{2+} *and* Sm^{2+}*. Here we will investigate deeper the optical and scintillation properties of* $CsBa_2I_5$:0.5%Sm^{2+}, $CsBa_2I_5$:1%Sm^{2+}, $CsBa_2I_5$:2%Eu^{2+},1%Sm^{2+}, $CsBa_2I_5$:4%Eu^{2+},1%Sm^{2+}*, and* $CsSrI_3$:2%Eu^{2+},1%Sm^{2+}*. We have found that among the studied samples the* $CsBa_2I_5$:2%Eu^{2+},1%Sm^{2+} *sample offers the best scintillation performance. The sample with samarium-only has deteriorated scintillation properties, so we conclude that the presence of europium is crucial for efficient scintillation.*

7.1. INTRODUCTION

Most of scintillation research in recent years was focused on developing cerium and europium doped compounds. This strategy resulted in many excellent materials with high energy resolution reaching 2% at 662 keV gamma excitation for $LaBr_3$:Ce,Sr (see Fig. 1.4 in Chapter 1). This was possible due to better understanding of energy loss processes in scintillators and discovering new materials with improved proportionality ($LaBr_3$:Ce, $LaBr_3$:Ce,Sr, $CeBr_3$, SrI_2:Eu, etc.). However, to discover new materials with even better energy resolution, a few requirements have to be met at the same time. The ultimate scintillator should be not only highly-proportional at high density of excitation, but has to offer high light-output, and very efficient detection of scintillation light. As discussed in Chapter 5, silicon photo-detectors like Avalanche Photodiodes (APD) can provide almost 100% efficient detection, but in the red and near-infrared (NIR) spectral range. Currently, there is no commercial scintillator which is suitable for this sensitivity range. In Chapter 5 we proposed the solution for this problem by applying non-radiative energy transfer between europium and samarium. In Chapter 6 we investigated the requirements for obtaining fast, spin-allowed 5d-4f emission of Sm^{2+}. Here we will characterize the scintillation and optical properties of the materials proposed in Chapter 6 as possible candidates.

7.2. SAMPLE PREPARATION AND CRYSTAL GROWTH

$CsSrI_3$:Eu^{2+},Sm^{2+} was synthesized from stoichiometric amounts of the binary halides CsI, SrI_2, EuI_2, and SmI_2. CsI (Merck, suprapur) was dried in vacuum at 250°C. SrI_2 was synthesized from $SrCO_3$ (Alfa Aesar, 4N4) by dissolving in hydroiodic acid (Merck, suprapur 57%). The product was dried up on a sandbath, heated to 450°C in vacuum ($< 10^{-3}$ mbar), and purified by Bridgman crystal growth in a glassy carbon ampoule. EuI_2 was synthesized from Eu metal (Stanford materials, 4N) and iodine (Merck, p.a.). The starting materials were sealed in a silica ampoule under vacuum. The ampoule was heated in a tube furnace keeping the colder end at about 100°C to avoid an overpressure. The metal was slowly heated and kept at 500°C until the iodine had reacted. EuI_2 was sublimed for purification in a tantalum ampoule under vacuum at 1000°C. SmI_3 was prepared in a similar way from Sm metal (Alfa, 3N). The ampoule was heated to 400°C and SmI_3 was sublimed at 800°C in a silica ampoule. SmI_2 was obtained by reacting SmI_3 with Sm in a tantalum ampoule at 900°C for 2 days. The tantalum ampoule was sealed by He-arc welding and encapsulated into a silica ampoule under vacuum.

Crystals of $CsSrI_3$:Eu,Sm were grown by the Bridgman technique using a vertical, static ampoule with seed selection tip and a moving furnace. The starting materials were sealed in a silica ampoule under vacuum and heated to 660°C for 1 day. $CsSrI_3$ melts congruently at 650°C. Then the furnace was slowly moved up by a controlled stepper motor with 0.6 mm/hour cooling the crystal to room temperature within about 10 days. The ampoules were opened in a glove box (MBraun, Graching, D) equipped with a microscope and with water and oxygen values < 0.1 ppm. Crystals were cleaved from the boule and pieces of about 5 mm size were sealed in small silica ampoules for further spectroscopic characterization. The phase purity of the product was verified by powder X-ray diffraction on a Stoe Stadip diffractometer in Bragg-Brentano (reflection) geometry with CuKa1 radiation from a curved (101) a-SiO_2 monochromator and a linear position sensitive detector. $CsSrI_3$ crystallizes in the stuffed $PuBr_3$ structure (orthorhombic, Cmcm, no. 63) [1]. Since starting materials and products are hygroscopic all handling was done under strictly dry conditions in glove boxes or sealed containers.

The synthesis and crystal growth of $CsBa_2I_5$:Eu,Sm and BaBrI:Eu,Sm samples have been described previously in Chapters 5 and 6, correspondingly.

7.3. EXPERIMENTAL METHODS

Optically excited luminescence spectra were measured with an FL-1039 Horiba 450 W xenon lamp combined with a Gemini-180 Horiba double-grating monochromator. The emission from the sample was dispersed with an Acton SP2300 Princeton Instruments monochromator and detected with a Hamamatsu R7600U-20 (300-920 nm) or R7600U-03 (185-650 nm) photomultiplier tube (PMT), or a Hamamatsu C9100-13 electron multiplier CCD camera.

X-ray excited luminescence spectra were recorded using an X-ray tube with tungstate anode. The emission from the sample was dispersed with an ARC VM504 monochromator and recorded with a Hamamatsu R493-02 PMT. The emission was not corrected for the monochromator transmission nor quantum efficiency of the PMT.

The scintillation decay time profiles were measured with the time-correlated single photon counting (TCSPC) method [2]. The setup consists of a PicoQuant LDH-P-C-440M pulsed diode laser, a Hamamatsu N5084 light-excited x-ray tube, and an ID Quantique id100-50 single-photon counter. The laser driver was triggered from a 8116A Hewlett Packard function generator. The driver's reference output was connected to the start input of an Ortec 567 time-to-amplitude converter (TAC), while the photon counter was connected to the stop input. An Ortec AD114 amplitude-to-digital converter was used to digitize and collect the start-stop time differences. An Ortec 462 time calibrator was used to determine the TAC bin width.

γ-ray excited Pulse Height Spectra (PHS) were recorded with an Advanced Photonix Avalanche Photo-diode (APD) 630-70-72-510 or Photonis XP2254B photomultiplier tube (PMT), connected to a Cremat CR-112 pre-amplifier, and an Ortec 672 spectroscopic amplifier with 10 μs shaping time. The sample was mounted in a pressed-Teflon holder, and placed 0.1 mm from the surface of the APD. The APD temperature was stabilized at T = 270 K by a two stage Peltier device and a LakeShore temperature controller. The APD bias voltage was +1690V. The crystals were mounted without any optical coupling, and the APD was used without any protective entrance window. More details about the APD setup can be found in [3].

7.4. RESULTS

7.4.1. OPTICAL SPECTROSCOPY OF Sm^{2+}

Fig. 7.1 shows photoluminescence emission spectra of $CsSrI_3$:2%Eu^{2+},1%Sm^{2+}, BaBrI:5%Eu^{2+},0.5%Sm^{2+}, and $CsBa_2I_5$:2%Eu^{2+},1%Sm^{2+} measured at room temperature. The wavelength ranges of typical Eu^{2+} and Sm^{2+} emission are marked at the top. The Eu^{2+} emission is characterized by a single broad peak ascribed to the spin allowed 5d-4f transition. The Eu^{2+} peak shifts to red with change of the host in the sequence from BaBrI (417 nm), $CsBa_2I_5$ (430 nm), to $CsSrI_3$ (454 nm). Similar red-shift is observed for Sm^{2+} emission, however, the Sm^{2+} emission in BaBrI is more complex, and it is characterized by presence of five sharp 4f-4f transition lines and a weak broad 5d-4f emission

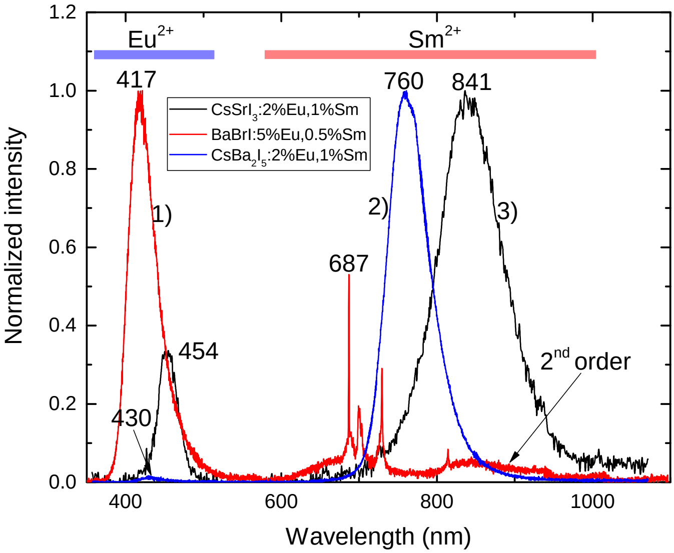

Figure 7.1: Room temperature emission spectra of 1) BaBrI:5%Eu^{2+},0.5%Sm^{2+} ($\lambda_{exc.}$ = 350 nm), 2) $CsBa_2I_5$:2%Eu^{2+},1%Sm^{2+} ($\lambda_{exc.}$ = 360 nm), and 3) $CsSrI_3$:2%Eu^{2+},1%Sm^{2+} ($\lambda_{exc.}$ = 360 nm) excited with a xenon lamp and measured with a 300 nm blazed monochromator coupled to a CCD detector. The spectra are not corrected for the monochromator and detector efficiencies.

at around 700 nm. The band between 800 and 1000 nm in BaBrI sample is from second order transmission of the monochromator.

Fig. 7.2 shows excitation and emission spectra of $CsBa_2I_5$:0.5%Sm^{2+} crystal measured at room and 10 K temperature. The emission spectrum is almost identical as that of $CsBa_2I_5$:2%Eu^{2+},1%Sm^{2+} in Fig. 7.1, but then without Eu^{2+} emission. The excitation spectrum measured at room temperature (Fig. 7.2a) has multiple Sm^{2+} excitation bands extending from 300 nm to 750 nm. The lowest energy excitation peak is at 693 nm. The emission spectrum changes dramatically at 10 K. Five sharp emission lines appear, that can be identified as 4f-4f transitions from $^5D_0$ Sm^{2+} level to the ground state manifold $^7F_0$ (688 nm), $^7F_1$ (703 nm), $^7F_2$ (729 nm), $^7F_3$ (767 nm), and $^7F_4$ (817 nm). The width of the 5d-4f emission peak decreases at 10 K and a sub-structure becomes visible: a main 750 nm peak, and an additional shoulder at ~825 nm.

Fig. 7.3 shows photoluminescence emission and excitation spectra of $CsBa_2I_5$:2%Eu^{2+},1%Sm^{2+} at room temperature. A single emission peak is observed at 762 nm. The excitation spectrum is similar to the excitation spectrum of $CsBa_2I_5$:0.5%Sm^{2+}. However, the higher Sm^{2+} concentration causes optical saturation and affects the intensity. The most dominating features of the excitation spectrum is a peak at 704 nm and broad band between 500 and 650 nm. Despite presence of Eu^{2+}, the excitation intensity is not enhanced in the range between 300 and 400 nm when compared with Fig. 7.2a.

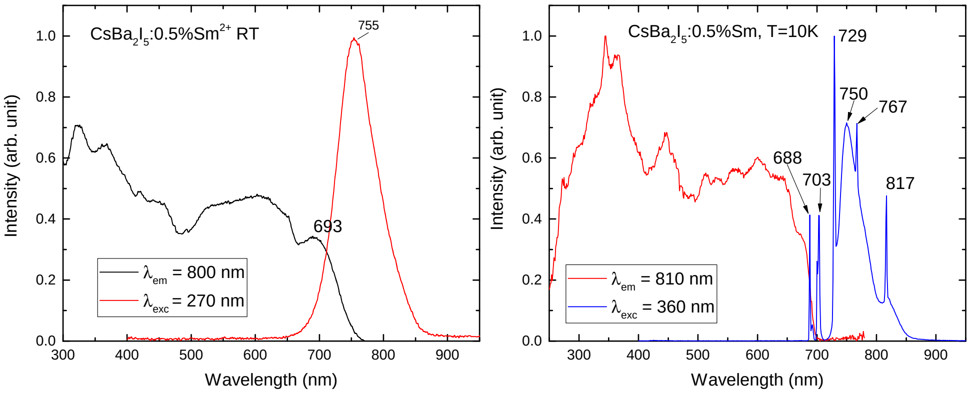

(a)

(b)

Figure 7.2: Photoluminescence emission and excitation spectra of CsBa$_2$I$_5$:0.5%Sm^{2+} a) at room temperature and b) at 10 K measured with a xenon lamp excitation and a Hamamatsu R7600U-20 photomultiplier.

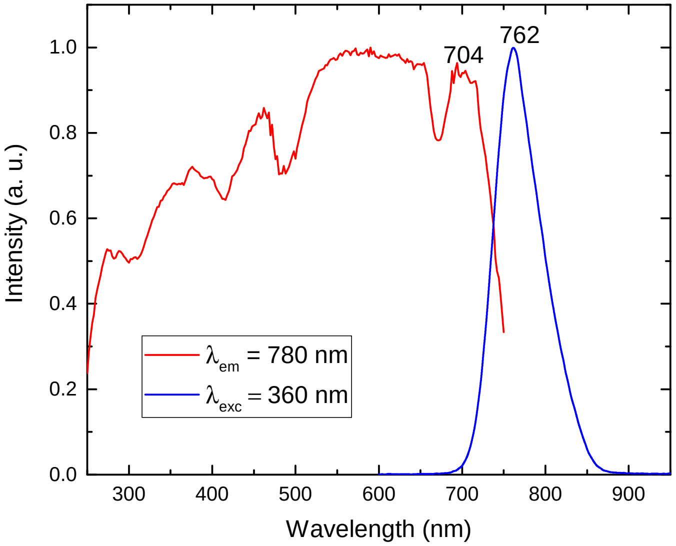

Figure 7.3: Photoluminescence emission and excitation spectra of CsBa$_2$I$_5$:2%Eu^{2+},1%Sm^{2+} at room temperature measured with a xenon lamp excitation and a Hamamatsu R7600U-20 photomultiplier.

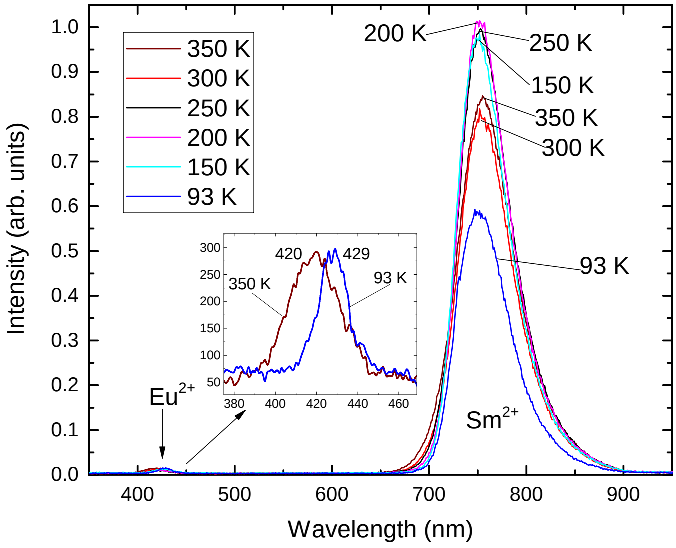

Figure 7.4: X-ray excited emission spectra of $CsBa_2I_5$:2%Eu^{2+},1%Sm^{2+} crystal as a function of temperature. The inset shows enlarged range of 370-480 nm.

7.4.2. X-RAY EXCITED EMISSION

Fig. 7.4 shows the X-ray excited emission of $CsBa_2I_5$:2%Eu^{2+},1%Sm^{2+} crystal measured between 93 K and 350 K. The broad Sm^{2+} 5d-4f emission peak dominates at 755 nm at all temperatures. It has the highest intensity at 150-250 K, the lowest at 93 K, and moderate at 300-350 K. The peak's shape and position does not change significantly. Very weak Eu^{2+} 5d-4f emission is observed around 420-430 nm. The inset shows the enlarged Eu^{2+} peak, which contains ~0.5% of the total integrated intensity. It broadens with increasing temperature and shifts to shorter wavelengths.

7.4.3. LIGHT YIELD AND ENERGY RESOLUTION

Fig. 7.5a shows pulse height spectra of a ^{137}Cs isotope measured with $CsBa_2I_5$:2%Eu^{2+},1%Sm^{2+} and $CsBa_2I_5$:1%Sm^{2+} using an APD. The energy resolution of the 662 keV full absorption peak is 4.5% in Sm doped sample, and 3.2% in the Eu,Sm doped sample. This suggests that the presence of europium plays a role in the scintillation process and leads to higher energy resolution.

Tab. 7.1 compiles the data on light yield and energy resolution of the studied crystals. The table shows energy resolution and light yield ranges obtained with the best and the worse sample cut from each studied boule. $CsBa_2I_5$:0.5%Sm^{2+} crystals showed high variability of the light yield and energy resolution between different samples with the same nominal composition. This is probably because of high non-uniformity of Sm^{2+} doping at low concentration of samarium in the starting melt. Some of $CsSrI_3$:2%Eu^{2+},1%Sm^{2+} samples did not have well defined pulse-height spectra at all, while others showed double photo-peak. It is possibly caused by high difficulty to growth a single-phase $CsSrI_3$ perovskite crystals. Interestingly, the addition of europium to $CsBa_2I_5$:1%Sm^{2+} does not

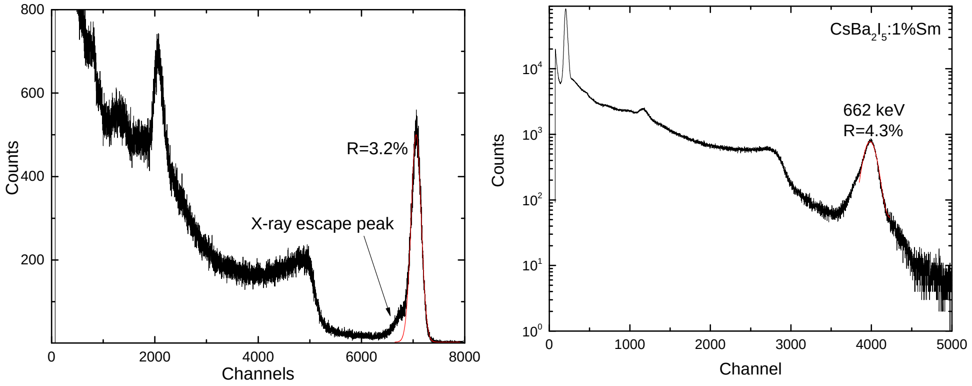

(a) $CsBa_2I_5$:2%Eu^{2+},1%Sm^{2+} (b) $CsBa_2I_5$:1%Sm^{2+}

Figure 7.5: Pulse height spectra of ^{137}Cs measured with a.) $CsBa_2I_5$:2%Eu^{2+},1%Sm^{2+} and b.) $CsBa_2I_5$:1%Sm^{2+} single crystals coupled to an APD.

change the light yield significantly, while it improves energy resolution. On the other hand, the increased europium concentration in $CsBa_2I_5$:4%Eu^{2+},1%Sm^{2+} deteriorates energy resolution when compared to $CsBa_2I_5$:2%Eu^{2+},1%Sm^{2+}, but it does not affect the light yield significantly.

Fig. 7.6 shows the light yield and energy resolution of $CsBa_2I_5$:2%Eu^{2+},1%Sm^{2+} crystal encapsulated in a quartz ampule and coupled to a XP2254B PMT. Both, the light output and energy resolution increase with increasing shaping time. This suggests rather long scintillation time. The energy resolution is much lower than measured with an APD, and it is well expected as the data sheet of the PMT reports ~1% quantum efficiency at 750 nm of $CsBa_2I_5$:2%Eu^{2+},1%Sm^{2+} emission. Obviously, $CsBa_2I_5$:2%Eu^{2+},1%Sm^{2+} is not a scintillator suited for a read-out with a traditional PMT, and the energy resolution is highly limited by the detection efficiency in that case.

Table 7.1: Light yield and energy resolution of the studied samples.

Sample	Light yield (phe/MeV)	Energy resolution (% at 662 keV)
$CsBa_2I_5$:0.5%Sm^{2+}	20.4-38.5	14.8-56.0
$CsBa_2I_5$:1%Sm^{2+}	47.8	4.3
$CsBa_2I_5$:2%Eu^{2+},1%Sm^{2+}	41.5-45.8	3.2-3.9
$CsBa_2I_5$:4%Eu^{2+},1%Sm^{2+}	38.2-51.6	4.5-6.3
$CsSrI_3$:2%Eu^{2+},1%Sm^{2+}	19.9-20.3	9.7-12.8

7.4.4. DECAY TIME

Fig. 7.7a shows the X-ray excited luminescence decay time of $CsBa_2I_5$:2%Eu^{2+},1%Sm^{2+} crystal at 300 K. The decay profile was fit with a double-exponential function. The dominant decay component is 2.1 μs and corresponds to 94% of the total scintillation light

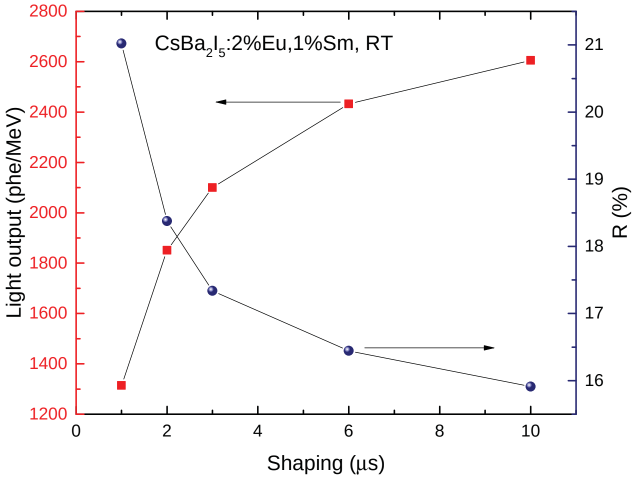

Figure 7.6: ^{137}Cs pulse height spectrum measured with $CsBa_2I_5$:2%Eu^{2+},1%Sm^{2+} crystal encapsulated in a quartz ampule and coupled to a XP2254B PMT.

intensity, while the fast component of 240 ns consists only 6% of the total. The long main component requires an appropriate integration/shaping time for efficient collection of all scintillation light, which was already seen in Fig. 7.6.

Since europium emission (430 nm) in $CsBa_2I_5$:2%Eu^{2+},1%Sm^{2+} is well separated in wavelength from samarium emission (760 nm, see Fig. 7.4), it is easily possible to separately measure europium scintillation decay with an optical band-pass filter. Fig. 7.7b shows Eu^{2+} scintillation decay in the $CsBa_2I_5$:2%Eu^{2+},1%Sm^{2+} crystal at 300 K measured with a 420 nm band-pass filter. The decay profile was fit with a double-exponential function. The most of light (72.8%) is emitted with 136.6 ns decay time. We conclude, that the europium emission is largely responsible for the fast 240 ns component observed in the total scintillation decay profile, Fig. 7.7a.

Fig. 7.8a shows X-ray excited luminescence decay profiles as a function of temperature. The decay time shortens with decrease of temperature. Fig. 7.8b shows the slow decay component (the dominant scintillation component) as a function of temperature. It decreases almost linearly between 400 and 100 K. The decay time slightly increases at 79 K when compared to the value at 100 K, and it can be explained by arising forbidden 4f-4f emission observed previously at 10 K, see Fig. 7.2b.

7.4.5. THE α/β RATIO

Fig. 7.9a shows the internal contamination spectrum of the $CsBa_2I_5$:2%Eu^{2+},1%Sm^{2+} crystal measured with an APD and a ^{137}Cs source placed in the vicinity of the detector for energy reference. An exponential slope between 700 keV and 2000 keV comes from direct detection of Compton-scattered 662 keV gamma photons in the APD. The peak observed at around 1 MeV of gamma-equivalent energy originates from the direct detection of X-ray fluorescence photons in the APD. The four peaks at 2450 keV, 2909 keV, 3241 keV, and 4415 keV of gamma-equivalent energy can be identified as internal alpha decays.

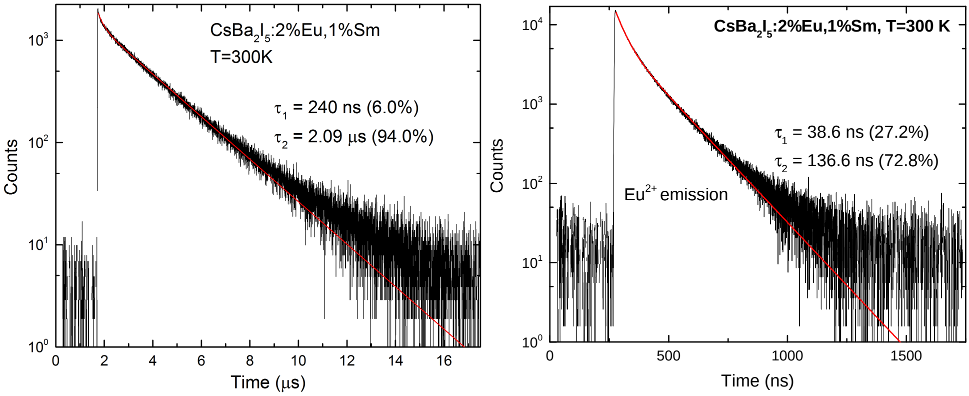

(a) (b)

Figure 7.7: a.) X-ray excited luminescence of CsBa$_2$I$_5$:2%Eu^{2+},1%Sm^{2+} crystal at 300 K (total emission) b.) with 420 nm optical band-pass filter (Eu^{2+} emission only).

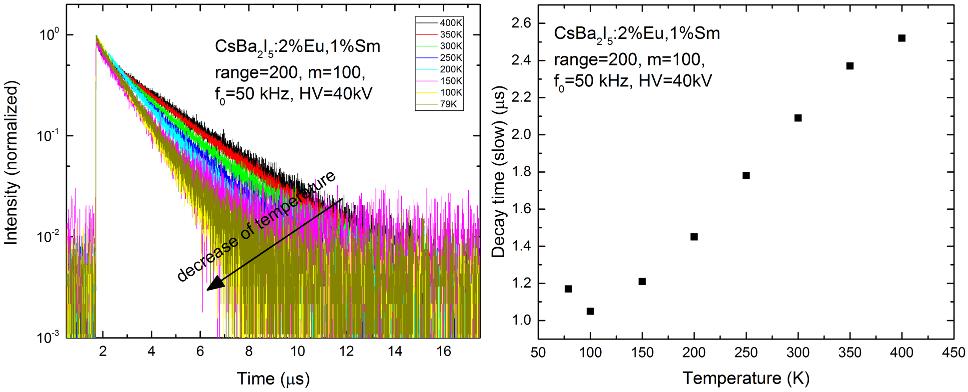

(a) (b)

Figure 7.8: X-ray excited luminescence of CsBa$_2$I$_5$:2%Eu^{2+},1%Sm^{2+} as a function of temperature. a.) luminescence decay profiles b.) decay time of the dominant (slow) component.

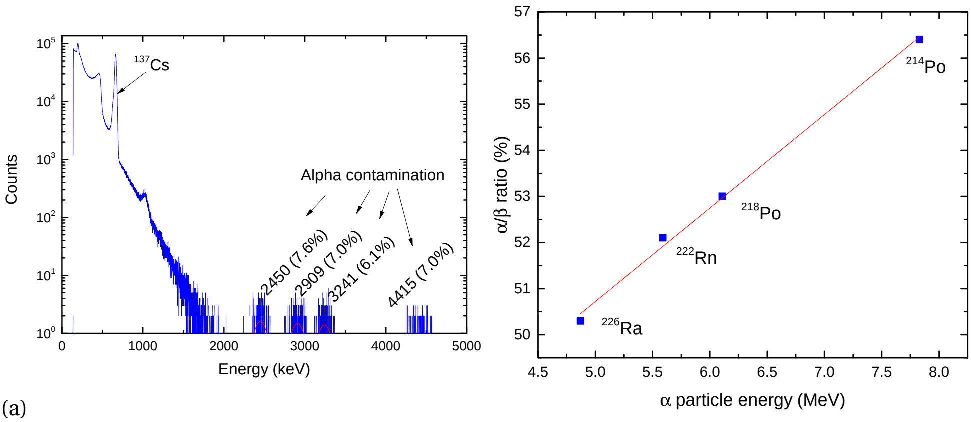

(a)

(b)

Figure 7.9: a.) Internal contamination pulse height spectrum with a ^{137}Cs reference in $CsBa_2I_5$:2%Eu^{2+},1%Sm^{2+} sample b.) The α/β ratio of $CsBa_2I_5$:2%Eu^{2+},1%Sm^{2+} as a function of alpha particle energy.

No gamma background is observed at this energy range as the sample size of around ~2-3 mm is too small for efficient detection of high energy gamma photons. The energy resolution with alpha particles is shown in parentheses, and it ranges from 6.1% to 7.6%. The alpha peaks were identified as ^{226}Ra (2450 keV), ^{222}Rn (2909 keV), ^{218}Po (3241 keV), and ^{214}Po (4415 keV) based on analogue identification in BaF_2, see Chapter 2. ^{226}Ra and ^{228}Th contamination are common in barium-based scintillators, and the decays of the daughter isotopes are responsible for the internal contamination [4]. Fig. 7.9b shows the α/β ratio measured with the identified impurity isotopes. As it was discussed in Chapter 2, the α/β ratio can be used for characterization of high density quenching of scintillators, and the high value of 50-56% indicates high proportionality of the material. Fig. 2.7 in Chapter 2 showed intrinsic energy resolution of multiple scintillators versus the alpha/beta ration. The alpha/beta ration of ~50% in $CsBa_2I_5$:2%Eu^{2+},1%Sm^{2+} is very close to the value for $LaBr_3$:Ce,Sr, so we conclude that the $CsBa_2I_5$:Eu,Sm scintillator have very good proportionality and intrisic energy resolution around 1%.

7.5. DISCUSSION

Almost all X-ray excited luminescence in $CsBa_2I_5$:2%Eu^{2+},1%Sm^{2+} comes from Sm^{2+}, so either the energy transfer from europium to samarium is very efficient or samarium can capture electrons and holes with much higher efficiency than europium, see Chapter 6.5.1. The weak Eu^{2+} peak in $CsBa_2I_5$:2%Eu^{2+},1%Sm^{2+} showed very similar behavior to that observed previously for a much lower concentration sample in $CsBa_2I_5$:0.5%Eu^{2+} [5]: it shifts towards short-wavelengths with increasing temperature (Fig. 7.4). This indicates that self-absorption by Eu^{2+} has been minimized in the Sm co-doped sample. However, the decay time change with temperature of $CsBa_2I_5$:2%Eu^{2+},1%Sm^{2+} (Fig. 7.8b) increases with temperature which can be caused by increased self-absorption of samarium at higher temperatures. Indeed, Fig. 7.3 shows increased broadening and overlap of excitation and emission spectra of samarium at room temperature compared to 10 K. Increasing overlap with increasing temperature leads to higher probability of self-absorption and explains lengthening of the decay time at higher temperatures. On the other hand, it is quite unexpected to observe strong self-absorption in such small samples like used in this study (2-3 mm). More studies are required to find the origin of decay time lengthening.

A single Eu^{2+} peak was observed in $CsBa_2I_5$:2%Eu^{2+},1%Sm^{2+} at 420 nm (350 K), and at 429 nm (93 K). The same position was reported previously by Alekhin et al. [5] and Shirwadkar et al. [6]. Bizzari et al. [7] has reported a double Eu^{2+} peak at 432 and 465nm, which was attributed to occupation of two different barium sites. Two crystallographically inequivalent sites exist in $CsBa_2I_5$ for the barium ions: one of them coordinated by seven iodides and the second coordinated by eight iodides [8]. This possibility was further investigated in [9], and the authors concluded that Eu favors the barium seven-coordination sites and shows a tendency towards forming Eu-rich domains (clusters). In our work we did not observe double Eu^{2+} peak, and we conclude that Eu in $CsBa_2I_5$:2%Eu^{2+},1%Sm^{2+} occupies only one coordination site. Possibly, the double peak observed by Bizzari at al. can be explained by growth conditions and Eu clustering.

Fig. 7.8a shows X-ray excited scintillation decay in $CsBa_2I_5$:2%Eu^{2+},1%Sm^{2+}. A fast component of 240 ns is probably caused by time and distance dependent energy transfer from europium to samarium. The double-exponential decay was not observed in the BaBrI:5%Eu,0.5%Sm sample studied previously in Chapter 6, see Fig. 6.6. This single-exponential decay justified applying the simple linear model previously presented for BaBrI:5%Eu,0.5%Sm in Section 6.5.1. Increased samarium concentration in $CsBa_2I_5$:2%Eu^{2+},1%Sm^{2+} can be responsible for the increased efficiency of the energy transfer and as result a double-exponential decay. We can estimate the efficiency of energy transfer from Eu to Sm in $CsBa_2I_5$:2%Eu^{2+},1%Sm^{2+} with the simple formula presented in Section 6.5.1: $\epsilon = 1 - \frac{1}{k_1 \cdot \tau_{(Eu^{2+})^*}}$, europium decay time in presence of samarium is taken as the main decay component at Fig. 7.7b and the europium decay time without samarium is 360 ns at 295 K in $CsBa_2I_5$ with a small trace impurity of europium (measured by [5]). Then, the efficiency is $\epsilon = 1 - \frac{136.6}{360} \approx 62\%$. It is much higher value than in BaBrI:5%Eu,0.5%Sm, and in $CsBa_2I_5$:2%Eu^{2+},1%Sm^{2+} most of samarium excitation originates from non-radiative energy transfer from europium, not direct hole-electron capture like in BaBrI:5%Eu,0.5%Sm. However, more detailed analysis of energy transfer process requires additional experimental data, preferably measured at multiple concentrations of both dopants.

The scintillation decay time of 2.1 μs in $CsBa_2I_5$:2%Eu^{2+},1%Sm^{2+} is not suitable for high count rate applications, but it is still acceptable for many γ-spectroscopy applications. The energy resolution of 3.2% obtained with $CsBa_2I_5$:2%Eu^{2+},1%Sm^{2+} places it in the range of high-resolution scintillators. For the first time it is possible with a near-infrared emission, which enables high detection efficiency with a silicon detector. However, it is not clear yet if this high resolution is caused by presence of europium and efficient energy transfer to samarium, or maybe samarium alone is a good electron-hole capturing center. This requires more experimental data and a study of a larger parameter space.

7.6. CONCLUSIONS

In this chapter we presented the scintillation properties of the recently discovered $CsBa_2I_5$:2%Eu^{2+},1%Sm^{2+} scintillator. It exploits the energy transfer mechanism from Eu to Sm for shifting the emission into near-infrared spectral range. It has good performance compared to the previously reported values, and is one of the first scintillators with such a high energy resolution of 3.2% and NIR emission. The light yield of 46,000 ph/MeV of absorbed 662 keV gamma-ray energy was measured and makes it a moderate-bright scintillator. It was shown that the presence of europium plays a role in scintillation mechanism as the energy resolution of Sm-only sample was lower (4.3%). However, this can be also explained by high variability of energy resolution in different samples with the same composition. The performance of the Eu and Sm doped perovskite sample $CsSrI_3$:2%Eu^{2+},1%Sm^{2+} was much worse. It has much lower efficiency of energy transfer and worse scintillation properties.

7.7. ACKNOWLEDGMENTS

The authors thank D. Biner (Bern) for the sample synthesis. This work was supported by the Dutch Technology Foundation STW, which is part of the Netherlands Organization for Scientific Research (NWO), which is partly funded by the Ministry of Economic Affairs. This work was partly funded by Saint Gobain Crystals, France.

REFERENCES

[1] G. Schilling and G. Meyer, *Ternäre Bromide und Iodide zweiwertiger Lanthanide und ihre Erdalkali-Analoga vom Typ* AMX_3 *und* AM_2X_5, Zeitschrift für anorganische und allgemeine Chemie **622**, 759 (1996), https://onlinelibrary.wiley.com/doi/pdf/10.1002/zaac.19966220502 .

[2] D. N. ter Weele, D. R. Schaart, and P. Dorenbos, *Intrinsic scintillation pulse shape measurements by means of picosecond x-ray excitation for fast timing applications,* Nuclear Instruments and Methods in Physics Research Section A: Accelerators, Spectrometers, Detectors and Associated Equipment **767**, 206 (2014).

[3] J. T. M. de Haas and P. Dorenbos, *Advances in yield calibration of scintillators,* IEEE Transactions on Nuclear Science **55**, 1086 (2008).

[4] P. Belli, R. Bernabei, F. Cappella, V. Caracciolo, R. Cerulli, F. A. Danevich, A. Di Marco, A. Incicchitti, D. V. Poda, O. G. Polischuk, and V. I. Tretyak, *Investigation of rare nuclear decays with* BaF_2 *crystal scintillator contaminated by radium,* The European Physical Journal A **50**, 134 (2014).

[5] M. S. Alekhin, D. A. Biner, K. W. Krämer, and P. Dorenbos, *Optical and scintillation properties of* $CsBa_2I_5$*:*Eu^{2+}, Journal of Luminescence **145**, 723 (2014).

[6] U. Shirwadkar, R. Hawrami, J. Glodo, E. V. D. van Loef, and K. S. Shah, *Promising alkaline earth halide scintillators for gamma-ray spectroscopy,* IEEE Transactions on Nuclear Science **60**, 1011 (2013).

[7] G. Bizarri, E. D. Bourret-Courchesne, Z. Yan, and S. E. Derenzo, *Scintillation and optical properties of BaBrI:Eu*$^{2+}$ *and CsBa*$_2$*I*$_5$*:Eu*$^{2+}$, IEEE Transactions on Nuclear Science **58**, 3403 (2011).

[8] E. Bourret-Courchesne, G. Bizarri, R. Borade, Z. Yan, S. Hanrahan, G. Gundiah, A. Chaudhry, A. Canning, and S. Derenzo, *Eu*$^{2+}$*-doped Ba*$_2$*CsI*$_5$*, a new high-performance scintillator,* Nuclear Instruments and Methods in Physics Research Section A: Accelerators, Spectrometers, Detectors and Associated Equipment **612**, 138 (2009).

[9] C. M. Fang and K. Biswas, *Preferential Eu Site Occupation and Its Consequences in the Ternary Luminescent Halides* $AB_2I_5:Eu^{2+}$ *(*$A = Li - Cs$*;* $B = Sr$*, Ba),* Phys. Rev. Applied **4**, 014012 (2015).

8

CONCLUSION

In Chapter 2 we showed that the α/β ratio can be used to characterize scintillators in the same way as electron/gamma non-proportionality at low energy of excitation (~10 keV). In many aspects measurement of the α/β ratio has advantages over other methods. It provides higher precision and higher density of excitation than is available with Compton or photoelectric effect electrons. It has been shown that the α/β ratio follows the same trends and patterns as previously found for nonproportionality of electron/gamma photon response. The α/β ratio also correlates with intrinsic energy resolution measured with 10 keV gamma photons. Materials with high α/β ratio have high intrinsic energy resolution at high density of excitation. The same trend is observed for 662 keV gamma photons with exception of alkali halides and ZnSe:Te. We have found that alkali halides have low intensity of quenching and perform better than $LaBr_3$:Ce and $LaCl_3$:Ce at high density excitation (with α particles or 10 keV electrons). The superiority of $LaBr_3$:Ce and $LaCl_3$:Ce over alkali halides probably comes not from high resistivity to high density quenching, but from lack of a low density quenching which is responsible for the "hump" in an electron/gamma nonproportionality curve. We can conclude, that halide-based scintillators are the most promising for discovering new highly proportional materials.

In Chapter 3 we presented digital spectroscopy as a powerful tool for studying scintillators. It makes possible to perform a complex analysis like a pulse shape discrimination or a time-amplitude analysis. This permitted us to investigate the complex structure of an intrinsic alpha spectrum in $LaBr_3$:Ce, $LaBr_3$:Ce,Sr and $CeBr_3$.

An alpha spectrum measured in a scintillator with an intrinsic contamination can be significantly distorted by gamma de-excitations of decay products. This is because an alpha particle can be detected together with a gamma photon as a single event, but both particles have significantly different light yields. This conclusion is particularly important for correct simulation of an intrinsic alpha activity. In addition, measuring the α/β ratio with an intrinsic alpha contamination seems to be an attractive way of avoiding surface effects, but it can not be easily done with an alpha isotope decaying into an excited state of a daughter nucleus.

By applying time-amplitude cuts on the acquired data, we were able to separate Po-215 and Rn-219 alpha peaks from the total spectrum. With this method, we found asymmetric alpha peaks in $LaBr_3$:Ce and $LaBr_3$:Ce,Sr but not in $CeBr_3$. The cause of this phenomenon is not known. Our approach to include nuclear de-excitation processes in simulation is promising, and together with experimental data on asymmetric α peaks gives a way to construct a complete and accurate simulation of a scintillation response to an intrinsic activity. We advise using the ^{215}Po alpha peak in future α/β ratio measurements, as this peak is made out of pure alpha decays to a ground state, not followed by any other type of de-excitation.

Chapter 4 extends the digital analysis methods for the study of pulse shapes in scintillators. With this method we have found a weak pulse shape dependence on gamma energy for CsI(Tl), and different scintillation decay time for gamma rays and X-ray pulsed excitations. The experimental results are in good agreement with theoretical predictions by Lu et al. [1], but minor differences are observed and require more research.

In Chapter 5 we proposed a new strategy for developing new near-infrared scintillators. By adding Sm^{2+} to $CsBa_2I_5$:Eu^{2+} energy transfer from Eu to Sm results into an efficient 755 nm near infra-red emitting scintillator. The ^{137}Cs pulse height spectrum with 3.2% energy resolution at 662 keV with APD read-out can be considered as the birth certificate of the first black scintillator. There are many other potential iodide compounds where the new research strategy can be applied to, and a realistic evaluation shows that resolution lower than 2% is well-feasible. We also demonstrated 5.4% resolution with a very low cost Si-PM. Such a detector can for example easily be incorporated into miniature portable γ-spectrometers, even in a smartphone type of device, for safety applications.

In Chapter 6 we investigated requirements for obtaining 5d-4f spin-allowed emission of samarium. We have found that BaBrI is a "border-case" host in which Sm^{2+} shows both 5d-4f and 4f-4f emission. The long decay time of 4f-4f emission makes a pulse height spectrum measurement virtually impossible, and BaBrI:5%Eu,0.5%Sm can not be used as a scintillator in γ spectroscopy at room temperature. Also, the energy transfer in BaBrI:5%Eu,0.5%Sm is not complete, and for obtaining high efficiency it requires optimization of dopant concentrations. This compound may not find application in γ spectroscopy but still can be used e.g. as a red-emitting X-ray phosphor or a luminescence thermometer [2, 3]. However, if the 4f5d level can be lowered sufficiently to avoid 4f-4f emission, the 5d-4f emission of Sm^{2+} ends in one of the seven ^7F_J states which is expected to reduce self-absorption as compared to Eu^{2+}.

In Chapter 7 we investigated further the possible candidate hosts for efficient 5d-4f emission of samarium. We have found that within studied compositions the $CsBa_2I_5$:2%Eu^{2+},1%Sm^{2+} sample shows the best scintillation performance and offers 3.2% energy resolution at 662 keV gamma excitation. It has moderate light yield of 46,000 photons/MeV (@662 keV), and 2.1 μs scintillation decay time. The samarium-only doped sample of $CsBa_2I_5$ did not show so good scintillation performance, which proves an essential role of europium in electron-hole capture process from an ionized track.

REFERENCES

[1] X. Lu, S. Gridin, R. T. Williams, M. R. Mayhugh, A. Gektin, A. Syntfeld-Każuch, Ł. Świderski, and M. Moszyński, *Energy-Dependent Scintillation Pulse Shape and Proportionality of Decay Components for CsI:Tl: Modeling with Transport and Rate Equations,* Phys. Rev. Applied **7**, 014007 (2017).

[2] M. Dramicanin, *Luminescence Thermometry: Methods, Materials, and Applications* (Elsevier, 2018).

[3] C. D. S. Brites, S. Balabhadra, and L. D. Carlos, *Lanthanide-based thermometers: At the cutting-edge of luminescence thermometry,* Advanced Optical Materials **7**, 1801239 (2019), https://onlinelibrary.wiley.com/doi/pdf/10.1002/adom.201801239 .

9

SAMENVATTING

In Hoofdstuk 2 hebben we aangetoond dat de α/β-verhouding kan worden gebruikt voor het karakteriseren van scintillatoren op dezelfde manier als laag energetische elektronen kunnen worden gebruikt voor karakterisatie van niet-evenredigheids responsie. In veel opzichten heeft meting van de α/β -verhouding voordelen ten opzichte van andere methoden. Het biedt een hogere precisie en een hogere dichtheid van excitatie dan beschikbaar is met Compton elektronen of elektronen gecreëerd met met het foto-elektrisch effect. Er is aangetoond dat de α/β-verhouding kan worden gebruikt voor het karakteriseren van scintillatiemateriaal. Het volgt dezelfde trends en patronen met betrekking tot niet-evenredigheid als eerder gevonden voor de respons op elektronen/gammafotonen. De α/β -verhouding correleert ook met de intrinsieke energieresolutie gemeten met 10 keV gammafotonen. Materialen met een hoge α/β-verhouding hebben een hoge intrinsieke energieresolutie bij excitatie met hoge energiedichtheid. Dezelfde trend wordt waargenomen voor 662 keV gammafotonen met uitzondering van alkalihalogeniden en ZnSe: Te. We hebben gevonden dat alkalihalogeniden een lage mate van uitdoving hebben en beter presteren dan $LaBr_3$:Ce en $LaCl_3$:Ce bij excitatie met hoge dichtheid (met α-deeltjes of 10 keV-elektronen). De superioriteit van $LaBr_3$:Ce en $LaCl_3$:Ce over alkalihalogeniden komt waarschijnlijk niet doordat deze materialen beter bestand zijn tegen uitdovingsprocessen als ze met een hoge dichtheid geëxciteerd worden, maar juist door het ontbreken van uitdovingsprocessen wanneer het materiaal met een lage dichtheid geëxciteerd wordt, die verantwoordelijk is voor de "bult" in de elektron/gamma niet-evenredigheids responsie. We kunnen concluderen dat op halogenide gebaseerde scintillatoren het meest veelbelovend zijn voor het ontdekken van nieuwe materialen met hoge evenredigheid.

In Hoofdstuk 3 hebben we digitale spectroscopie als een krachtig hulpmiddel voor het bestuderen van scintillatoren gepresenteerd. Het maakt het mogelijk om een complexe analyse uit te voeren zoals het onderscheiden van pulsvormen of een tijd-amplitude analyse. Dit stelde ons in staat om de complexe structuur van een intrinsiek alfaspectrum in $LaBr_3$:Ce, $LaBr_3$:Ce,Sr en $CeBr_3$ te onderzoeken.

Een alfaspectrum gemeten van een scintillator met een intrinsieke verontreiniging kan aanzienlijk worden vervormd door gamma-de-excitaties van vervalproducten. Dit komt omdat een alfadeeltje samen met een gammafoton kan worden gedetecteerd als een enkele gebeurtenis. Beide deeltjes hebben echter aanmerkelijke verschillende lichtopbrengsten. Deze conclusie is vooral belangrijk voor de juiste simulatie van intrinsieke alfa-activiteit. Bovendien lijkt het meten van de α/β-verhouding met een intrinsieke alfa-verontreiniging een aantrekkelijke manier om oppervlakte-effecten te voorkomen, maar het kan niet gemakkelijk worden gedaan bij een alfa-isotoop die in een aangeslagen toestand van een dochterkern vervalt.

Door tijd-amplitudeselectie toe te passen op de verkregen gegevens, waren we in staat om Po-215- en Rn-219-alfapieken van het totale spectrum te scheiden. Op deze manier vonden we asymmetrische alfapieken in $LaBr_3$:Ce en $LaBr_3$:Ce,Sr maar niet in $CeBr_3$. De oorzaak van dit fenomeen is niet bekend. Onze benadering om rekening te houden met nucleaire de-excitatieprocessen in simulaties te omvatten, is veelbelovend en biedt samen met experimentele gegevens over asymmetrische α-pieken een manier om een volledige en nauwkeurige simulatie van een scintillatierespons op een intrinsieke activiteit te construeren. We raden aan om de 215Po-alfapiek te gebruiken in toekomstige α/β-verhoudingsmetingen, omdat deze piek een gevolg is van zuiver alfa-verval naar een grondtoestand, en niet gevolgd wordt door een ander type van de-excitatie.

Hoofdstuk 4 breidt de digitale analysemethoden uit voor de studie van de pulsvorm van scintillatoren. Met deze methode hebben we een zwakke pulsvormafhankelijkheid gevonden als functie van de gamma-energie in het geval van CsI(Tl), alsmede verschillende scintillatie-vervaltijden voor excitatie door middel van gammastraling en gepulste röntgenstralen. De experimentele resultaten komen goed overeen met theoretische voorspellingen van Lu et al. [1], maar er zijn desalniettemin kleine verschillen die meer onderzoek vereisen.

In Hoofdstuk 5 hebben we een nieuwe aanpak voorgesteld voor het ontwikkelen van nieuwe nabij-infrarode scintillatoren. Door Sm^{2+} toe te voegen aan CsBa2I5:Eu2+, is energieoverdracht van Eu naar Sm mogelijk. Dit resulteert in een efficiënte nabij-infrarood stralende scintillator, emitterend op 755 nm. Het ^{137}Cs pulshoogtespectrum met een energie-resolutie van 3,2% bij 662 keV met APD-uitlezing kan worden beschouwd als het geboortebewijs van de eerste zwarte scintillator. Er zijn veel andere potentiële jodideverbindingen waar de nieuwe onderzoeksstrategie op kan worden toegepast. Een realistische evaluatie toont aan dat een resolutie van minder dan 2% goed haalbaar is. Tevens hebben we een resolutie van 5,4% aangetoond met een zeer goedkope Si-PM. Zo een detector kan bijvoorbeeld gemakkelijk worden opgenomen in kleine draagbare γ-spectrometers, zelfs in een smartphone-achtig apparaat, voor veiligheidstoepassingen.

In Hoofdstuk 6 onderzochten we de eis voor het verkrijgen van 5d-4f spin-toegestane emissie van samarium. We hebben ontdekt dat BaBrI een "grensgeval" is waarin Sm^{2+} zowel 5d-4f als 4f-4f-emissie vertoont. De lange vervaltijd van 4f-4f-emissie maakt een pulshoogtespectrummeting vrijwel onmogelijk. BaBrI:5%Eu,0,5%Sm kan dan ook niet worden gebruikt als een scintillator in γ-spectroscopie bij kamertemperatuur. Ook is de energieoverdracht in BaBrI: 5% Eu, 0,5% Sm niet volledig en voor het verkrijgen van hoge efficiëntie vereist dit optimalisatie van doteringsconcentraties. Deze verbinding vindt mogelijk geen toepassing in y-spectroscopie maar kan nog steeds worden gebruikt als bijvoorbeeld een rood-emitterend röntgenfosfor of in de luminescentiethermometrie [2, 3]. Als het 4f5d-niveau echter voldoende kan worden verlaagd om 4f-4f-emissie te voorkomen, eindigt de 5d-4f-emissie van Sm^{2+} in een van de zeven ^7F_J toestanden waarvan wordt verwacht dat deze de zelfabsorptie verlaagt in vergelijking met Eu^{2+}.

In Hoofdstuk 7 hebben we de mogelijke kandidaat-materialen voor efficiënte 5d-4f-emissie van samarium verder onderzocht. We hebben gevonden dat van de bestudeerde samenstellingen het $CsBa_2I_5$: 2% Eu^{2+}, 1% Sm^{2+} monster de beste scintillatieprestaties vertoont en een energie-resolutie van 3,2% bij 662 keV gamma-excitatie biedt. Het heeft een matige lichtopbrengst van 46.000 fotonen / MeV (@ 662 keV) en 2,1 μs scintillatievervaltijd. $CsBa_2I_5$ gedoteerd met alleen samarium vertoonde niet zulke goede scintillatieprestaties, wat de essentiële rol van europium in het elektron-gat invangingsproces van een ionisatiespoor aantoont.

REFERENCES

[1] X. Lu, S. Gridin, R. T. Williams, M. R. Mayhugh, A. Gektin, A. Syntfeld-Każuch, Ł. Świderski, and M. Moszyński, *Energy-Dependent Scintillation Pulse Shape and Proportionality of Decay Components for CsI:Tl: Modeling with Transport and Rate Equations,* Phys. Rev. Applied **7**, 014007 (2017).

[2] M. Dramicanin, *Luminescence Thermometry: Methods, Materials, and Applications* (Elsevier, 2018).

[3] C. D. S. Brites, S. Balabhadra, and L. D. Carlos, *Lanthanide-based thermometers: At the cutting-edge of luminescence thermometry,* Advanced Optical Materials **7**, 1801239 (2019), https://onlinelibrary.wiley.com/doi/pdf/10.1002/adom.201801239 .

ACKNOWLEDGEMENTS

My PhD project at TU Delft was enormously enriching experience. I learned a lot, not only about physics, but also doing science in general, people, different cultures, and also myself. I am deeply grateful for having this opportunity, and I cannot overestimate its importance.

This awesome endeavor would not be possible without Pieter Dorenbos choosing me for the project. I learned from Pieter lots of physics, but more importantly, I learned about doing science. A big thanks to the technicians: Johan, John, and Aday for keeping all the setups up and running. I would like to thank to Roy Awater for our discussions on the project. Our disagreements and different points of view always stimulated me to improve my reasoning and search for better explanations. I would like to thank Anna Dobrowolska for her introduction to life in Delft, at the University, and the group. Thanks to you I had very smooth introduction into Dutch culture :) I would like to thank Francesco Quarati for our discussions on internal contamination, and help with setting up low-background measurements. Thanks to Stefan Brunner for our discussions on scintillation mechanism, fast scintillators, Cherenkov radiation, and our search for ultra-fast intra-band luminescence ;) I also very appreciate your help with getting a test-board with a SiPM! I want to thank our industrial partners, Vladmir Ouspensky and John Frank from Saint-Gobain Crystals, for custom made samples and interesting discussions during our bi-annual meetings in Delft and Paris. I would like to thank to all people from Luminescence Research and Medical Imaging groups for our social activities and having fun together: Beien, Jarno, Tianshuai, Hongde, Minh, Pieter (Vesie), Giacomo, Maarten, Evert, Jumpei, and Erik. Special thanks to Evert for helping me with Dutch translation of Summary and Propositions!

Weronika Wolszczak
Delft, August 2019

CURRICULUM VITÆ

Weronika Wiktoria Wolszczak was born on 27th of December 1987 in Lipsko, Poland. She attended Jan Kochanowski 1th elementary and middle public school in Zwoleń, and Jan Kochanowski 6th Upper Secondary School in Radom. In September 2006, she started study at Inter-faculty Studies in Mathematics and Natural Sciences, University of Warsaw, with major in physics and minor in chemistry. In 2010 she joined Warsaw High Energy Physics group in Institute of Experimental Physics, Faculty of Physics, University of Warsaw. She was seconded for multiple research visits at CERN to perform work on muon trigger software development at the CMS experiment at LHC. In 2012 she defended Master of Science thesis in particle physics, *W boson mass measurement with the CMS experiment*. In 2012 she shifted her interest to Positron Emission Tomography imaging, and started collaboration with prof. dr. Marek Moszyński's research group at National Centre for Nuclear Research (Poland). The project was focused on developing a new depth-of-interaction encoding scheme using temperature dependent scintillation properties.

In March 2015, Weronika started her PhD research in the Luminescence Materials section lead by prof. dr. Pieter Dorenbos at Faculty of Applied Sciences, Delft Univeristy of Technology. The result of this research are presented in this thesis.

LIST OF PUBLICATIONS

1. **W. Wolszczak** and P. Dorenbos, "*Nonproportional Response of Scintillators to Alpha Particle Excitation*," in IEEE Transactions on Nuclear Science, vol. 64, no. 6, pp. 1580-1591, 2017, `https://doi.org/10.1109/TNS.2017.2699327`.
2. **W. Wolszczak** and P. Dorenbos, *Shape of intrinsic alpha pulse height spectra in lanthanide halide scintillators*, Nuclear Inst. and Methods in Physics Research, A, `http://dx.doi.org/10.1016/j.nima.2017.02.041`
3. **W. Wolszczak** and P. Dorenbos, *Time-resolved gamma spectroscopy of single events*, Nuclear Inst. and Methods in Physics Research, A, 886 (2018) 30–35 `https://doi.org/10.1016/j.nima.2017.12.080`
4. **W. Wolszczak**, K. W. Krämer, and P. Dorenbos, $CsBa_2I_5$*:*Eu^{2+}*,*Sm^{2+} *- The first high energy resolution black scintillator for* γ*-ray spectroscopy*, physica status solidi (RRL)–Rapid Research Letters, 2019, `https://doi.org/10.1002/pssr.201900158`.